Force-Controlled Robotic Micromanipulation for Mechanotransduction Studies of *Drosophila* Larvae

by

Weize Zhang

Department of Mechanical Engineering
McGill University

Montreal, Quebec, Canada

Febuary 2017

A thesis submitted to McGill University in partial fulfillment of the requirements for a doctoral degree

DEDICATION

To my parents who gave me life and all the support.

TABLE OF CONTENTS

LIST OF FIGURES

LIST OF TABLES

ABSTRACT

Robotic micromanipulation is a widely used experimental technique to physically interact with a microscale sample under a microscope, and has found important applications in cell microinjection, mechanical characterization of biomaterials, and assembly of micro-parts. Force sensing and control play important roles in robotic micromanipulation. For instance, monitoring the contact force in cell injection indicates the moment of cell membrane penetration, and controlling the grasping force of a microgripper allows accurate characterization of the mechanical properties of a material being manipulated. Recently, force-controlled robotic micromanipulation has found its new application in studying the neuron-level mechanobiology of Drosophila larvae. Specifically, the capability of accurately applying millinewton-level touch stimuli to a Drosophila larva and simultaneously observing resultant fluorescence signal transmissions in its mechanosensitive neurons will enable novel research on mechanisms of the animals mechanotransductive neural circuitries. The conventional method is to conduct the experiment manually, which is time consuming and requires extensive training for operators. A robotic micromanipulation system designed for this type of experiments could greatly facilitate the mechanobiology research on Drosophila with much higher accuracy, efficiency, and repeatability.

In this thesis, a force-controlled robotic micromanipulation system is developed for simultaneously applying accurate mechanical stimuli and quantifying fluorescence neuron transmission signals in Drosophila larvae. The system employs an elastomeric microdevice for immobilizing individual larvae on a substrate, and a microelectromechanical systems (MEMS) piezoresistive force sensor for applying a closed-loop controlled touch stimulus to a larva. A micromanipulator and a microscope XY stage are coordinately servoed using orchestrated position and force control laws for automatic operations. The system performs force-controlled larva touching and fluorescence imaging at a speed of four larvae per minute, with a success rate of 92.5%. A new force control

architecture, including a compensation-prediction scheme and a switched fuzzy to proportional-integral-derivative (fuzzy-PID) controller, is also proposed to effectively improve the dynamics of the force control system. The compensation-prediction scheme is employed to accommodate force measurement noise, system modelling errors, time delays and lack of position feedback from the micromanipulator. The switched fuzzy-PID controller is proposed to ensure the fast convergence and small steady-state oscillation of the system. Compared to conventional PID control scheme, the proposed architecture reduces the force overshoot to <5% and settling time to <0.2% s.

To verify the effectiveness of the developed system, it is used to apply mechanical stimuli to Drosophila larva with fluorescence-labelled class III ddaA neurons (which is known to be responsible to mechanical stimulation). Similar responses of the neural transmissions are acquired compared to those reported in the literature (obtained by manual operations), and significantly improved accuracy and efficiency are demonstrated. Leveraging the systems capability of accurately controlling the stimulation force, Mechanical stimuli were applied at different force levels (0.25-2 mN) to the larva samples, and experimentally determined, for the first time, the minimal force level to which the class III ddaA neurons of a Drosophila larva start to respond. This robotic system will greatly facilitate the dissection of mechanotransduction mechanisms of Drosophila larvae, and the proposed force control architecture could also be readily applied to other robotic micromanipulation systems to improve their dynamic performance.

RÉSUMÉ

Micromanipulation robotique est une technique d'interagir physiquement avec un échantillon sous un microscope, où un niveau de précision du mouvement est nécessaire qui ne peut être atteint par la main de l'homme sans aide. Cette technique est couramment utilisé dans l'injection de cellules, propriété mécanique caractérisation des matériaux et l'assemblage de pices sous micrométrique, etc.

Le sensoriel et le contrôle de la Force jouent des rôles importants dans la micromanipulation robotique. Par exemple, la surveillance de la force de contact à l'injection de cellules peut indiquer le moment de la pénétration de la membrane cellulaire, et à commander la force de préhension d'une micropince pourrait caractériser précisément les propriétés mécaniques d'un matériau.

Récemment, force contrôlée micromanipulation robotique a trouvé sa nouvelle application dans l'étude du comportement danger-fuite de *Drosophila* larves. La capacité d'appliquer avec précision stimuli niveau de millinewton tactiles à *Drosophila* larves et en observant simultanément leurs réponses de fluorescence résultantes dans la transmission des neurones mécanosensible permettra de nouvelles études de circuits mécanotransduction neuronal. Le procédé classique consiste à réaliser l'expérience manuellement, ce qui prend du temps et nécessite une formation complète pour les opérateurs. Un systme de micromanipulation robotique capable d'appliquer avec précision des stimuli mécaniques pourrait grandement faciliter la recherche de mécanobiologie sur *Drosophila*, et peut éventuellement mener à de nouvelles découvertes dans mécanotransduction des circuits de neurones.

Des efforts considérables ont été faits dans le domaine de la micromanipulation robotique force contrôlée. Cependant, les systèmes existants de micromanipulation forces contrôlées sont toujours sujettes au bruit de mesure, erreur de modélisation, la temporisation et la rétroaction insuffisante. Pas de solutions universelles à ces questions ont été proposées. Dans cette thèse, un régime

d'indemnisation-prédiction est proposée pour résoudre le bruit de mesure, erreur de modélisation, la temporisation et la rétroaction insuffisante tout à fait. Un contrôleur flou-PID commuté est proposé pour garantir la convergence rapide et petite oscillation d'état stable. L'idée de cette architecture de contrôle se résume comme suit: le inobservabilité causé par des retours insuffisants est résolu par une transformation mathématique des variables d'état de combiner deux termes inconnus dans un terme inconnu équivalent, puis une extension à gain élevé observateurs de bruit insensible (EHGO) estimations ce terme inconnu équivalent, ce qui rend le systme dépourvu de termes inconnus. Enfin, un prédicteur de Smith pour compenser le retard de temps. Le contrôleur flou converge la force de contact à la valeur objective à la vitesse maximale possible. Le système passe alors au contrôleur PID lorsqu'un seuil est atteint pour minimiser l'oscillation d'état stable. Les expériences montrent que cette architecture de commande réduit le temps de dépassement et de régler de manire significative, en dépit de la présence d'erreurs de modélisation, bruit de mesure, temps de retard, et la rétroaction insuffisante.

Le système utilise également une caméra de fluorescence qui pourrait observer les réponses de fluorescence dans la transmission des neurones mécanosensible de *Drosophila* larve. fonctionnalité de téléoperation supplémentaires, telles que manipulation via clavier, est également adopté pour faciliter davantage la procédure expérimentale. Les expériences biologiques montrent que la force de contact contrôlé avec précision pourrait stimuler les larves pour afficher le changement correspondant de l'intensité de fluorescence. Par rapport au fonctionnement manuel, ce systme améliore considérablement l'efficacité et réduit la formation requise pour les opérateurs.

ACKNOWLEDGEMENT

I would not be able to complete my thesis without the help from a group of people including Professors, staff, colleagues, friends and my family. First, I would like to thank my supervisor Professor Xinyu Liu who gave me the opportunity to pursue my doctoral degree at McGill University, guided me through the research explorations, and took care of my financial supports. His enthusiasm for research and high standard for research quality set the bar for me and will be my example in future.

I appreciate the financial supports from the Faculty of Engineering at McGill University.

I would like to express my great appreciation to my colleagues in Biomedical Microsystem Laboratory and other friends who are always ready to help: Longyan Chen, Xiao Li, Yu-Hsuan Wang, Pengfei Song, Xianke Dong, Chen Zhao, Juntian Qu, Qiyang Wu, Binbin Ying, Hao Fu, Philip Zwanenburg, Da-Eun Kim, Ayvi Islam, Alexandre Sobolevski, Anan Lu, Dylan Caverly, Guowei Zhong, Milda Sabiston, Zhuoran Wang, Bin Ouyang, and Elton Tan.

Last but not least, I owe the deepest thanks to my father Chaoying Zhang and my mother Haiyan Wei. They stand with me and support me through the difficult times.

CONTRIBUTION OF AUTHORS

This is a manuscript-based thesis consisting of five journal articles that have been published, submitted, or completed for submission. The titles of the articles, names of the authors, and their contributions are listed below.

- **Force-controlled Robotic Micromanipulation: A Review**

  Weize Zhang and Xinyu Liu

  Weize Zhang and Xinyu Liu are with the Department of Mechanical Engineering, McGill University, Montreal, Quebec H3A 0C3, Canada.

  To be submitted.

  Author contributions:

  Weize Zhang organized the literature information, collected the presentation items, and wrote the manuscript.

  Xinyu Liu wrote the manuscript.

- **An Automated Force-Controlled Robotic Micromanipulation System for Mechanotransduction Studies of *Drosophila* Larvae**

  Weize Zhang, Alexandre Sobolevski, Bing Li, Yong Rao, and Xinyu Liu

  Weize Zhang, Alexandre Sobolevski, Bing Li, and Xinyu Liu are with the Department of Mechanical Engineering, McGill University, Montreal, Quebec H3A 0C3, Canada. Bing Li is also with the School of Information and Engineering, Huzhou Teachers College, China. Yong Rao is with the Department of Neurology and Neurosurgery, McGill University.

  IEEE Transactions on Automation Science and Engineering, vol. 13, no. 2, pp. 789–797, 2016. DOI 10.1109/TASE.2015.2403393.

  Author contributions:

Weize Zhang designed and conducted the experiments, collected and analyzed the data, and wrote the manuscript.

Alexandre Sobolevski provided the image processing algorithm.

Bing Li analyzed the data.

Yong Rao prepared larva samples.

Xinyu Liu supervised the project, co-designed the experiments, and wrote the manuscript.

- **Switched Fuzzy-PD Control of Contact Forces in Robotic Micro-Biomanipulation**

  Weize Zhang, Xianke Dong, and Xinyu Liu

  The authors are with the Department of Mechanical Engineering, McGill University, 817 Sherbrooke Street West, Montreal, QC, Canada, H3A 0C3.

  IEEE Transactions on Biomedical Engineering, accepted.

  Author contributions:

  Weize Zhang designed and conducted the experiments, collected and analyzed the data, and wrote the manuscript.

  Xianke Dong conducted the experiments and wrote the manuscript.

  Xinyu Liu supervised the project, co-designed the experiments, and wrote the manuscript.

- **A Model Compensation-Prediction Scheme for Control of Micromanipulation Systems with a Single Feedback Loop**

  Weize Zhang, Juntian Qu, Xuping Zhang, and Xinyu Liu

  The authors are with the Department of Mechanical Engineering, McGill University, 817 Sherbrooke Street West, Montreal, QC, Canada, H3A 0C3.

  Submitted.

  Author contributions:

  Weize Zhang designed and conducted the experiments, collected and analyzed the data, and wrote the manuscript.

  Juntian Qu conducted the experiments.

  Xinyu Liu supervised the project, co-designed the experiments, and wrote the manuscript.

- **Quantifying the Relationship between Touch Force and Signal Transmission of Class III ddaA Neurons in *Drosophila* Larvae**

  Weize Zhang, Yixu Chen, Yong Rao, and Xinyu Liu

  Weize Zhang and Xinyu Liu are with the Department of Mechanical Engineering, McGill University, 817 Sherbrooke Street West, Montreal, QC, Canada, H3A 0C3. Yixu Chen and Yong Rao is with the Department of Neurology and Neurosurgery, McGill University.

  To be Submitted.

  Author contributions:

  Weize Zhang designed and conducted the experiments, collected and analyzed the data, and wrote the manuscript.

  Yixu Chen and Yong Rao prepared the larva samples.

  Xinyu Liu supervised the project, co-designed the experiments, and wrote the manuscript.

CHAPTER 1
Introduction

1.1 Robotic Micromanipulation Systems for Biomedical Research

Robotic micromanipulation refers to the robotic science and technology for physically interacting with microscale objects, which is typically performed under a microscope. Examples of micromanipulation tasks for which robotic technologies can be used include micro-assembly of microelectrochemical systems (MEMS) parts, orientation, transfer, and microinjection of biological cells, mechanical stimulation of small organisms, just to name a few. Robotic micromanipulation systems are systems that benefit from technologies in a variety of fields such as automation, optics, computer vision, and sensory to facilitate micromanipulation tasks, which would be less effective or less accurate if done manually. Robotic micromanipulation systems of bio-samples and soft materials (e.g. cells, tissues, small organisms, PDMS (Polydimethylsiloxane) and hydrogel, etc.) are crucial in biological, material and medical research. In the past two decades, numerous robotic systems capable of specific micromanipulation tasks such as single-cell transportation [1, 2, 3], high-throughput cell injection [4, 5, 6, 7, 8, 9, 10], cutting [11], grasping [12, 13, 14, 15], deposition [16, 17], and orientation [18, 19, 20], cell/tissue mechanical characterization [21, 22, 23], and whole organism injection [24], to name a few. These robotic systems operate efficiently and consistently, and thus could significantly improve the reproducibility and throughput of the biomanipulation procedures and even enable new types of studies that cannot be fulfilled by conventional techniques.

Contact force is involved in a wide range of micomanipulating interactions (i.e. microgripper and test subject, glass pipette and cell membrane, etc.). Force sensing and control are essential technologies in robotic micromanipulation [25, 26]. Measurement of interaction forces in a real-time manner between a biological sample and an end-effector serves as an additional feedback to the manipulation procedure, and could improve the robustness and the dexterity of robotic micromanipulation systems. For instance, the measurement of indentation forces during cell injection could precisely predict the moment of penetration of cell membrane and thus initialize injecting the material [27, 28, 6]. Closed-loop control of grasping force levels during robotic cell pick-place using a microelectromechanical systems (MEMS) microgripper guarantees secured grasping while avoiding cell damage by overlarge forces [12].

Accurate contact force regulating has been proven useful for applying mechanical stimuli to in-*vivo* bio-samples and studying their mechanotransduction responses [29, 30, 31, 32]. Given that most biomanipulation tasks require optical microscopes, advanced optical imaging techniques could be conveniently implemented on a robotic micromanipulation system to visualize real-time mechanotransduction responses of bio-samples.

Drosophila is one of the most popular model organisms for studying sensory mechanotransduction and the related molecular and cellular mechanisms [33]. Its behavior at presence of mechanical stimuli has been thoroughly studied [34, 35, 36]. A recent research proved that under millinewton-level touches at anterior segments of body, *Drosophila* larvae tend to reorient and select a new path for further movement [34]. Follow-up genetic and neural experiments showed that a set of $\sim$50 interconnected neurons expressing the cell-surface protein Turtle (Tutl) are responsible for the reorientation. These interesting discoveries partially unveiled the unknown underlying mechanisms governing navigation patterns in response to mechanical stimuli, and further more, the biological explanation of larvae's survival instinct at the presence of environmental danger. However, despite these merits, all current study applied forces to the *Drosophila* larvae manually, resulting in errors due to human involvement: In manual operations, the touch force is measured through visual estimation under an optical microscope [34]. The stiffness of a hair is first calibrated with a weighing scale, and the deformation of the hair under the desired amount of force is recorded. When the biological experiment is conducted, the operator visualizes the deformation of the hair under the microscope, and manually controls the touch force to reach the desired level through human-eye visualization of the hair deformation [34]. This technique is inaccurate, and may cause significant variations in the biological results. An automated system capable of regulating touching force is highly desired.

Paralleling mechanical stimuli upon *Drosophila* larvae and fluorescent calcium imaging of specific neural networks (i.e. class III dda A, *tutl*, etc.) will enable the investigation of roles of neurons in governing the touch-induced reactions. However, at current level of study, experimental setups

previously employed [34, 35, 36] lack in-*vivo* immobilizing *Drosophila* larvae for fluorescent imaging. In addition, the gentle touch was applied manually using a fine hair [34] or an eye lash [35], resulting in inaccurate open-loop force. Single level touch force was applied, so the relationship between touch force and fluorescence intensity could not be obtained. A robotic micromanipulation system capable of high-resolution touch force control and quantitative fluorescent imaging is highly desired. Biological experiments may require large quantities of samples to be tested, which may lead to a heavy workload for a human operator and possible cause large variations in experimental results due to human fatigue and inconsistency. Therefore, high throughput is a desirable characteristic of the micromanipulation system to be developed.

1.2 Thesis Objective

The overall objective of my Ph.D. research is to develop an automated robotic micromanipulation system with advanced touch force controller for studying the touch-related neural circuits in *Drosophila* larvae. The detailed objectives are listed as follows:

1. To design the architecture and integrate the hardware of a robotic micromanipulation system, including two micromanipulators (microrobots), a fluorescent microscope, and a digital camera.
2. To develop the system control interface using Visual C++, which can display the camera video in real time ($\geq$ 30 Hz) and control the motions of the two microrobots via GUI buttons.
3. To develop a polymer-based microdevice for immobilizing *Drosophila* larva in an array to facilitate the robotic micromanipulation.
4. To design and implement an advanced force control law that includes a switched fuzzy-PID controller and a noise-insensitive EHGO (extended high gain observer), which overcomes the inherent control challenges of the system such as nonlinearity, unknown modeling terms, and measurement noise.
5. To perform biological experiments using the robotic system and study the signal transduction of the Tutl-positive neural circuits in response to force-regulated touches.

1.3 Thesis Organization

This thesis is organized as follow:

Chapter 1 describes the objective of this research; Chapter 2 gives a brief introduction to the current research and common issues of force controlled robotic micromanipulation; Chapter 3 describes the general layout and setup of a robotic micromanipulation platform, with a simple PID controller integrated into the system; Chapter 4 gives a new switched fuzzy-PD controller that significantly improves system performance; Chapter 5 give a compensation-prediction scheme as a solution to the common issues (time delay, measurement noise, modeling error and insufficient feedback) with the micromanipulation systems; and Chapter 6 demonstrates the biological results on *Drosophila* larvae samples.

References

[1] S. Hu and D. Sun, "Automatic transportation of biological cells with a robot-tweezer manipulation system," *Int. J. Robot. Res.*, vol. 30, no. 14, pp. 1681–1694, 2011.

[2] C. C. Cheah, X. Li, X. Yan, and D. Sun, "Observer-based optical manipulation of biological cells with robotic tweezers," *IEEE Trans. Robot.*, vol. 30, no. 1, pp. 68–80, 2013.

[3] A. Thakur, S. Chowdhury, P. Švec, C. Wang, W. Losert, and S. K. Gupta, "Indirect pushing based automated micromanipulation of biological cells using optical tweezers," *Int. J. Robot. Res.*, vol. 33, pp. 1098–1111, 2014.

[4] W. Wang, X. Y. Liu, D. Gelinas, B. Ciruna, and Y. Sun, "A fully automated robotic system for microinjection of zebrafish embryos," *PLoS ONE*, vol. 2, no. 9, e862, 2007.

[5] W. H. Wang, X. Y. Liu, and Y. Sun, "High-throughput automated injection of individual biological cells," *IEEE Trans. Autom. Sci. Eng.*, vol. 6, no. 2, pp. 209–219, 2009.

[6] H. B. Huang, D. Sun, J. K. Mills, and S. H. Cheng, "Robotic cell injection system with position and force control: toward automatic batch biomanipulation," *IEEE Trans. Robot.*, vol. 25, no. 3, pp. 727–737, 2009.

[7] Y. Xie, D. Sun, C. Liu, H. Tse, and S. Cheng, "A force control approach to a robot-assisted cell microinjection system," *Int. J. Robot. Res.*, vol. 29, no. 9, pp. 1222–1232, 2010.

[8] X. Liu, R. Fernandes, M. Gertsenstein, A. Perumalsamy, I. Lai, M. Chi, K. H. Moley, E. Greenblatt, I. Jurisica, R. F. Casper, et al., "Automated microinjection of recombinant bcl-x into mouse zygotes enhances embryo development," *PLoS ONE*, vol. 6, no. 7, e21687, 2011.

[9] H. P. Spaink, C. Cui, M. I. Wiweger, H. J. Jansen, W. J. Veneman, R. Marín-Juez, J. de Sonneville, A. Ordas, V. Torraca, W. van der Ent, et al., "Robotic injection of zebrafish embryos for high-throughput screening in disease models," *Methods*, vol. 62, no. 3, pp. 246–254, 2013.

[10] J. Liu, V. Siragam, Z. Gong, J. Chen, M Fridman, C. Leung, Z. Lu, C. Ru, S. Xie, J. Luo, et al., "Robotic adherent cell injection (raci) for characterizing cell-cell communication," *IEEE Trans. Biomed. Eng.*, vol. PP, no. 99, pp. 1–1, 2014.

[11] N. Inomata, T. Mizunuma, Y. Yamanishi, and F. Arai, "Omnidirectional actuation of magnetically driven microtool for cutting of oocyte in a chip," *J. Microelectromech. Syst.*, vol. 20, no. 2, pp. 383–388, 2011.

[12] K. Kim, X. Liu, Y. Zhang, and Y. Sun, "Nanonewton force-controlled manipulation of biological cells using a monolithic mems microgripper with two-axis force feedback," *J. Micromech. Microeng.*, vol. 18, no. 5, p. 055 013, 2008.

[13] T. Tanikawa and T. Arai, "Development of a micro-manipulation system having a two-fingered micro-hand," *IEEE Trans. Robot. Autom.*, vol. 15, no. 1, pp. 152–162, 1999.

[14] M. Jeannerod, M. A. Arbib, G. Rizzolatti, and H Sakata, "Grasping objects: the cortical mechanisms of visuomotor transformation," *Trends Neurosci.*, vol. 18, no. 7, pp. 314–320, 1995.

[15] S. Chowdhury, A. Thakur, C. Wang, P. Svec, W. Losert, and S. K. Gupta, "Automated indirect transport of biological cells with optical tweezers using planar gripper formations," in *2012 IEEE International Conference on Automation Science and Engineering (CASE)*, IEEE, 2012, pp. 267–272.

[16] Z. Lu, C. Moraes, G. Ye, C. A. Simmons, and Y. Sun, "Single cell deposition and patterning with a robotic system," *PLoS ONE*, vol. 5, no. 10, e13542, 2010.

[17] Y. H. Anis, M. R. Holl, and D. R. Meldrum, "Automated selection and placement of single cells using vision-based feedback control," *IEEE Trans. Autom. Sci. Eng.*, vol. 7, no. 3, pp. 598–606, 2010.

[18] X. Liu, Z. Lu, and Y. Sun, "Orientation control of biological cells under inverted microscopy," *IEEE/ASME Tran. Mechatron.*, vol. 16, no. 5, pp. 918–924, 2011.

[19] C. Leung, Z. Lu, X. P. Zhang, and Y. Sun, "Three-dimensional rotation of mouse embryos," *IEEE Trans. Biomed. Eng.*, vol. 59, no. 4, pp. 1049–1056, 2012.

[20] Q. Zhao, M. Sun, M. Cui, J. Yu, Y. Qin, and X. Zhao, "Robotic cell rotation based on the minimum rotation force," *IEEE Trans. Autom. Sci. Eng.*, vol. PP, no. 99, pp. 1–12, 2014, ISSN: 1545-5955. DOI: 10.1109/TASE.2014.2360220.

[21] P Jordan, S Socrate, T. Zickler, and R. Howe, "Constitutive modeling of porcine liver in indentation using 3d ultrasound imaging," *J. Mech. Behav. Biomed.*, vol. 2, no. 2, pp. 192–201, 2009.

[22] X. Liu, J. Shi, Z. Zong, K.-T. Wan, and Y. Sun, "Elastic and viscoelastic characterization of mouse oocytes using micropipette indentation," *Ann. Biomed. Eng.*, vol. 40, no. 10, pp. 2122–2130, 2012.

[23] H. Xie, M. Yin, W. Rong, and L. Sun, "In situ quantification of living cell adhesion forces: single cell force spectroscopy with a nanotweezer," *Langmuir*, vol. 30, no. 10, pp. 2952–2959, 2014.

[24] M. Nakajima, T. Hirano, M. Kojima, N. Hisamoto, N. Nakanishi, H. Tajima, M. Homma, and T. Fukuda, "Local nano-injection of fluorescent nano-beads inside c. elegans based on nanomanipulation," in *2012 IEEE/RSJ International Conference on Intelligent Robots and Systems (IROS)*, IEEE, 2012, pp. 3241–3246.

[25] Z. Lu, P. C. Chen, and W. Lin, "Force sensing and control in micromanipulation," *IEEE Trans. Syst., Man, Cybern. C, Appl. Rev.*, vol. 36, no. 6, pp. 713–724, 2006.

[26] X. Y. Liu, K. Kim, Y. Zhang, and Y. Sun, "Nanonewton force sensing and control in microrobotic cell manipulation," *Int. J. Robot. Res.*, vol. 28, no. 8, pp. 1065–1076, 2009.

[27] Z. Lu, P. C. Y. Chen, J. Nam, R. Ge, and W. Lin, "A micromanipulation system with dynamic force-feedback for automatic batch microinjection," *J. Micromech. Microeng.*, vol. 17, no. 2, pp. 314–321, 2007.

[28] X. Liu, Y. Sun, W. Wang, and B. M. Lansdorp, "Vision-based cellular force measurement using an elastic microfabricated device," *J. Micromech. Microeng.*, vol. 17, no. 7, p. 1281, 2007.

[29] M. Girot, M. Boukallel, and S. Régnier, "A microforce and nanoforce biomicroscope device for in vitro mechanotransduction investigation," *IEEE Trans. Instrum. Meas.*, vol. 57, no. 11, p. 2532, 2008.

[30] J. H. Nam, P. C. Y. Chen, Z. Lu, H. Luo, R. Ge, and W. Lin, "Force control for mechanoinduction of impedance variation in cellular organisms," *J. Micromech. Microeng.*, vol. 20, no. 2, p. 025 003, 2010.

[31] M. L. Han, Y. L. Zhang, M. Y. Yu, C. Y. Shee, and W. T. Ang, "Non-contact force sensing for real-time stressing of biological cells," *Micro Nano Lett.*, vol. 6, no. 5, pp. 306–310, 2011.

[32] H. Ladjal, J.-L. Hanus, A. Pillarisetti, C. Keefer, A. Ferreira, and J. P. Desai, "Reality-based real-time cell indentation simulator," *IEEE/ASME Trans. Mechatron.*, vol. 17, no. 2, pp. 239–259, 2012. DOI: 10.1109/TMECH.2010.2091010.

[33] G. G. Ernstrom and M. Chalfie, "Genetics of sensory mechanotransduction," *Annu. Rev. Genet.*, vol. 36, no. 1, pp. 411–453, 2002.

[34] Y. Zhou, S. Cameron, W.-T. Chang, Y. Rao, et al., "Control of directional change after mechanical stimulation in drosophila," *Mol. Brain*, vol. 5, no. 1, pp. 39–51, 2012.

[35] R. Y. Hwang, L. Zhong, Y. Xu, T. Johnson, F. Zhang, K. Deisseroth, and W. D. Tracey, "Nociceptive neurons protect drosophila larvae from parasitoid wasps," *Curr. Biol.*, vol. 17, no. 24, pp. 2105–2116, 2007.

[36] A. Tsubouchi, J. C. Caldwell, and W. D. Tracey, "Dendritic filopodia, ripped pocket, nompc, and nmdars contribute to the sense of touch in drosophila larvae," *Curr. Biol.*, vol. 22, no. 22, pp. 2124–2134, 2012.

CHAPTER 2
Force-controlled Robotic Micromanipulation: A Review

Force-controlled Robotic Micromanipulation: A Review

Weize Zhang and Xinyu Liu*

Department of Mechanical Engineering, McGill University, 817 Sherbrooke Street West,

Montreal, Quebec H3A 0C3, Canada

*Corresponding author: xinyu.liu@mcgill.ca.

To be submitted.

Robotic systems improve the efficiency and accuracy of micromanipulation tasks over conventional manual operations. Force control has been widely involved in robotic micromanipulation systems to provide better performance. However, the characteristics that differ interaction forces at microscale from that at macroscale make closed-loop force control in robotic micromanipulation a challenging task. In this paper, we review the state of the art of force-controlled robotic micromanipulation techniques. We first present typical robotic micromanipulation tasks for biological samples. Commonly used force sensing and actuation tools for robotic micromanipulation are then discussed, and their advantages and disadvantages are pointed out. Force control design techniques and applications in various types of robotic micromanipulation tasks are presented. The influence of major difficulties in force controller design, including modeling error, time delay, measurement noise, insufficient feedback, and nonlinearity are outlined. Current control architectures and their limitations are summarized finally.

Index Terms-Robotic micromanipulation, force control, microscale, biological samples, *Drosophila* larva, control architecture

2.1 Introduction

Robotic micromanipulation is an important experimental approach for physical interactions with biological cells and small organisms. It has resulted in novel capabilities for biological and biomedical research, and found important applications in numerous domains such as genetics, development, pathology, and pharmaceutics, to name a few. Combining techniques in robotics, automation, and micro-electro-mechanical systems (MEMS), robotic micromanipulation systems is becoming increasingly accurate, intelligent, and efficient; and are able to manipulate a wide range of biological samples, from small organisms, to single cells, and to subcellular organelles. Since late 1990s, a variety of effective robotic micromanipulation systems have been developed to tackle various problems, aiming to automate the micromanipulation processes and provide much improved manipulation precision, efficiency, and consistency.

When performing micromanipulation tasks, the operator always needs to position and physically interact (with force) with small objects. Mature techniques already exit to solve the positioning problem. Successful microscale positioning is demonstrated in various robot-assisted operations [1, 2, 3, 4]. However, only positioning capability under microscope is not adequate for more sophisticated micromanipulation tasks, such as operations that require high degree of dexterity, because microscale objects are usually fragile and easy to damage. Thus, position-only strategies may not ensure sample integrity and thus cause the manipulation task to eventually fail. This is the reason why force control is critical in many robotic micromanipulation tasks. In addition, obtaining the interaction force information is also one of the major objectives for certain applications such as mechanical property characterisation of bio-samples. However, the material's properties at the microscale set obstacles for designing a satisfactory force controller. For instance, the adhesion force between a sample and an end effector becomes dominant at the microscale, which adds additional uncertainties to the system model; the interaction force is also at the micronewton to nanonewton range, making the force feedback signal noisy. These factors and make it particularly challenging to perform the force control in robotic micromanipulation.

In this review, typical robotic micromanipulation tasks for bio-samples are presented. Commonly used force sensing and actuation tools for robotic micromanipulation are discussed. Force control design techniques and applications are reviewed. Major difficulties in force controller design are analysed. Current control architectures and their limitations are reviewed in detail.

2.2 Robotic Micromanipulation of biological Samples

2.2.1 Robotic Micromanipulation for Cell Injection

Cell injection is a method to deliver foreign material into target single cells with a glass pipette. Among various experimental methods that could introduce foreign materials into single cells, including virus vectors [5, 6], lipofection [7], electroporation [8, 9, 10], and microinjection [11], microinjection is advantageous for the following reasons. Virus vectors and lipofection rely heavily on engineered molecules to introduce foreign molecules into cells. Electroporation and microinjection both belong to the same category of physical methods, which use electrical and mechanical forces respectively to make the foreign material cross over the cell membrane [8]. Cell injection punctures directly the cell membrane with a glass pipette and introduce the material by applying a well controlled pressure pulse. Fig. 2–1 shows a photograph of injecting a mouse embryo. Electroporation may cause less damage to cell compared to microinjection. However, microinjection has an edge that the quantity of the material delivered can be controlled by regulating the duration and amplitude of the pressure pulse applied. In addition, microinjection could target specific intracellular locations (e.g., nucleus and cytoplasm) to deposit the material. Compared with other experimental methods, microinjection is applicable to many types of cells and materials, which makes it a universal solution.

Cell immobilization is a method to immobilize target cells which could significantly simplify cell search/positioning tasks. Four cell immobilization methods have been reported. The first method immobilizes a cell with a holding pipette [12]. The second method immobilizes multiple cells in a pattern via vacuum suction [13, 14, 15]. The third method utilizes half circular grooves with cavities to immobilize cells [16]. The last method attaches a single cell on a substrate by gluing [17, 18, 19]. Note that all these methods require certain amount of manual operations.

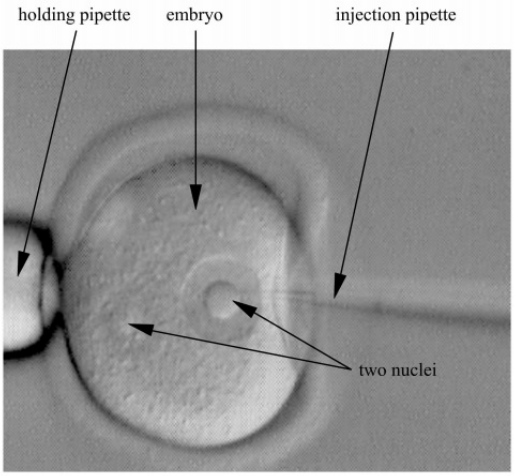

Figure 2–1: Cell injection of a mouse embryo, adapted from [12].

2.2.2 Robotic Transfer of Biological Samples

Another important application of robotic micromanipulation is bio-sample transfer. By transferring bio-samples from one place to another, several tasks, such as cell sorting and isolation [20], cell-cell communication [21] and cell fusion [22], could be conducted. Specific tools have been developed to fulfill different tasks, including mechanical microgrippers, transfer pipettes, laser traps, and untethered microrobots.

Microgrippers are end effectors that utilize two or more arms to conduct manipulation tasks such as grasping, releasing, transferring, and even surgery [23, 24, 25, 26, 27]. Transfer pipettes employ a pressure unit connected to a glass micropipette to aspirate and push cells [28, 29, 30]. Laser trapping is a technique based on the property that when a cell is illuminated by a focus low-power laser on one side, the cell will overcome the viscosity force and move to the centre of the laser beam [31]. Magnetically actuated microrobots are made from ferromagnetic materials with the surrounding magnetic field regulated by currents in coils of external circuitry to act as micromanipulators [32, 33].

2.2.3 Robotic Micromanipulation of *Drosophila Larvae*

Drosophila larva, as shown in Fig. 2–2, is a popular model organism for studying animal behaviors, sensory mechanotransduction, and their underlying molecular and cellular mechanisms

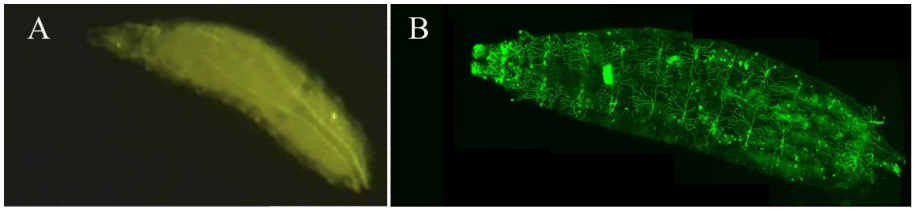

Figure 2–2: (A) Photograph of *Drosophila* larva in bright field, adapted from [37]. (B) Photograph of *Drosophila* larva in fluorescence, adapted from [39]

[34, 35]. Increasing interests arise upon the fact that a *Drosophila* larva tends to turn/roll at the presence of touch [36, 37, 38], which is the basis of their danger-escaping behaviors and is critical for this creature to survive.

Numerous neuron types have been investigated to determine the relationship between the mechanical touch stimuli and the neuronal responses. Even though most of the neuron types found in the *Drosophila* larval body wall remain unexplored [38], it has been demonstrated that Class I to IV neurons are nociceptive and related to larval locomotion, among which the Class III md neurons contribute to the larval response to gentle touch, and can be activated by force stimuli [38]. Therefore, Class III neurons have drawn increasing attentions in biological study [38, 39, 37], and will be thoroughly investigated by our robotic micromanipulation system.

One method to investigate Class III neurons is to visualize their calcium signal transmission through fluorescence imaging when mechanical stimuli are applied. In [38, 39, 37], eye lashes were attached to a micromanipulator to control the depth of touch. In [36], human hairs were used instead of eye lashes to perform the same type of experiments. The time-lapse history of consecutive images of fluorescence intensity is given in [38]. Even though these experiments are performed with open-loop controlled forces, biological advances have been made. The neuron that shows significant change in fluorescence intensity has been identified to be Class III ddaA [38].

2.3 Force Sensing and Actuating Tools

2.3.1 Force Sensors

Force sensing at the microscale becomes different from that at the macroscale [40, 41]. Two types of force sensors are commonly used force measurement at the microscale level, including piezoelectric and piezoresistive sensors.

2.3.1.1 Piezoelectric Sensor

Piezoelectric force sensors are known for its versatility in various applications. It is a mature measurement technique with outstanding inherent reliability. Its basic mechanism is related to the electric dipole moments inside a piezoelectric material, and the polarization changes at the presence of mechanical stress. The reversible and linear piezoelectric effect manifests as the production of a charge (voltage) upon application of stress (direct effect) and/or as the production of strain (stress) upon application of an electric field [42]. Fig. 2–3 shows a piezoelectric sensor containing multiple layers. Piezoelectric materials have good electromechanical properties for fabricating micromachined sensors [43]: the piezoelectric phenomenon does not exhibit failure mode associated with charge storage; it is reversible and typically linear [44]. Numerous studies have been conducted on piezoelectric sensors. Piezoelectric microbalances have been developed as sensitive biological and chemical sensors [45]. Piezoelectric effect is also proved to be useful in fabricating strain gauges [46]. Piezoelectric transducers are used as muscle movement detectors for medical purpose [47]. Ultrasonic piezoelectric sensors are used in acoustic emission detection [48].

2.3.1.2 Piezoresistive Sensor

Piezoresistive sensors are among the earliest MEMS devices [50]. They are easy to fabricate and provide relatively high accuracy of measurement (some are at nanonewton level) and the readout circuit is simple (usually a Wheatstone Bridge), which facilitates its use in robotic micromanipulation systems. The piezoresistive effect describes the change in the electrical resistivity of a material (usually a semiconductor or a metal) at presence of mechanical strain. Unlike the piezoelectric effect, the piezoresistive effect only causes electrical resistance to change. The change in resistance is mainly due to two factors: the change in geometry and the change in resistivity.

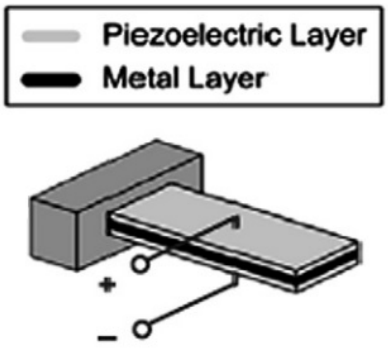

Figure 2–3: Schematic drawing of a piezoelectric sensor containing multiple layers, adapted from [49].

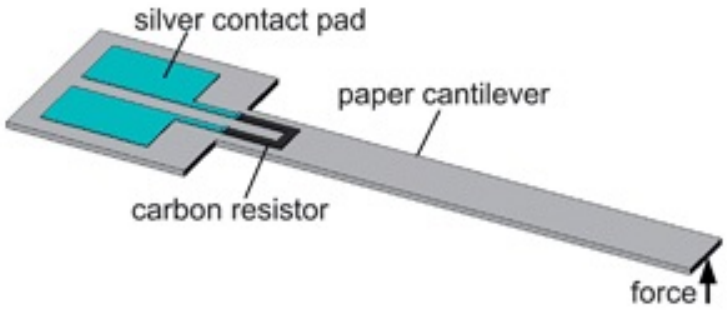

Figure 2–4: Schematic drawing of a paper based piezoresistive force sensor, adapted from [53].

For metal, the change in geometry has a much higher influence than the change in resistivity. But for semiconductor, it is the latter that contributes to the change in resistance (50-100 times more than the geometry part) [50]. Fig. 2–4 shows the schematic of a paper based piezoresistive force sensor. This fact manifests as the principle of piezoresistive force sensors with a very high coefficient of sensitivity, making it a better choice for MEMS than metallic material [51, 52]. Silicon is a common material for piezoresistive sensing.

Silicon piezoresistors have been widely used for various sensors including pressure sensors, accelerometers, cantilever force sensors, inertial sensors, and strain gauges, among which cantilever force sensors and strain gauges are extensively used in microrobotics [50]. Cantilever beams are simple in structure and inexpensive to build [54]. They form a variety of practical applications of piezoresistive sensors, commonly used for force, displacement and mass sensing [50]. Several

schemas have been proposed [55, 56, 57, 58, 59]. Besides these applications, cantilever beam sensors are also widely used in environmental [60], chemical [61] and biological sensing [62, 63, 64]. Strain measurement is another important application in microrobotics. Interests in semiconductor strain sensing was generated since the discovery of the piezoresistive effect in silicon and germanium in [65]. An increasing number of recent studies focus on integrating rosette patterns into silicon die for integrated circuit packaging stresses measurement [66]. 3D sensing capability is also demonstrated when implemented with planar arrangements of pseudo-hall effect [67]. In a word, piezoresistive sensing provides sensitive, accurate and easy-to-use measurement, as well as low cost. These key characteristics make piezoresistive sensing an effective and reliable choice for force sensing in robotic micromanipulation.

2.3.1.3 Force Sensor Based on Hall Effect

The Hall effect allows the detection of changes in magnetic field, which has been fully exploited in fabrication of force sensors, angular velocity sensors and displacement sensors, and so on. Force sensors based on Hall effect provides high sensitivity and repeatability, small footprint, low power consumption, and high corrosion resistance [68, 69, 70]. Hall-effect force sensors also have certain limitations. For instance, the Hall-effect sensing components are more susceptible to temperature change, and have relatively low linearity. Single-chip Acorn RISC Machine (ARM) based temperature compensation methods have been investigated in [71].

2.3.2 Actuators

2.3.2.1 Micromanipulator with Step or DC Motor

In conventional optics domain, motorized micromanipulators integrated into translational or rotational stages are classic motion control tools. These devices usually employ a stepper or DC (direct current) motor, and an anti-backlash screw-and-nut mechanism to translate linearly the rotation of motor into the movement of stage. DC motors generate smooth and continuous motion, while stepper motors rotate in discrete steps at response to electrical pulses [72].

Micromanipulators with stepper motors work by the principle of magnetic attraction. By alternately injecting current into the individual windings in the motor stator, a turning and a

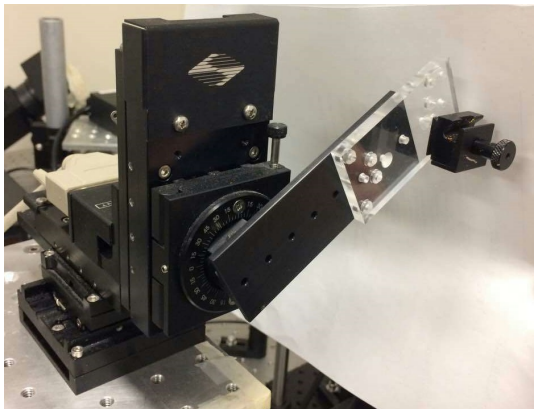

Figure 2–5: A photograph of MP-285 stepper motor based micromanipulator.

holding torque are created which turns and stops a permanent magnet and/or an iron rotor, respectively. Unlike DC motors, a stepper motor has an inherent holding torque that maintain the position of the device during the power-off state for a short period of time. The discrete characteristic of this device enables it intrinsic position feedback by simply counting the number of pulses it receives. Advanced commercial systems, such as MP-285 (Sutter Instrument, Fig. 2–5), could achieve over 20 mm range while maintaining a resolution better than 1 μm. However, stepper motors have the risk of losing steps, which requires careful operation and maintenance.

Micromanipulators with DC motors are characterized by smooth and continuous motions and wide speed ranges. They do not have build-in position feedback; however, if used with an encoder, these devices could provide sub-micrometer accuracy. When an electric current is applied into the coil of wire inside a permanent magnetic field, the coil interacts with the magnetic field and starts to turn. The property of DC motor does not allow it maintain position without electric power or external break, so it does not posses the "set and hold" function as a step motor. It consumes energy when holding a position and generates heat. On top of that, even with an incorporated encoder that provides position feedback, it may suffer from additional oscillation due to the hysteresis effect.

2.3.2.2 Micromanipulator using Magnetic Levitation

Micromanipulators based magnetic levitation technology have been investigated in the last decade [73, 74, 75, 76]. These devices do not require tethering structures, which allow them to be implemented and operated under environments which could not be accessed by other methods, such as blood vessels and hazardous environments [74]. This characteristic also eliminates vibrations of the micromanipulation systems, which are usually caused by structural compliance [74].

However, magnetic-levitation-based (MagLev) micromanipulators have relatively poor positioning resolution compared to mechanical micromanipulators, such as motor-driven micromanipulators. The positioning resolution of the MagLev micromanipulators is on the order of magnitude of 0.1 mm [74, 75], while conventional mechanical micromanipulators could achieve sub-micrometer resolution. Moreover, the performance of MagLev micromanipulators is sensitive to its payload. Different levels of payload result in different positioning resolution values [74].

2.3.2.3 Micropositioner

A micropositioner is a device that controls the position and the movement of an object at the precision of micron level, with a certain amount of degrees of freedom (DOF) [77]. This is extremely practical when position and attitude control under disturbance are required. Originally patented in 1980s, micropositioners have gone through rapid development and have held substantial importance in robotic micromanipulation, with ever improving performance, including speed, precision, stability, DOF and minimization. Many practical designs have been proposed in recent studies, with different design objectives. Some designs aim to extend the DOF, which allows for full 6-DOF (3 translational and 3 rotational) manipulation [78, 79]. Extended travel range, ground plate-free structure and immunity from levitation are analyzed in [80]. Mass balancing concept is adopted for vibration rejection [81]. Simple planar structure with low electricity consumption is tested in [82].

Despite these differences, current designs share the following characteristics. Their mechanisms are mostly rotory/joint parallel kinetic mechanism (PKM) because PKM facilitates design and fabrication. Most designs are actuated by comb drive since comb drive actuation theories are

mature and easy to realize. Most of them are fabricated from silicon on insulator (SOI), silicon bulk or poly silicon because these operations could be done through traditional microfabrication processes.

Some disadvantages still exist. These designs have limited motion ranges, and their linear ranges is even more limited. Pull-in effect is hard to avoid for comb-drive actuators. Some requirements (e.g., structural simplicity and DOF) contradict one another, and thus compromises must be made. Despite these negative factors, micropositioners remain irreplaceable in position/attitude control.

2.4 Force-Controlled Robotic Micromanipulation and its Applications

2.4.1 Force Control Strategies in Robotic Micromanipulation

The purpose of current force-controlled micromanipulation tasks could fall into two categories [83]. One is to regulate the impact force between sample and end effector [2, 84, 85], and the other is to maintain a certain force level for secured micrograsping [86, 87].

In the case of the impact force regulation, both position and force information are needed. One common approach is to switch between position control and force control [84, 85]. The switching signal is usually based on position and force signals to avoid causing damage to the sample or to the end effector. These two signals also serve as the input of controllers. The controller switch is triggered when the end effector is close enough to the sample, or the interactive force exceeds a threshold value. In addition to this conventional strategy, position-force hybrid control is investigated in [88].

In the case of gripping force control, position feedback may not be needed, but model-based analysis of the sample is imperative to achieve satisfying control performance and to avoid damaging the sample. Frequency domain analysis is adopted [89] where the principal component is acquired via step response, then the controller could be designed with mature linear system theories. Time domain analysis is another useful approach when the system demonstrates nonlinearity [87] and uncertainty [90]. The advance in nonlinear and time dependent system theories in the last few decades significantly helped to tackle robotic micromanipulation systems that could not be

treated as linear time invariant systems, such as thermally actuated grippers [91] and actuators with hysteresis effects [92].

One fact to notice is that force feedback alone is not enough for force control. Position signal is used in a variety of control architectures [93, 94, 95]. Different methods are developed to acquire position signal. Direct vision position feedback via microscope cameras is straightforward and is commonly used [15, 96, 14]. Ultrasonic measurement is employed when vision is difficult to implement [97], but the equipment is usually costly. When using a micromanipulator with stepper motor or encoded DC motor, position feedback could be directly acquired by assuming that the deformation of end effector could be neglected. End effector deformation could be indirectly measured via displacement augmentation approach such as by measuring the deflection angle of laser reflected from a cantilever beam [98], or by calculating the position signal from force signal [99] if the mechanical model of the system is reliable.

2.4.2 Applications of Force-Controlled Micromanipulation

2.4.2.1 Force-Controlled Micro and Nanoassembly

Micro and nanoassmbly represent a typical example of force-controlled robotic micromanipulation. The major objective of the control task in micro and nanoassembly is position control. However, the force control serves as an important inner loop to push an micro-object to a desired location. Pushing directly in an open-loop manner always cause the object to be damaged. In [100, 84], AFM cantilever tips are employed to push nanoparticles with traditional linear analysis in frequency domain. In [88], hybrid control is adopted for successful insertion. Given the lack of position feedback due to the difficulty in implementing a position sensor, multi-probe approach was investigated in [101]. In [102], active force control is implemented to guide a particle along a desired trajectory.

2.4.2.2 Force-Controlled MEMS Grasping Tools

MEMS grasping tools such as micro and nanogrippers, featuring two gripping arms, guarantee more reliable and controlled manipulation when operating in air and liquid environments [103]. With microfabricated position and force sensors, the relative displacement of arms and the

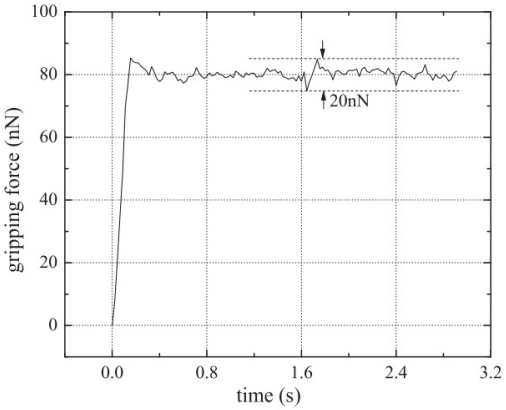

Figure 2–6: Force control result of a MEMS grasping tool, adapted from [106].

resultant force could be measured, from which the mechanical parameters of the object being manipulated could even be deducted. Early designs of MEMS grippers usually do not include force sensors [104, 105]. Recently, for more dexterous manipulation of fragile micro-objects, especially for soft materials, some new ideas emerge to perform closed-loop force control on MEMS grippers, and force sensing ranges from micronewton [103] to nanonewton level [26, 106]. The steady state oscillation could be as small as 10 nN (Fig. 2–6). Two-axis force-controlled gripper for shear and compressive force control are realized in [86], for elastic and viscoelastic characterization of soft materials. In addition to soft materials, closed-loop force control for hard material is studied in [95]. Conventionally, only elastic properties are analyzed. However, viscoelastic properties are being paid increasing attention and are successfully extracted in [86]. Besides force control, closed-loop positioning control are investigated in [107] to minimize tip gaps.

2.4.2.3 Automated Cell Microinjection with Injection Force Control

Cell injection plays an important role in biological studies, with applications in various areas such as *in vitro* fertilization, sperm injection and drug development. Continuous efforts have been made to automate the cell injection process. Manual injection efficiency relies heavily on operators' skills and experience. The early stage of automated injection was focused on improving efficiency over manual injection [108, 109]. Commercial open loop injection systems were introduced to the market for adherent cells but survival rate of injected cells was not satisfactory [12]. Since

2000, more attentions have been placed on improving the survival rate. Open-loop visual-assisted monitoring and closed-loop force control are used in [12, 110] to improve the survival rate of suspended cells after robotic injection. Sensorless force control using reaction torque observer is demonstrated in [111] to reduce overall cost.

2.5 Issues with Force Control in Robotic Micromanipulation

Despite the wide application of force control in robotic micromanipulation systems, the complexity of micromanipulation generates several difficulties that makes the force controller barely work perfectly. The major difficulties are summarized as follows.

2.5.1 Modeling Error

Modeling error is defined as the difference between a real model and the ideal model. Modeling errors have multiple origins. For thermal actuators, errors could come from system linearization because some actuators are nonlinear [112]. Parameter inaccuracy also contributes to the total modeling errors [113]. Environmental disturbance often results in periodic errors [114]. Model deterioration provokes slow varying errors, such as applying a pure elastic model on viscoelastic system [115]. Modeling errors make model based control schemes, such as MPC (model predictive control) [116] and feed forward compensation [94] less effective.

2.5.2 Time Delay

Time delay is defined as the time interval between the control input and the response of the system. Typical sources of time delay could be attributed to the data transfer through comports, the back lash of mechanics, and the physical properties of test subjects [112], and so on. Time delay deteriorates control system performance, and even destabilizes the system completely. Note that failure to accurately measure the time delay could also be treated as an inaccuracy of parameter, making some overlap between time delays and modeling errors.

2.5.3 Insufficient Feedback

Modern controllers may require multiple feedback modalities. For instance, H-infinity controller requires the displacement of end effector [99]. Such information may not be viable due to lack of position feedback in some robotic micromanipulation systems. This lack of information

also reduces the controllability and observability of the system [117]. Some advanced actuators have built-in sensors but its cost is also significantly increased, which is not viable through normal commercial silicon based fabrication services. Solving this problem is meaningful for academic and commercial purposes.

2.5.4 Measurement Noise

Measurement noise is defined as the white noise (whose average is 0) in the measurement. Measurement noise is always generated by hardware and environmental disturbance. Measurement noise makes calculating the time derivative of signal difficult, while the time derivative is often used in controllers, such as PID controller, MPC controller and fuzzy controller.

2.5.5 Nonlinearity

Real control problems always include non-linearity. In this case, the system dynamics could not be written in linear differential equations, transfer functions do not exist, and methods based on frequency domain could not be applied.

2.6 Commonly Used Force Control Architectures

The common issues (modeling error, time delay, measurement noise and insufficient feedback) always appear in the same control problem simultaneously. Some approaches have been investigated to tackle some of these issues when others do not exist, but no approach could tackle all these issues simultaneously.

The most common way is to ignore details of the system model and implement a simple proportional-integral-derivative (PID) controller, which guarantees zero static error. However, because the system dynamics is not considered in the controller design and the time delay exists, the PID controller usually leads to large overshoots [86]. By tuning the PID coefficients, the overshoot may be reduced but settling time is also sacrificed [118]. The Smith predictor is ideal to treat the time-delay effect of control systems which a secondary loop to neutralize the effect of the delay block e^{-Ls}, but requires a precise time invariant model [119, 120], which is unsuitable for our case here because unknown modeling errors exist in the robotic micromanipulation systems. Another method is to ignore modeling errors completely to obtain a simplified linear system, and

analyze it in frequency domain [121]. However, this method leads to long settling time and static state oscillations.

Another common method to compensate for unknown system parameters and modeling errors is to implement an extended high gain observer (EHGO) [122]. Conventional EGHOs are difficult to use for force control in robotic micromanipulation, because small force signals are always noisy whereas conventional EHGOs are very sensitive to noise in feedback [123, 124].

Advanced control schemes have also been proposed for a variety of robotic micromanipulation systems. H-infinity and μ-synthesis were investigated in [99] to account for modeling errors of piezoelectric microactuators. These methods require the feedback of the actuator output, which can not be implemented in systems with sensorless actuators. Gain scheduling was adopted in [113] to adaptively compensate for system nonlinearity, but modeling errors were neglected in this study. In [125], unknown terms were estimated during the initial step of control system. This method could only treat constant modeling errors, and causes large overshoot during each estimation. In [93], an iterative procedure, based on an eigenstructure assignment methodology coupled with auto-scheduling, was proposed to treat model uncertainties.

In [94], a fuzzy-PID controller with feedforward compensation was adopted to account for model uncertainties. However, in these two systems [93, 94], only simulations were conducted and no real control experiments were demonstrated. In [95], a sliding mode controller was employed for a gripper system to compensate for uncertainties, but the system was only tested on a hard material (copper) without any effect of the material compliance (e.g., elasticity and viscoelasticity). In our case, soft materials are manipulated and the slow dynamics of these soft materials will bring in additional uncertainties in the control system. Besides, this work does not involve time delay. Passive bilateral control was investigated in [126] to account for time delays, but this approach showed large steady state errors. Moreover, all control methods introduced above fail to account for time-varying modeling errors, time delays, and feedback measurement noises simultaneously.

Due to the aforementioned issues commonly existing in force control for robotic micromanipulation, new control schemes are highly desired to tackle these challenges simultaneously and improve the control system performance.

2.7 Conclusion

Robotic micromanipulation systems significantly improve the efficiency and accuracy of manipulation tasks compared to manual operations. Force sensing and control are widely used to improve system performance for increasingly demanding micromanipulation tasks, such as micro- and nanoassembly, force-controlled grasping, and automated cell injection. Due to the complexity of micromanipulation systems, there are several factors that hinder the force control performance, including modeling error, time delay, measurement noise, insufficient feedback and nonlinearity. No existing control strategies could tackle all these problems altogether, and new control schemes are highly desired.

References

[1] Z. Lu, P. C. Chen, and W. Lin, "Optimization of hamiltonian algorithm for fiber alignment by simulation and experiments," *Opt. Eng.*, vol. 44, no. 7, pp. 075 002–075 002, 2005.

[2] G. Yang, J. A. Gaines, and B. J. Nelson, "A flexible experimental workcell for efficient and reliable wafer-level 3d micro-assembly," in *Robotics and Automation, 2001. Proceedings 2001 ICRA. IEEE International Conference on*, IEEE, vol. 1, 2001, pp. 133–138.

[3] T. Kasaya, H. T. Miyazaki, S. Saito, and T. Sato, "Micro-object handling under sem by vision-based automatic control," in *Photonics East (ISAM, VVDC, IEMB)*, International Society for Optics and Photonics, 1998, pp. 181–192.

[4] H.-H. Pham, H.-C. Yeh, and I.-M. Chen, "Micromanipulation system design based on selective actuation mechanisms," *Int. J. Robot. Res.*, vol. 25, no. 2, pp. 171–186, 2006.

[5] J. White, D. Thesier, J. Swain, M. Katz, C Tomasulo, A Henderson, L Wang, C Yarnall, A Fargnoli, M Sumaroka, et al., "Myocardial gene delivery using molecular cardiac surgery with recombinant adeno-associated virus vectors in vivo," *Gene Ther.*, vol. 18, no. 6, pp. 546–552, 2011.

[6] M. Nonnenmacher and T. Weber, "Intracellular transport of recombinant adeno-associated virus vectors," *Gene Ther.*, vol. 19, no. 6, pp. 649–658, 2012.

[7] E. Enlund, S. Fischer, R. Handrick, K. Otte, K.-M. Debatin, M. Wabitsch, and P. Fischer-Posovszky, "Establishment of lipofection for studying mirna function in human adipocytes," *PLoS ONE*, vol. 9, no. 5, e98023, 2014.

[8] J. C. Weaver and Y. A. Chizmadzhev, "Theory of electroporation: a review," *Bioelectrochem. Bioenerg.*, vol. 41, no. 2, pp. 135–160, 1996.

[9] J. C. Weaver, "Electroporation of cells and tissues," vol. 28, no. 1, pp. 24–33, 2000.

[10] K. Sakaki, N. Dechev, R. D. Burke, and E. J. Park, "Development of an autonomous biological cell manipulator with single-cell electroporation and visual servoing capabilities," *IEEE Trans. Biomed. Eng.*, vol. 56, no. 8, pp. 2064–2074, 2009.

[11] Y. Zhang and L.-C. Yu, "Microinjection as a tool of mechanical delivery," *Curr. Opin. Biotechnol.*, vol. 19, no. 5, pp. 506–510, 2008.

[12] Y. Sun and B. J. Nelson, "Biological cell injection using an autonomous microrobotic system," *Int. J. Robot. Res.*, vol. 21, no. 10-11, pp. 861–868, 2002.

[13] Z. Lu, X. Zhang, C. Leung, N. Esfandiari, R. F. Casper, and Y. Sun, "Robotic icsi (intracytoplasmic sperm injection)," *IEEE Trans. Biomed. Eng.*, vol. 58, no. 7, pp. 2102–2108, 2011.

[14] W. Wang, X. Y. Liu, D. Gelinas, B. Ciruna, and Y. Sun, "A fully automated robotic system for microinjection of zebrafish embryos," *PLoS ONE*, vol. 2, no. 9, e862, 2007.

[15] X. Liu, R. Fernandes, M. Gertsenstein, A. Perumalsamy, I. Lai, M. Chi, K. H. Moley, E. Greenblatt, I. Jurisica, R. F. Casper, et al., "Automated microinjection of recombinant bcl-x into mouse zygotes enhances embryo development," *PLoS ONE*, vol. 6, no. 7, e21687, 2011.

[16] H. B. Huang, D. Sun, J. K. Mills, and S. H. Cheng, "Robotic cell injection system with position and force control: toward automatic batch biomanipulation," *IEEE Trans. Robot.*, vol. 25, no. 3, pp. 727–737, 2009.

[17] S. Zappe, M. Fish, M. P. Scott, and O. Solgaard, "Automated mems-based drosophila embryo injection system for high-throughput rnai screens," *Lab. Chip*, vol. 6, no. 8, pp. 1012–1019, 2006.

[18] R. W. Bernstein, M. Scott, and O. Solgaard, "Biomems for high-throughput handling and microinjection of embryos," in *Photonics Asia 2004*, International Society for Optics and Photonics, 2004, pp. 67–73.

[19] R. W. Bernstein, X. Zhang, S. Zappe, M. Fish, M. Scott, and O. Solgaard, "Positioning and immobilization of drosophila embryos in 2-d arrays for drug injection," in *Micro Total Analysis Systems 2002*, Springer, 2002, pp. 793–795.

[20] X. Wang, S. Chen, M. Kong, Z. Wang, K. D. Costa, R. A. Li, and D. Sun, "Enhanced cell sorting and manipulation with combined optical tweezer and microfluidic chip technologies," *Lab. Chip*, vol. 11, no. 21, pp. 3656–3662, 2011.

[21] P. J. Lee, P. J. Hung, R. Shaw, L. Jan, and L. P. Lee, "Microfluidic application-specific integrated device for monitoring direct cell-cell communication via gap junctions between individual cell pairs," *Appl. Phys. Lett.*, vol. 86, no. 22, p. 223 902, 2005.

[22] R. W. Steubing, S. Cheng, W. H. Wright, Y. Numajiri, and M. W. Berns, "Laser induced cell fusion in combination with optical tweezers: the laser cell fusion trap," *Cytometry*, vol. 12, no. 6, pp. 505–510, 1991.

[23] A. P. Vijayasai, G. Sivakumar, M. Mulsow, S. Lacouture, A. Holness, and T. E. Dallas, "Haptic controlled three-axis mems gripper system," *Rev. Sci. Instrum.*, vol. 81, no. 10, p. 105 114, 2010.

[24] N. Chronis and L. P. Lee, "Electrothermally activated su-8 microgripper for single cell manipulation in solution," *J. Microelectromech. Syst.*, vol. 14, no. 4, pp. 857–863, 2005.

[25] F. Beyeler, A. Neild, S. Oberti, D. J. Bell, Y. Sun, J. Dual, and B. J. Nelson, "Monolithically fabricated microgripper with integrated force sensor for manipulating microobjects and biological cells aligned in an ultrasonic field," *J. Microelectromech. Syst.*, vol. 16, no. 1, pp. 7–15, 2007.

[26] K. Kim, X. Liu, Y. Zhang, and Y. Sun, "Nanonewton force-controlled manipulation of biological cells using a monolithic mems microgripper with two-axis force feedback," *J. Micromech. Microeng.*, vol. 18, no. 5, p. 055 013, 2008.

[27] T. G. Leong, C. L. Randall, B. R. Benson, N. Bassik, G. M. Stern, and D. H. Gracias, "Tetherless thermobiochemically actuated microgrippers," *Proceedings of the National Academy of Sciences*, vol. 106, no. 3, pp. 703–708, 2009.

[28] M. Takeuchi, M. Nakajima, M. Kojima, and T. Fukuda, "Probe device for soft handling of single cells using thermoresponsive polymer," in *Robotics and Automation (ICRA), 2011 IEEE International Conference on*, IEEE, 2011, pp. 3163–3168.

[29] Z. Lu, C. Moraes, G. Ye, C. A. Simmons, and Y. Sun, "Single cell deposition and patterning with a robotic system," *PLoS ONE*, vol. 5, no. 10, e13542, 2010.

[30] K. Zhang, X. Han, Y. Li, S. Y. Li, Y. Zu, Z. Wang, and L. Qin, "Hand-held and integrated single-cell pipettes," *J. Am. Chem. Soc.*, vol. 136, no. 31, pp. 10 858–10 861, 2014.

[31] S. Hu and D. Sun, "Automated transportation of single cells using robot-tweezer manipulation system," *Journal of the Association for Laboratory Automation*, vol. 16, no. 4, pp. 263–270, 2011.

[32] E. B. Steager, M. S. Sakar, C. Magee, M. Kennedy, A. Cowley, and V. Kumar, "Automated biomanipulation of single cells using magnetic microrobots," *Int. J. Robot. Res.*, vol. 32, no. 3, pp. 346–359, 2013.

[33] Z. Ye and M. Sitti, "Dynamic trapping and two-dimensional transport of swimming microorganisms using a rotating magnetic microrobot," *Lab. Chip*, vol. 14, no. 13, pp. 2177–2182, 2014.

[34] G. G. Ernstrom and M. Chalfie, "Genetics of sensory mechanotransduction," *Annu. Rev. Genet.*, vol. 36, no. 1, pp. 411–453, 2002.

[35] A. P. Jarman, "Studies of mechanosensation using the fly," *Hum. Mol. Gen.*, vol. 11, no. 10, pp. 1215–1218, 2002.

[36] Y. Zhou, S. Cameron, W.-T. Chang, Y. Rao, et al., "Control of directional change after mechanical stimulation in drosophila," *Mol. Brain*, vol. 5, no. 1, pp. 39–51, 2012.

[37] R. Y. Hwang, L. Zhong, Y. Xu, T. Johnson, F. Zhang, K. Deisseroth, and W. D. Tracey, "Nociceptive neurons protect drosophila larvae from parasitoid wasps," *Curr. Biol.*, vol. 17, no. 24, pp. 2105–2116, 2007.

[38] A. Tsubouchi, J. C. Caldwell, and W. D. Tracey, "Dendritic filopodia, ripped pocket, nompc, and nmdars contribute to the sense of touch in drosophila larvae," *Curr. Biol.*, vol. 22, no. 22, pp. 2124–2134, 2012.

[39] Z. Yan, W. Zhang, Y. He, D. Gorczyca, Y. Xiang, L. E. Cheng, S. Meltzer, L. Y. Jan, and Y. N. Jan, "Drosophila nompc is a mechanotransduction channel subunit for gentle-touch sensation," *Nature*, vol. 493, no. 7431, pp. 221–225, 2013.

[40] F. Arai, D. Andou, and T. Fukuda, "Adhesion forces reduction for micro manipulation based on micro physics," in *Micro Electro Mechanical Systems, 1996, MEMS'96, Proceedings. An Investigation of Micro Structures, Sensors, Actuators, Machines and Systems. IEEE, The Ninth Annual International Workshop on*, IEEE, 1996, pp. 354–359.

[41] S. Fahlbusch, S. Fatikow, and K. Santa, "Force sensing in microrobot systems: an overview," in *Advances in Manufacturing*, Springer, 1999, pp. 233–244.

[42] S Tadigadapa and K Mateti, "Piezoelectric mems sensors: state-of-the-art and perspectives," *Meas. Sci. Technol.*, vol. 20, no. 9, p. 092 001, 2009.

[43] N Setter, D Damjanovic, L Eng, G Fox, S. Gevorgian, S Hong, A Kingon, H Kohlstedt, N. Park, G. Stephenson, et al., "Ferroelectric thin films: review of materials, properties, and applications," *J. Appl. Phys.*, vol. 100, no. 5, p. 051 606, 2006.

[44] S. Trolier-McKinstry and P. Muralt, "Thin film piezoelectrics for mems," *Journal of Electroceramics*, vol. 12, no. 1-2, pp. 7–17, 2004.

[45] C. Yao, Y. Qi, Y. Zhao, Y. Xiang, Q. Chen, and W. Fu, "Aptamer-based piezoelectric quartz crystal microbalance biosensor array for the quantification of ige," *Biosens. Bioelectron.*, vol. 24, no. 8, pp. 2499–2503, 2009.

[46] J. Sirohi and I. Chopra, "Fundamental understanding of piezoelectric strain sensors," *Journal of Intelligent Material Systems and Structures*, vol. 11, no. 4, pp. 246–257, 2000.

[47] S. R. Moheimani and A. J. Fleming, *Piezoelectric transducers for vibration control and damping*. Springer Science & Business Media, 2006.

[48] K. Uchino, *Piezoelectric actuators and ultrasonic motors*. Springer Science & Business Media, 1996, vol. 1.

[49] T. J. Johnson, D. Charnegie, W. W. Clark, M. Buric, and G. Kusic, "Energy harvesting from mechanical vibrations using piezoelectric cantilever beams," in *smart structures and materials*, International Society for Optics and Photonics, 2006, pp. 61690D–61690D.

[50] A. A. Barlian, W.-T. Park, J. R. Mallon Jr, A. J. Rastegar, and B. L. Pruitt, "Review: semiconductor piezoresistance for microsystems," vol. 97, no. 3, pp. 513–552, 2009.

[51] Y. Kanda, "Piezoresistance effect of silicon," *Sensor. Actuat. A-Phys.*, vol. 28, no. 2, pp. 83–91, 1991.

[52] R. He and P. Yang, "Giant piezoresistance effect in silicon nanowires," *Nature nanotechnology*, vol. 1, no. 1, pp. 42–46, 2006.

[53] X. Liu, M. Mwangi, X. Li, M. O'Brien, and G. M. Whitesides, "Paper-based piezoresistive mems sensors," *Lab. Chip*, vol. 11, no. 13, pp. 2189–2196, 2011.

[54] R. J. Roark and W. C. Young, *Formulas for stress and strain*. McGraw-Hill, 1975.

[55] R. Wilfinger, P. Bardell, and D. Chhabra, "The resonistor: a frequency selective device utilizing the mechanical resonance of a silicon substrate," *IBM Journal of Research and Development*, vol. 12, no. 1, pp. 113–118, 1968.

[56] D. J. Beebe, A. S. Hsieh, D. D. Denton, and R. G. Radwin, "A silicon force sensor for robotics and medicine," *Sensor. Actuat. A-Phys.*, vol. 50, no. 1, pp. 55–65, 1995.

[57] D. Jin, X. Li, J. Liu, G. Zuo, Y. Wang, M. Liu, and H. Yu, "High-mode resonant piezoresistive cantilever sensors for tens-femtogram resoluble mass sensing in air," *J. Micromech. Microeng.*, vol. 16, no. 5, p. 1017, 2006.

[58] A Hierlemann, D Lange, C Hagleitner, N Kerness, A Koll, O Brand, and H Baltes, "Application-specific sensor systems based on cmos chemical microsensors," *Sensors and Actuators B: Chemical*, vol. 70, no. 1, pp. 2–11, 2000.

[59] D. Lange, C Hagleitner, O Brand, and H Baltes, "Cmos resonant beam gas sensing system with on-chip self excitation," in *Micro Electro Mechanical Systems, 2001. MEMS 2001. The 14th IEEE International Conference on*, IEEE, 2001, pp. 547–552.

[60] A. Boisen, J. Thaysen, H. Jensenius, and O. Hansen, "Environmental sensors based on micromachined cantilevers with integrated read-out," *Ultramicroscopy*, vol. 82, no. 1, pp. 11–16, 2000.

[61] H. Jensenius, J. Thaysen, A. A. Rasmussen, L. H. Veje, O. Hansen, and A. Boisen, "A microcantilever-based alcohol vapor sensor-application and response model," *Appl. Phys. Lett.*, vol. 76, no. 18, pp. 2615–2617, 2000.

[62] D. R. Baselt, G. U. Lee, K. M. Hansen, L. A. Chrisey, and R. J. Colton, "A high-sensitivity micromachined biosensor," vol. 85, no. 4, pp. 672–680, 1997.

[63] R. Marie, H. Jensenius, J. Thaysen, C. B. Christensen, and A. Boisen, "Adsorption kinetics and mechanical properties of thiol-modified dna-oligos on gold investigated by microcantilever sensors," *Ultramicroscopy*, vol. 91, no. 1, pp. 29–36, 2002.

[64] P. Rasmussen, J. Thaysen, O. Hansen, S. Eriksen, and A. Boisen, "Optimised cantilever biosensor with piezoresistive read-out," *Ultramicroscopy*, vol. 97, no. 1, pp. 371–376, 2003.

[65] C. S. Smith, "Piezoresistance effect in germanium and silicon," *Phys. Rev.*, vol. 94, no. 1, p. 42, 1954.

[66] D. Bittle, J. Suhling, R. Beaty, R. Jaeger, and R. Johnson, "Piezoresistive stress sensors for structural analysis of electronic packages," *Journal of Electronic Packaging*, vol. 113, no. 3, pp. 203–215, 1991.

[67] P Ruther and M Wandt, "Innovativer miniaturisierter 3d-kraftsensor für koordinatenmesssysteme von mikrokomponenten," *Sensor Maganzin*, pp. 30–33, 2008.

[68] P. J. Kyberd and P. H. Chappell, "A force sensor for automatic manipulation based on the hall effect," *Meas. Sci. Technol.*, vol. 4, no. 3, p. 281, 1993.

[69] J. Paulsen, A. Ring, C. Lo, J. E. Snyder, and D. Jiles, "Manganese-substituted cobalt ferrite magnetostrictive materials for magnetic stress sensor applications," *J. Appl. Phys.*, vol. 97, no. 4, p. 044 502, 2005.

[70] F. Carignan, *Displacement/force transducers utilizing hall effect sensors*, US Patent 5,339,699, 1994. [Online]. Available: https://www.google.com/patents/US5339699.

[71] M. Demierre, E. Schurig, C. Schott, P.-A. Besse, and R. S. Popović, "Contactless 360 absolute angular cmos microsystem based on vertical hall sensors," *Sensor. Actuat. A-Phys.*, vol. 116, no. 1, pp. 39–44, 2004.

[72] P. Ouyang, R. Tjiptoprodjo, W. Zhang, and G. Yang, "Micro-motion devices technology: the state of arts review," *Int. J. Adv. Manuf. Tech.*, vol. 38, no. 5-6, pp. 463–478, 2008.

[73] S. Verma, W. jong Kim, and H. Shakir, "Multi-axis maglev nanopositioner for precision manufacturing and manipulation applications," *IEEE Transactions on Industry Applications*, vol. 41, no. 5, pp. 1159–1167, 2005, ISSN: 0093-9994. DOI: 10.1109/TIA.2005.853374.

[74] M. B. Khamesee, N. Kato, Y. Nomura, and T. Nakamura, "Design and control of a microrobotic system using magnetic levitation," *IEEE/ASME Transactions on Mechatronics*, vol. 7, no. 1, pp. 1–14, 2002, ISSN: 1083-4435. DOI: 10.1109/3516.990882.

[75] M. Mehrtash, N. Tsuda, and M. B. Khamesee, "Bilateral macro–micro teleoperation using magnetic levitation," *IEEE/ASME Trans. Mechatron.*, vol. 16, no. 3, pp. 459–469, 2011.

[76] E. Shameli, M. B. Khamesee, and J. P. Huissoon, "Real-time control of a magnetic levitation device based on instantaneous modeling of magnetic field," *Mechatronics*, vol. 18, no. 10, pp. 536–544, 2008.

[77] S. C. Jacobsen, J. E. Wood, and R. H. Price, *Micropositioner systems and methods*, US Patent 4,789,803, 1988.

[78] S. H. Yang, Y.-S. Kim, J.-M. Yoo, and N. G. Dagalakis, "Microelectromechanical systems based stewart platform with sub-nano resolution," *Appl. Phys. Lett.*, vol. 101, no. 6, p. 061 909, 2012.

[79] N. G. Dagalakis and E. Amatucci, "Kinematic modeling of a 6 degree of freedom tri-stage micro-positioner," in *Proceedings of ASPE 16th Annual Meeting, Crystal City, VA*, Citeseer, 2001.

[80] Y. Sun, D Piyabongkarn, A Sezen, B. Nelson, and R Rajamani, "A high-aspect-ratio two-axis electrostatic microactuator with extended travel range," *Sensor. Actuat. A-Phys.*, vol. 102, no. 1, pp. 49–60, 2002.

[81] M. A. Lantz, H. E. Rothuizen, U. Drechsler, W. Häberle, and M. Despont, "A vibration resistant nanopositioner for mobile parallel-probe storage applications," *J. Microelectromech. Syst.*, vol. 16, no. 1, pp. 130–139, 2007.

[82] B. R. De Jong, D. M. Brouwer, M. J. De Boer, H. V. Jansen, H. M. Soemers, and G. J. Krijnen, "Design and fabrication of a planar three-dofs mems-based manipulator," *J. Microelectromech. Syst.*, vol. 19, no. 5, pp. 1116–1130, 2010.

[83] Z. Lu, P. C. Chen, and W. Lin, "Force sensing and control in micromanipulation," *IEEE Trans. Syst., Man, Cybern. C, Appl. Rev.*, vol. 36, no. 6, pp. 713–724, 2006.

[84] Y. Shen, N. Xi, and W. J. Li, "Contact and force control in microassembly," in *Assembly and Task Planning, 2003. Proceedings of the IEEE International Symposium on*, 2003, pp. 60–65. DOI: 10.1109/ISATP.2003.1217188.

[85] Y. Zhou, B. J. Nelson, and B. Vikramaditya, "Fusing force and vision feedback for micromanipulation," in *Robotics and Automation, 1998. Proceedings. 1998 IEEE International Conference on*, IEEE, vol. 2, 1998, pp. 1220–1225.

[86] J. Qu, W. Zhang, A. Jung, S. Sliva, and X. Liu, "A MEMS microgripper with two-axis actuators and force sensors for microscale mechanical characterization of soft materials," in *2015 IEEE International Conference on Automation Science and Engineering (CASE)*, 2015.

[87] M. Boudaoud, Y. Haddab, and Y. Le Gorrec, "Modeling and optimal force control of a nonlinear electrostatic microgripper," *IEEE/ASME Trans. Mechatron.*, vol. 18, no. 3, pp. 1130–1139, 2013.

[88] Y. Li, "Hybrid control approach to the peg-in hole problem," *IEEE Robotics Automation Magazine*, vol. 4, no. 2, pp. 52–60, 1997, ISSN: 1070-9932. DOI: 10.1109/100.591646.

[89] A Eisinberg, A Menciassi, S Micera, D Campolo, M. Carrozza, and P Dario, "Pi force control of a microgripper for assembling biomedical microdevices," *IEE P-Circ. Dev. Syst.*, vol. 148, no. 6, pp. 348–352, 2001.

[90] Q. Xu, "Adaptive discrete-time sliding mode impedance control of a piezoelectric microgripper," *IEEE Trans. Robot.*, vol. 29, no. 3, pp. 663–673, 2013.

[91] H. Zhang, Y. Bellouard, E. Burdet, R. Clavel, A.-N. Poo, and D. Hutamacher, "Shape memory alloy microgripper for robotic microassembly of tissue engineering scaffolds," in *Robotics and Automation, 2004. Proceedings. ICRA'04. 2004 IEEE International Conference on*, IEEE, vol. 5, 2004, pp. 4918–4924.

[92] M. Rakotondrabe, "Bouc-wen modeling and inverse multiplicative structure to compensate hysteresis nonlinearity in piezoelectric actuators.," *IEEE Trans. Autom. Sci. Eng.*, vol. 8, no. 2, pp. 428–431, 2011.

[93] M. Boudaoud, M. G. De Faria, Y. Haddab, S. Haliyo, Y. Le Gorrec, P. Lutz, and S. Régnier, "Robust microscale grasping using a self scheduled dynamic controller," in *World Congress*, vol. 19, 2014, pp. 7492–7498.

[94] Z. Chi, M. Jia, and Q. Xu, "Fuzzy pid feedback control of piezoelectric actuator with feedforward compensation," *Math. Probl. Eng.*, vol. 2014, 2014.

[95] Q. Xu, "Design and smooth position/force switching control of a miniature gripper for automated microhandling," *IEEE Trans. Ind. Informat.*, vol. 10, no. 2, pp. 1023–1032, 2014, ISSN: 1551-3203. DOI: 10.1109/TII.2013.2290895.

[96] X. Liu, Z. Lu, and Y. Sun, "Orientation control of biological cells under inverted microscopy," *IEEE/ASME Tran. Mechatron.*, vol. 16, no. 5, pp. 918–924, 2011.

[97] F Tatar, J. Mollinger, R. Den Dulk, W. van Duyl, J. Goosen, and A Bossche, "Ultrasonic sensor system for measuring position and orientation of laproscopic instruments in minimal invasive surgery," in *Microtechnologies in Medicine & Biology 2nd Annual International IEEE-EMB Special Topic Conference on*, IEEE, 2002, pp. 301–304.

[98] G. Binnig, C. F. Quate, and C. Gerber, "Atomic force microscope," *Phys. Rev. Lett.*, vol. 56, no. 9, p. 930, 1986.

[99] S. Khadraoui, M. Rakotondrabe, and P. Lutz, "Interval modeling and robust control of piezoelectric microactuators," *IEEE Trans. Control Syst. Technol.*, vol. 20, no. 2, pp. 486–494, 2012.

[100] M. Sitti and H. Hashimoto, "Controlled pushing of nanoparticles: modeling and experiments," *IEEE/ASME Trans. Mechatron.*, vol. 5, no. 2, pp. 199–211, 2000, ISSN: 1083-4435. DOI: 10.1109/3516.847093.

[101] J. Wason, W. Gressick, J. T. Wen, J. Gorman, and N. Dagalakis, "Multi-probe microassembly," in *2007 IEEE International Conference on Automation Science and Engineering*, 2007, pp. 63–68. DOI: 10.1109/COASE.2007.4341814.

[102] K. Rabenorosoa, C. Clvy, and P. Lutz, "Active force control for robotic micro-assembly: application to guiding tasks," in *Robotics and Automation (ICRA), 2010 IEEE International Conference on*, 2010, pp. 2137–2142. DOI: 10.1109/ROBOT.2010.5509863.

[103] K. Kim, X. Liu, Y. Zhang, and Y. Sun, "Micronewton force-controlled manipulation of biomaterials using a monolithic mems microgripper with two-axis force feedback," in *Robotics and Automation, 2008. ICRA 2008. IEEE International Conference on*, IEEE, 2008, pp. 3100–3105.

[104] W.-H. M. Chu, "Microfabricated tweezers with a large gripping force and a large range of motion," PhD thesis, Case Western Reserve University, 1994.

[105] M Kohl, E Just, W Pfleging, and S Miyazaki, "Sma microgripper with integrated antagonism," *Sensor. Actuat. A-Phys.*, vol. 83, no. 1, pp. 208–213, 2000.

[106] X. Y. Liu, K. Kim, Y. Zhang, and Y. Sun, "Nanonewton force sensing and control in microrobotic cell manipulation," *Int. J. Robot. Res.*, vol. 28, no. 8, pp. 1065–1076, 2009.

[107] B. Komati, K. Rabenorosoa, C. Clévy, and P. Lutz, "Automated guiding task of a flexible micropart using a two-sensing-finger microgripper," *IEEE Trans. Autom. Sci. Eng.*, vol. 10, no. 3, pp. 515–524, 2013.

[108] T. Huang, Y. Kimura, and R. Yanagimachi, "The use of piezo micromanipulation for intracytoplasmic sperm injection of human oocytes," *J. Assist. Reprod. Genet.*, vol. 13, no. 4, pp. 320–328, 1996.

[109] U. Koch and A Büschges, "A high speed recoil-free piezo-drive for cell impalement," *J. Neurosci. Methods*, vol. 35, no. 3, pp. 261–265, 1990.

[110] Y. Xie, D. Sun, H. Y. G. Tse, C. Liu, and S. H. Cheng, "Force sensing and manipulation strategy in robot-assisted microinjection on zebrafish embryos," *IEEE/ASME Trans. Mechatron.*, vol. 16, no. 6, pp. 1002–1010, 2011.

[111] Y. Ohba, M. Sazawa, K. Ohishi, T. Asai, K. Majima, Y. Yoshizawa, and K. Kageyama, "Sensorless force control for injection molding machine using reaction torque observer considering torsion phenomenon," *IEEE Tran. Ind. Electron.*, vol. 56, no. 8, pp. 2955–2960, 2009, ISSN: 0278-0046. DOI: 10.1109/TIE.2009.2024444.

[112] W. Zhang, X. Dong, and X. Liu, "Switched fuzzy-pd control of contact forces in robotic micromanipulation of drosophila larvae," in *2015 IEEE International Conference on Robotics and Automation (ICRA)*, 2015.

[113] M. Boudaoud, Y. Le Gorrec, Y. Haddab, and P. Lutz, "Gain scheduling control of a nonlinear electrostatic microgripper: design by an eigenstructure assignment with an observer-based structure," *IEEE Trans. Control Syst. Technol.*, vol. 23, no. 4, pp. 1255–1267, 2015, ISSN: 1063-6536. DOI: 10.1109/TCST.2014.2362725.

[114] M. Rakotondrabe, Y. Haddab, and P. Lutz, "Quadrilateral modelling and robust control of a nonlinear piezoelectric cantilever," *IEEE Trans. Control Syst. Technol.*, vol. 17, no. 3, pp. 528–539, 2009.

[115] M. Vandamme and F.-J. Ulm, "Viscoelastic solutions for conical indentation," *Int. J. Solids. Struct.*, vol. 43, no. 10, pp. 3142–3165, 2006.

[116] C. E. Garcia, D. M. Prett, and M. Morari, "Model predictive control: theory and practicea survey," *Automatica*, vol. 25, no. 3, pp. 335–348, 1989.

[117] S. Chakrabarti, E. Kyriakides, and D. G. Eliades, "Placement of synchronized measurements for power system observability," *IEEE Trans. Power Del.*, vol. 24, no. 1, pp. 12–19, 2009.

[118] P. Klan and R Gorez, "PI controller design for actuator preservation," in *Proceedings of the 17th IFAC World Congress*, 2008.

[119] C. Kravaris and R. A. Wright, "Deadtime compensation for nonlinear processes," *AIChE J.*, vol. 35, no. 9, pp. 1535–1542, 1989.

[120] F. N. Deniz, N. Tan, S. E. Hamamci, and I. Kaya, "Stability region analysis in smith predictor configurations using a pi controller," *Trans. Inst. Measurement Control*, vol. 37, no. 5, pp. 606–614, 2015.

[121] B. Komati, M. R. Pac, I. Ranatunga, C. Clévy, D. O. Popa, and P. Lutz, "Explicit force control vs impedance control for micromanipulation," in *ASME 2013 International Design Engineering Technical Conferences and Computers and Information in Engineering Conference*, American Society of Mechanical Engineers, 2013, V001T09A018–V001T09A018.

[122] R. Zhang, Q. Quan, and K.-Y. Cai, "Attitude control of a quadrotor aircraft subject to a class of time-varying disturbances," *IET Control Theory A*, vol. 5, no. 9, pp. 1140–1146, 2011.

[123] R. Madonski and P. Herman, "Method of sensor noise attenuation in high-gain observersexperimental verification on two laboratory systems," in *2012 IEEE International Symposium on Robotic and Sensors Environments (ROSE)*, IEEE, 2012, pp. 121–126.

[124] A. A. Prasov and H. K. Khalil, "A nonlinear high-gain observer for systems with measurement noise in a feedback control framework," *IEEE Trans. Automat. Contr.*, vol. 58, no. 3, pp. 569–580, 2013.

[125] B. Komati, C. Clevy, and P. Lutz, "Force tracking impedance control with unknown environment at the microscale," in *2014 IEEE International Conference on Robotics and Automation (ICRA)*, 2014, pp. 5203–5208.

[126] M. Boukhnifer and A. Ferreira, "Passive bilateral control of teleoperators under time delay and scaling factors," in *44th IEEE Conference on Decision and Control, and 2005 European Control Conference (CDC-ECC '05)*, 2005, pp. 6972–6977.

The connection between Chapter 2 and Chapter 3

In Chapter 2, existing robotic micromanipualtion techniques and associated force control strategies were reviewed. In the rest of this thesis, a novel force-controlled robotic micromanipulation system and will be developed for mechanical stimulation and calcium fluorescence imaging of *Drosophila* larvae. In Chapter 3, the entire micromanipulation system will be described, and a conventional proportional-integral-derivative (PID) controller will be implemented for regulating the touch force. The system is able to immobilize four larvae samples in an array. Two micromanipulators are coordinated to apply force-controlled mechanical stimuli to larva samples one after another. This system also features a fluorescence camera which allows for real-time imaging of larva samples.

CHAPTER 3
An Automated Force-Controlled Robotic Micromanipulation System for Mechanotransduction Studies of *Drosophila* Larvae

An Automated Force-Controlled Robotic Micromanipulation System for Mechanotransduction Studies of *Drosophila* Larvae

Weize Zhang, Alexandre Sobolevski, Bing Li, Yong Rao, and Xinyu Liu*

Department of Mechanical Engineering, McGill University, 817 Sherbrooke Street West, Montreal, Quebec H3A 0C3, Canada

*Corresponding author: (xinyu.liu@mcgill.ca)

IEEE Transactions on Automation Science and Engineering, vol. 13, no. 2, pp. 789C797, 2016. DOI 10.1109/TASE.2015.2403393.

The capability of accurately applying millinewtonlevel touch stimuli to *Drosophila* larvae and simultaneously observing their resultant fluorescence responses in mechanosensitive neuron transmission will enable novel studies of mechanotransduction neural circuitry. This paper presents an automated robotic micromanipulation system capable of force-controlled mechanical stimulation and quantitative fluorescence imaging of *Drosophila* larvae, which significantly improves the force regulation accuracy and operation consistency over conventional manual operations. An elastomeric microdevice is developed for efficient immobilization of an array of larvae for subsequent forcecontrolled touching. A microelectromechanical systems (MEMS) based force sensor is integrated into the robotic system for closedloop force control of larva touching at a resolution of 300 N. Two micromanipulators are coordinately servoed using orchestrated position and force control laws for automatic operations. The system performs simultaneous force-controlled larva touching and fluorescence imaging at a speed of four larvae per minute, with a success rate of 92.5%. This robotic system will greatly facilitate the dissection of mechanotransduction mechanisms of Drosophila larvae at both molecular and cellular levels.

Index Terms-Robotic micromanipulation, force control, calcium imaging, Drosophila larva, MEMS force sensor, neural circuitry, mechanotransduction.

3.1 Introduction

Robotic micromanipulation of biological samples (e.g., cells, tissues, and small organisms) has found important applications in biological and medical research. Significant efforts have been spent on developing robotic systems capable of performing specific biomanipulation tasks such as high-throughput cell injection [1, 2, 3, 4, 5, 6, 7], single-cell transportation [8, 9, 10], grasping [11, 12, 13, 14], cutting [15], orientation [16, 17, 18] and deposition [19, 20], cell/tissue mechanical characterization [21, 22, 23], and whole organism injection [24], to name just a few. These robotic systems operate in a highly consistent and efficient manner, and thus could significantly improve the reproducibility and throughput of the biomanipulation procedures and even enable new types of studies that cannot be fulfilled by conventional techniques.

Force sensing and control have played critical roles in robotic micromanipulation [25, 26]. Real-time measurement of interaction forces between a robotic end-effector and a biological sample provide an additional feedback of the ongoing manipulation, and could improve the dexterity and robustness of biomanipulation systems. For instance, the detection of indentation forces during cell injection can accurately predict the penetration of cell membrane and thus trigger the subsequent material deposition [27, 28, 3]. Closed-loop control of grasping force levels during robotic cell pick-place using a microelectromechanical systems (MEMS) microgripper guarantees secured grasping while avoiding cell damage by overlarge forces [11].

The capability of accurately regulating interaction forces during robotic micromanipulation may also prove useful for applying well-controlled mechanical stimulation to living cells or organisms and studying their mechanotransduction responses and pathways [29, 30, 31, 32]. Since most biomanipulation tasks are performed under optical microscopes, it is convenient to implement advanced optical imaging techniques on a micromanipulation system to probe the instantaneous mechanotransduction responses of bio-samples.

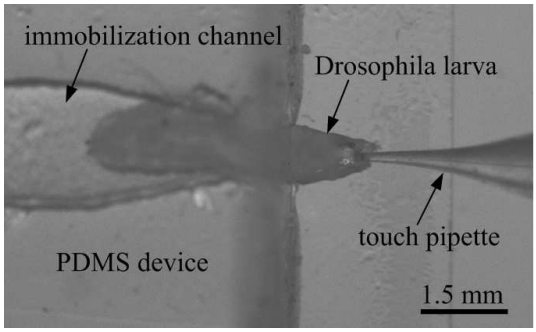

Figure 3–1: A bright-field snapshot of an immobilized *Drosophila* larva being touched by a glass pipette at the force level of 5 mN.

Drosophila is a popular model organism for studying sensory mechanotransduction and the underlying molecular and cellular mechanisms [33, 34]. A recent study demonstrated that millinewton-level touches at anterior segments of *Drosophila* larvae induced the larva's reorientation and selection of a new path for forward movement [35]. Follow-up genetic analysis and neural circuit breaking experiments revealed that a set of ∼50 interconnected neurons expressing the cell-surface protein *Turtle* (*Tutl*) are involved in the adjustment of moving direction. These exciting findings shed light on the unknown mechanisms controlling navigational behaviors in response to mechanical stimulation, and the further dissection of the *Tutl*-positive neural circuitry is needed.

Simultaneous mechanical stimulation of *Drosophila* larvae and fluorescent calcium imaging of transmissions in *Tutl*-positive neural circuits will enable the investigation of roles of individual *Tutl*-positive neurons in regulation of the touch-induced movement adjustments. To mimic the real scenario where an object hits the larva body, a simple one-dimensional touch applied with a fine hair was performed. However, the experimental setup previously employed [35] cannot carry out this type of experiments because it lacks an effective mechanism for immobilizing *Drosophila* larvae for fluorescence imaging. In addition, the gentle touch was applied manually using a fine hair, and inconsistent touch locations and less accurate touch force regulations led to variations in results obtained from different experiments and by different operators. A micromanipulation system capable of high-resolution touch force control and quantitative fluorescent imaging is highly desired. The system should be able to mimic the real object-hitting scenario by automatically

applying one-dimensional touches (mechanical stimuli), to perform in-situ fluorescence calcium imaging, and to guarantee a force range of 1-11 mN (a typical range adopted in manual operation) and a resolution better than 1 mN (the smallest force required to discern changes in larva's danger-escaping behavior).

This paper reports the development of the first automated robotic *Drosophila* larva manipulation system featuring closed-loop touch force control, microdevice-based larva immobilization, and *in-situ* fluorescence calcium imaging upon stimulation. A microfabricated elastomeric device is created to securely immobilize an array of larvae for subsequent force-controlled touching and fluorescence imaging, and a MEMS piezoresistive force sensor is integrated into the system for closed-loop force control at a resolution of 300 μN. An image processing algorithm is developed to identify the larva and touch pipette tip. Two micromanipulators are coordinately controlled based on microscopic vision feedback to apply quantitative mechanical stimulation to the immobilized larva (Fig. 3–1), and touch-induced calcium level changes in *Tutl*-positive neurons are accurately measured. Experimental results demonstrate that this micromanipulation system is capable of simultaneous mechanical stimulation and fluorescence imaging of *Drosophila* larvae in an accurate and consistent manner, which could enable a wide variety of mechanotransduction studies in *Drosophila*.

3.2 Robotic Micromanipulation System Setup

3.2.1 System Architecture

As shown in Fig. 3–2(A), the robotic system employs a stereo fluorescence microscope (SZX-16, Olympus), two three-degree-of-freedom (3-DOF) micromanipulators (MP-285, Sutter), a polydimethylsiloxane (PDMS) larva immobilization device carried by micromanipulator 1 (left), and an assembly of a glass pipette (tip size: 25 μm) and a MEMS piezoresiseive force sensor (AE801, Kronex) mounted on micromanipulator 2 (right). Each of the two micromanipulators moves along three orthogonal axes, with a motion range of 25 mm and a resolution of 40 nm. A fluorescence camera (EXi-Blue, QImaging) is mounted on the microscope for high-sensitivity fluorescence imaging. A host computer (Quad-Core 3.00GHz CPU and 6 GB memory), mounted with a motion-control

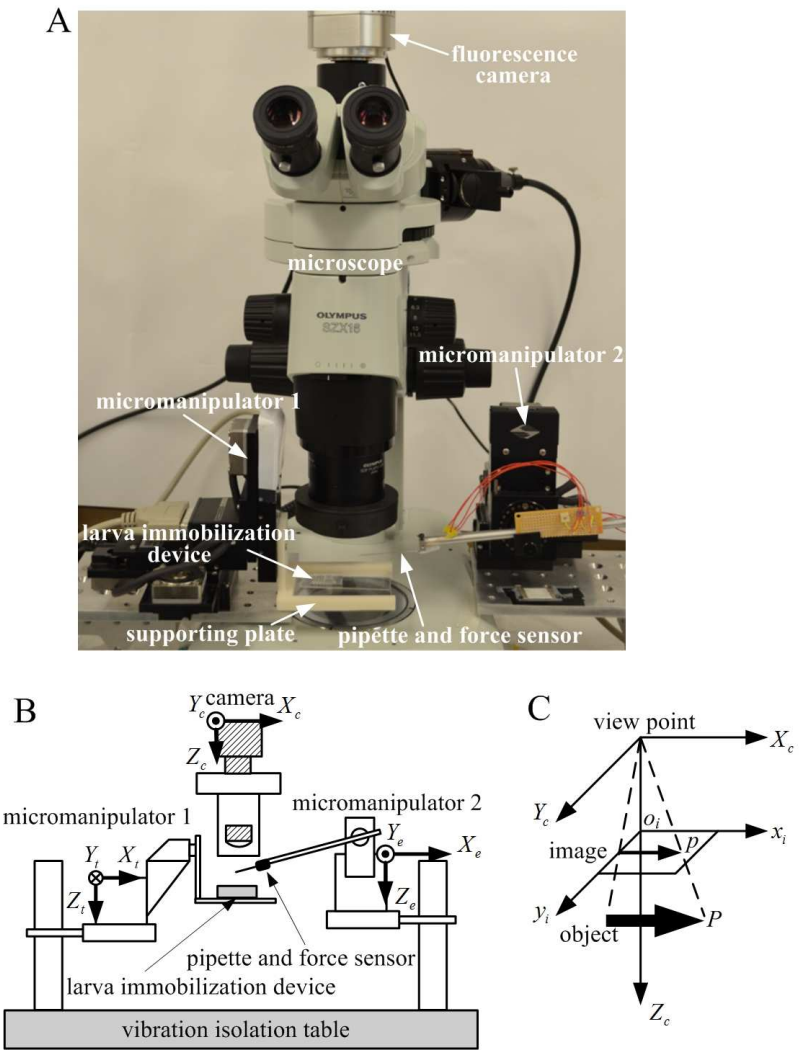

Figure 3–2: Robotic micromanipulation system setup. (A) System setup photo. (B) Coordinate frames associated with the robotic system. (C) Image projection model between the camera coordinate frame and the image plane.

card (PCIe-6259, National Instruments), is used to run algorithms of force data acquisition, imaging processing, and motion/force control. The control program is implemented in Visual C++. The sensor/pipette assembly is mounted with a tilting angle of 10°. The whole system is placed on an anti-vibration table to minimize vibrations.

Fig. 3–2(B) shows coordinate frames associated with the two micromanipulators (X_t-Y_t-Z_t and X_e-Y_e-Z_e) and the camera (X_c-Y_c-Z_c), and Fig. 3–2(C) illustrates the image projection model between the camera frame c and the image plane i. Denote the coordinate of a point P in frame c by ${}^cP = (x_c, y_c)$, and the coordinate of the correspondingly mapped point p in image frame i by ${}^ip = (u, v)$. The equation of scaled orthographic projection is:

$$\begin{bmatrix} s_x & 0 \\ 0 & s_y \end{bmatrix} \begin{bmatrix} u \\ v \end{bmatrix} = \begin{bmatrix} x_c \\ y_c \end{bmatrix} \tag{3.1}$$

where s_x and s_y are the pixel sizes along the horizontal and vertical directions of the image plane, which are calibrated off-line.

3.2.2 MEMS Piezoresistive Force Sensor

The MEMS piezoresistive force sensor (AE801, Kronex) was chosen for the following reasons. First, it is an off-the-shelf commercial sensor which could save our effort of device fabrication. Second, we need a measurement range of at least 0-11 mN and a resolution better than 1 mN as discussed in the introduction, both of which can be satisfied by the chosen model. Last but not least, the price of AE801 is affordable to allow for spare sensors in case of any damage. This sensor is fabricated from a 150 μm thick silicon cantilever with two doped piezoresistors located at its root (one on the top and one on the bottom). A Wheatstone bridge circuit is used to convert resistance changes of the piezoresistors into voltage signals. After attaching the glass pipette to the free end of the force sensor (Fig. 3–3(A)), the sensor/pipette assembly was calibrated using a precision balance (MXX-123, Denver Instrument; force resolution: 10 μN). The sensor/pipette assembly was controlled to contact a precision balance vertically (along Z_e in Fig. 3–3(C)), and readings of the balance (which represents the vertical component of the contact force F_o) and

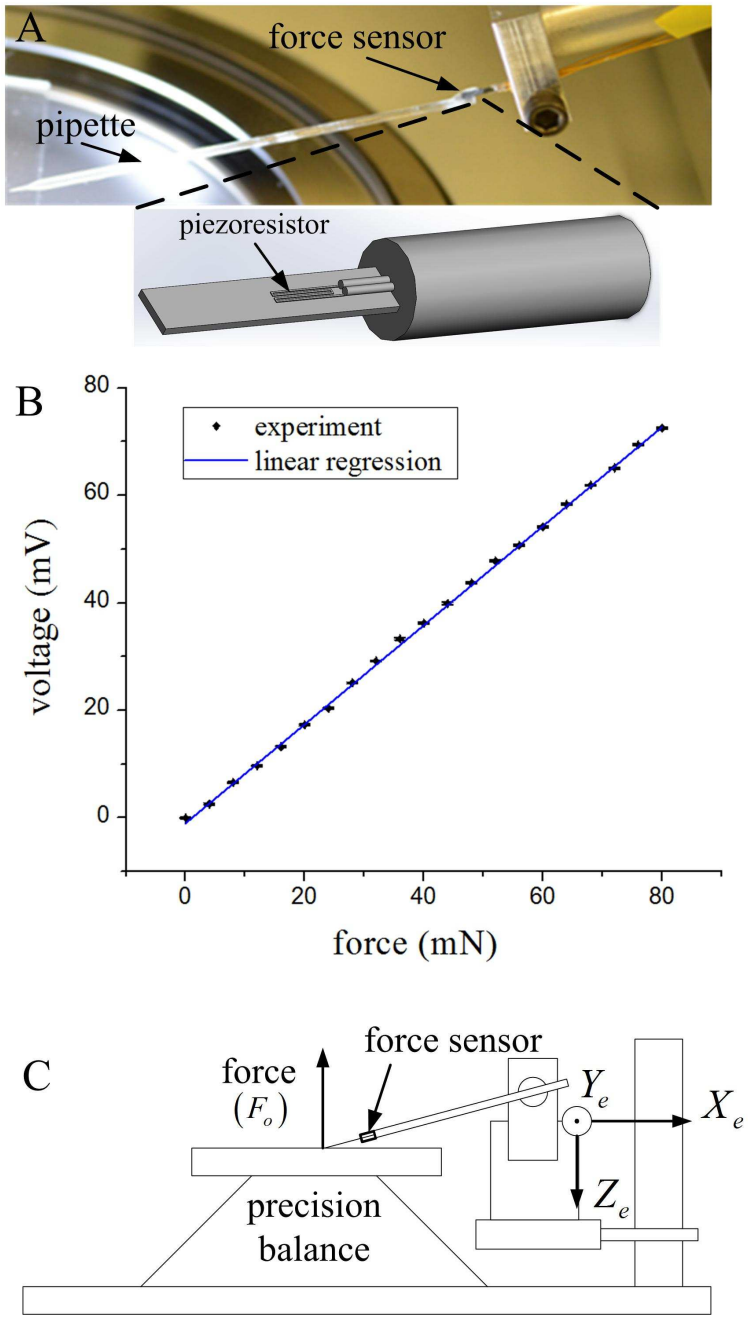

Figure 3–3: (A) Photograph of the piezoresistive force sensor with a glass pipette attached to the free end. (B) Calibration curve of the sensor/pipette assembly. (C) A schematic of calibration setup.

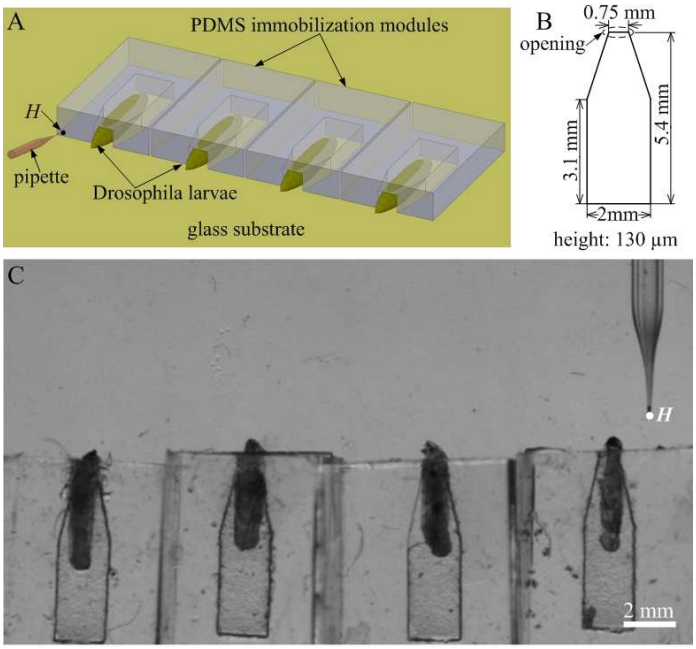

Figure 3–4: PDMS Larva immobilization device. (A) Schematic of the device with four separate immobilization modules. (B) Dimensions of the microchannel in each module. (C) Microscopic photo of four immobilized larvae in the device.

output voltages of the Wheatstone bridge circuit were recorded. The calibration data are shown in Fig. 3–3(B), which are average values of 5 measurements. The standard deviation of each data point is below 0.22 mV. The measurement range, resolution and sensitivity of the sensor/pipette assembly were determined to be 0-80 mN, 50 μN, and 0.93 mV/mN, respectively.

Only vertical component of the touch force is studied in this research, because previous studies have shown that the vertically-applied touch force to a larva has a positive correlation with it turning angle during the danger-escaping behaviour [35, 36]. The reason for using this piezoresistive force sensor is that it uses semiconductor as piezoresistive material, which results in high gauge factor and thus high sensitivity. Besides, this sensor also demonstrates high linearity throughout the measurement range.

3.2.3 Larva Immobilization Device

Fluorescence imaging of *Drosophila* larvae requires their body to be firmly immobilized. To observe *Tutl*-positive neurons inside the larva body, it is preferred to mechanically compress the

larva body to a smaller thickness so that the fluorescence light could pass the body tissues more efficiently. The conventional dissection approach [37] for immobilizing larvae is time-consuming and invasive, and the dissection procedure adds additional mechanical disturbance to the mechanotransduction studies.

Microfluidic devices have been recently applied to *Drosophila* larvae immobilization and fluorescence imaging [38, 39]. However, these devices fixed the larva in enclosed microfluidic chambers, and do not allow a pipette to reach the the anterior segment (nose) of larva body. In this research, a simple design was conceived and implemented for rapidly immobilizing single larvae with their noses exposed outside the device for mechanical stimulation. Fig. 3–4(A) shows the schematic of a PDMS device for larva immobilization. It includes four separated immobilization modules for fixing four third-instar larvae. Each module includes a microchannel fabricated using soft lithography, and the thickness of the microchannel was set to be 130 μm (Fig. 3–4(B)) so that the microchannel could firmly compress the body of a third-instar larva (0.8-1 mm thick) upon bonding with a glass substrate. Each microchannel has a 0.75 mm opening which is formed via manual cutting after soft lithography. The standard deviation of the opening size was $\pm$0.08 mm (n=4).

The fabrication of the PDMS device consists of three steps. First, a piece of 130 μm thick plastic film is cut to the desired shape of microchannels (Fig. 3–4(B)) with a laser cutter. The plastic film serves as the mold and is placed at the bottom of a petri dish. Uncured PDMS (w/w mixing ratio: 10:1) is then poured into the petri dish to reach a thickness of 3 mm. The peri dish is finally put into an oven and baked at 60 °C for 4 hours. The solidified PDMS is final peeled off to complete the fabrication process.

The larva immobilization process is performed manually, which is summarized as follows. A double-sided transparent tape is first attached to the glass substrate, and four larvae are then transferred to the tape using a pair of tweezers. The adhesive tape significantly reduces the larva locomotion and facilitates the subsequent immobilization. Individual PDMS module is manually aligned with a larva and placed onto the adhesive tape to fix the larva. The low height of the

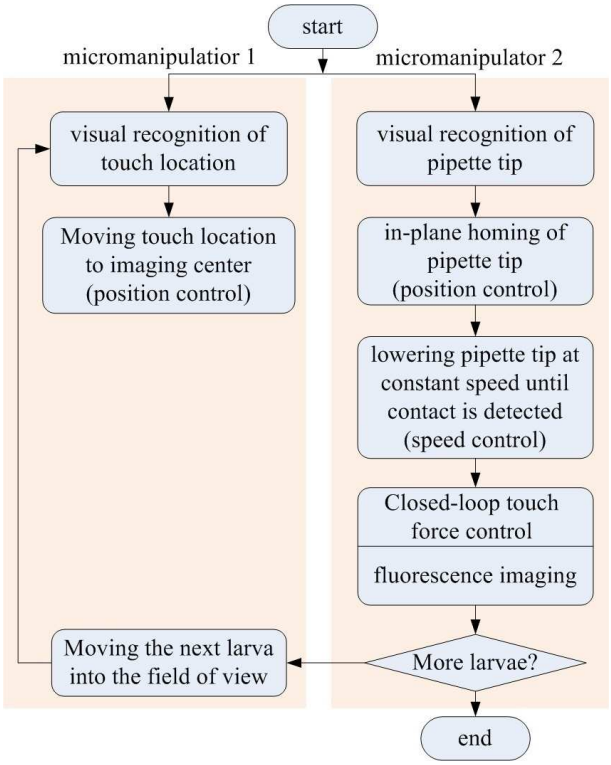

Figure 3–5: Overall control sequence of robotic operations.

microchamber presses and flattens the larva body. The adhesion between the tape and the PDMS module bottom surface is strong enough to securely immobilize the larva without further bonding treatments (e.g., oxygen plasma). The four modules are arranged on the substrate side by side to form an array of four fixed larvae with a spacing of 4.5±0.8 mm (n=4). This regular array greatly simplifies the robotic larva positioning task during operations. The PDMS device is reusable after washing and sterilization. Fig. 3–4(C) shows four immobilized larvae in the device with the touch needle suspended close to the first target larva. The whole larva immobilization process can be completed within two minutes.

3.3 Force-Controlled Larva Stimulation and Fluorescence Imaging

3.3.1 Overall Control Sequence

After immobilization, the PDMS device with the larva samples is placed onto the supporting plate of micromanipulator 1 (Fig. 3–2), with the first target larva in the field of view of the microscope. The pipette tip is also brought into the field of view, and its initial position is

manually adjusted as follows. The initial in-plane image coordinates (in frame i) of the pipette tip is set to close to but not overlapping with the larva nose, and the initial out-of-plane coordinate (along Z_e) of the pipette tip is set to make the pipette tip visible (not necessarily in focus) in the field of view and high enough to avoid collision with the target larva. The coordinates of this initial position in (X_e-Y_e-Z_e) serves as the home position H (Fig. 3–4(A)(C)) of the pipette tip during operations. Small variations in this manually-set home position do not affect the subsequent visual recognition of the pipette tip and robotic manipulation.

The control sequence, as shown in Fig. 3–5, starts from visual recognition of the image coordinates of the pipette tip and the touch location on the larva nose (described in Section 3.3.2). The larva nose is then brought to the center of the field of view. In the meanwhile, the pipette tip is moved in-plane (along X_e and Y_e) to the image coordinates of the touch location (a position right above the touch location on the larva nose), during which coordinate transformation from the image frame i to the micromanipulator 2 frame e is performed (see Section III-C). After that, the pipette tip is lowered vertically along Z_e at a constant speed of 500 μm/s (the maximum speed of the micromanipulator) toward the larva nose, and the voltage signal from the force sensor is monitored constantly to determine the initial contact between the pipette tip and the larva nose (described in Section 3.3.4). Upon the contact being detected, the control of micromanipulator 2 is switched from the position control mode to the force control mode (Fig. 3–7), and the touch force is regulated by a proportional-integral-derivative (PID) controller. Once the force-controlled larva stimulation is started, the camera is switched from bright-field imaging to fluorescence imaging for quantifying calcium levels in *Tutl*-positive neurons in the immobilized portion of the larva body. After the completion of the mechanical stimulation and fluorescence imaging, the pipette tip is lifted up, then moved backed to the *home* position, and meanwhile the next larva is brought into the field of view. This operation sequence is repeated until all the four larvae are touched and observed.

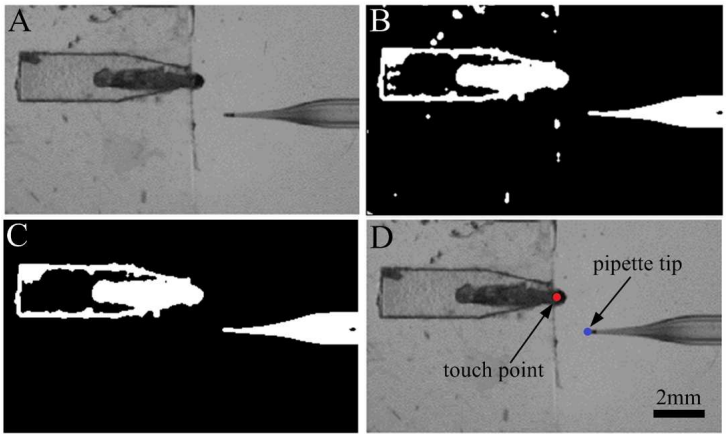

Figure 3–6: Image processing sequence of identifying the pipette tip and the touch location on the larva nose.

3.3.2 Visual Recognition of Pipette Tip and Touch Location

An image processing algorithm is developed to identify the pipette tip and the nose of target larva. An image, including an immobilized larva and the pipette, is read from the camera into the host computer in RGB format and converted into eight-bit grayscale format, as shown in Fig. 3–6(A). The resultant image is binarized into a black-white image (Fig. 3–6(B)) using Otsu's adaptive thresholding method [40]. Based on the connectivity of the white areas, the two biggest areas, corresponding to the larva (connected with the channel walls) and the pipette, are identified and removed from the image to create a 'background' image that just includes noise features. This 'background' image is subtracted from the original binary image to leave only the two biggest areas (Fig. 3–6(C)). In the current setup, the pipette area is always smaller than the larva connected with the channel walls. Thus, for the biggest area (larva and channel walls), the image coordinates of rightmost pixel are identified and regarded as the tip of the larva nose, and the touch location is set to be the point 400 μm away on the left of the larva nose (red point in Fig. 3–6(D)). In the second biggest area (pipette), the image coordinates of the leftmost pixel are found and saved as the pipette tip (blue point in Fig. 3–6(D)). The vertical coordinate (along X_e) of the pipette tip is not needed in operations since the force sensor is able to detect the initial contact while lowering the pipette. The imaging processing algorithm takes 15 ms on the host computer.

3.3.3 Control Architecture and Coordinate Transformations

As shown in Fig. 3–7, the robotic control system includes an image space task planner (for implementing the control sequence in Fig. 3–5), two PID closed-loop position controller for regulating the motions of the two micromanipulators, and one PID closed-loop force controller for adjusting the touch force applied to *Drosophila* larvae. Visual feedback is used to provide the two micromanipulators with image coordinates of the pipette tip (${}^{i}p_t$) and the touch location (${}^{i}p_l$) and guide the robotic manipulation, forming a vision-guided 'look-then-move' system.

During automatic operations, an image-based task planner receives real-time visual feedback of two image coordinates (${}^{i}p_t$ and ${}^{i}p_l$), plans the motions of two micromanipulators, and generates reference signals (p_1 and p_2) for the two PID position controllers. The motion regulation of micromanipulator 2 is transited from position control to force control once the initial touch is detected (the virtual switch K is thrown from state 1 to state 2).

Since the visual feedback is always expressed in the image frame i, the task planner needs to conduct coordinate transformations between: (i) image frame i and micromanipulator 1 frame t (transformation #1); and (ii) image frame i and micromanipulator 2 frame e (transformation #2).

Denote by ${}^{t}R_c \in \Re^{2\times 2}$ the rotation matrix of frame c with respect to (w.r.t.) frame t. Denote by ${}^{t}t_c \in \Re^{2}$ the origin location of the frame c w.r.t. the frame t. Transformations #1 and #2 can be expressed by

$$\begin{aligned} {}^{t}P &= {}^{t}R_c\,{}^{c}P + {}^{t}t_c \\ {}^{e}P &= {}^{e}R_c\,{}^{c}P + {}^{e}t_c \end{aligned} \tag{3.2}$$

Rewriting (3.1) as

$$S\,{}^{i}p = {}^{c}P \tag{3.3}$$

where

$$S = \begin{bmatrix} s_x & 0 \\ 0 & s_y \end{bmatrix}$$

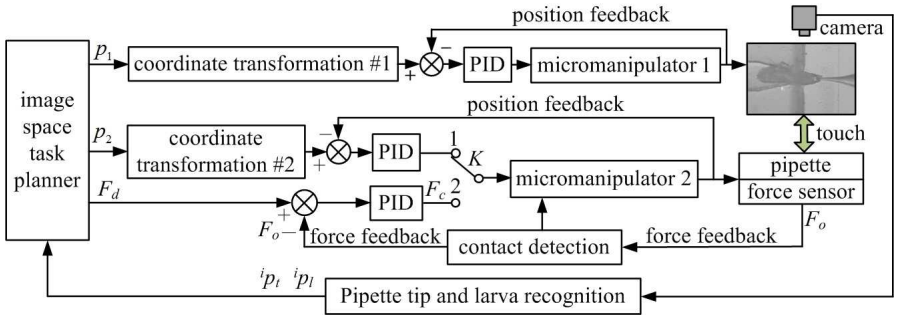

Figure 3–7: Schematic diagram of the system control architecture.

and substituting (3.3) into (3.2) yields

$$^tP = {}^tR_c S^i p + {}^tt_c \tag{3.4}$$

$$^eP = {}^eR_c S^i p + {}^et_c \tag{3.5}$$

As defined in Fig. 3–2, the coordinate frames t, e, and i have the following rotation matrices:

$$^tR_c = \begin{bmatrix} 1 & 0 \\ 0 & -1 \end{bmatrix}, \quad {}^eR_c = \begin{bmatrix} 1 & 0 \\ 0 & 1 \end{bmatrix} \tag{3.6}$$

The discussion above clarifies the relationship between the pixel coordinates and the coordinates used in micromanipulators, which is used in the space task planner for implementing the control sequence in Fig. 3–5.

3.3.4 Contact Detection and Force Control

Before the closed-loop control of touch forces, the initial contact between the pipette tip and the larva nose is detected by monitoring the feedback from the force sensor. The output signal of the force sensor were sampled at 500 Hz. The average changing rate of the force signal in the past 0.2 seconds was adopted as an indicator of initial contact, which is robust to zero drifts and noises of the force sensor data. For a speed of 100 μm/s at which the pipette was lowered, a threshold of 2.5 mN/s of the average changing rate of the force signal was used to trigger the transition from position control to force control (virtual switch K from position 1 to position 2 in Fig. 3–7). This threshold value was determined through trial-and-error experiments; it should be

high enough to prevent the control system from being triggered by noises in force measurement data before contact, and meanwhile low enough to quickly trigger the controller transition right after the initial contact. A smooth controller transition is desired, and effective methods have been proposed in recent years [41]. In this work, the smooth controller transition is achieved by maintaining the voltage control signal of the z-axis of the micromanipulator 2 at the same level during the transition. Before the transition (position control), micromanipulator 2 moves down at the maximum speed (500 μm) and the voltage control signal reaches its maximum. Once the transition is triggered (force control), the high gain of the three PID coefficients also results in a saturated voltage control signal. Thus, the z-axis velocity of micromanipulator 2 remains constant at the transition point.

The PID closed-loop force controller receives the instruction of desired touch force (F_d in Fig. 3–7) from the task planner, compares it with the force feedback (F_o in Fig. 3–7), and computes voltage signals as inputs for micromanipulator 2 based on the PID control law. The force controller can be expressed by

$$V_c = K_p e_f(t) + K_i \int e_f(t) + K_d \dot{e}_f(t) \tag{3.7}$$

where V_c denotes the voltage control signal for micromanipulator 2, and $e_f(t) = F_o(t) - F_d$. K_p, K_i, and K_d are the three gains of the PID controller. The derivative component acts as a dampening term which could improve the dynamic performance of the system [42]. To minimize the effect of measurement noises of the feedback signal on the derivative component, the term $\dot{e}_f$ was calculated using a noise-insensitive differentiator [43].

3.4 Experimental Results and Discussion

The larvae used in the experiments are transgenically encoded with green fluorescent proteins (GFP) in *Tutl*-positive neurons. Third-instar larvae were immobilized in the PDMS device, and the whole immobilization process took less than 2 minutes. A 3.2× objective (NA=0.15) was used for both bright-field and fluorescence imaging, and the horizontal and vertical pixel sizes were

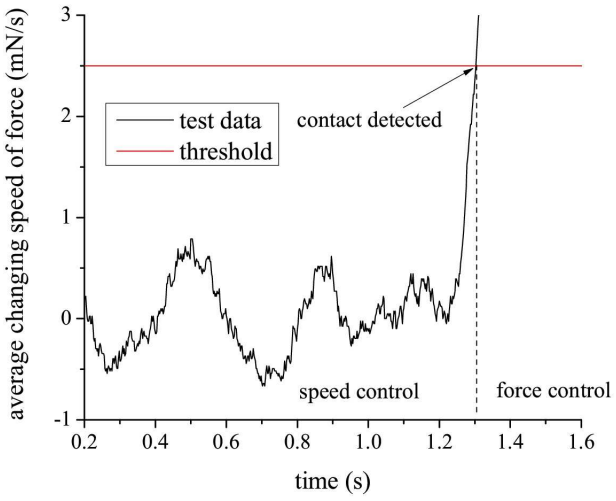

Figure 3–8: Experimental data of detecting the initial contact between the pipette tip and the larva nose before closed-loop force control. Contact is detected once average force changing rate of the past 0.2 seconds reaches the threshold.

calibrated to be $s_x = s_y = 0.5$ μm. The camera frame rates for bright-field and fluorescence imaging are 25 Hz and 2.5 Hz (fluorescence exposure time: 400 ms), respectively.

3.4.1 Closed-Loop Force Control

As described in Section 3.3.4, the average changing speed of the force feedback over the past 0.2 s (100 consecutive data points) was used as an indicator to detect the initial contact between the pipette tip and the larva nose. Fig. 3–8 shows the experimental results of the average force changing speed as a function of time. A threshold of 2.5 mN/s (red line) indicates the transition point for the micromanipulator 2 from position control to force control.

Four parameters of the PID force controller were optimized through extensive trail-and-error experiments. Besides the three PID gains (K_p, K_i, K_d), the limit of the voltage control input for the z-axis motor of micromanipulator 2, $V_{\max}$, was also considered. The inequalities $|V_c| \leq V_{\max}$ was implemented in the controller to limit the maximum speed and to protect the fragile MEMS force sensor.

Based on the results from a previous study [35], the touch force for larva stimulation was controlled in the range of 1-11 mN. Fig. 3–9(A) shows the experimental results of the step response

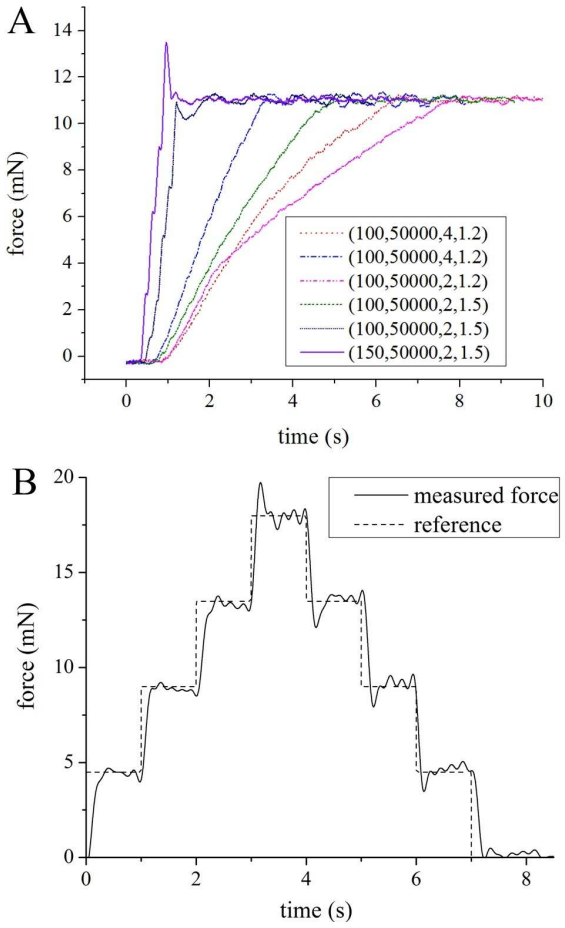

Figure 3–9: Experimental results of touch force control. (A) Step responses of the PID force controller with different combinations of controller parameters (K_p, K_i, K_d, $V_{\max}$). (B) Tracking response of a multi-step force.

curves of the PID controller at different combinations of the four parameters. The combination of $K_p = 150$, $K_i = 50000$, $K_d = 2$, and $V_{\max} = 1.5$ was chosen for the subsequent larva touch experiments since it yielded the fastest dynamic response with a short rise time of 612 ms and an acceptable overshoot of 20%. Fig. 3–9(B) shows the tracking response of a multi-step force using the five controller parameters selected above.

3.4.2 Larva Stimulation and Fluorescence Imaging

After the force controller was optimized, larva stimulation and fluorescence imaging experiments were performed. The two micromanipulators moved the larva samples and the pipette at a speed of 500 μm/s during closed-loop position control, and the touch force was accurately controlled to be 5 mN (which matches the typical order of touch force magnitude used in a previous study[35] where manual operation was involved to mimic the object-hitting scenario). The whole manipulation process of a single larva (from positioning the larva into the field of view to completion of touching and imaging) took 15 s, yielding a speed of 4 larvae/minutes. In comparison, a proficient human operator typically has a speed of 1 larva per 5 minutes. The operation speed of the robotic system can be further improved by adopting micromanipulators with a faster speed. 40 samples (10 arrays) have been tested, out of which 37 samples were successfully touched and imaged, with a success rate of 92.5%. The operation of a larva is judged to be successful if the whole larva touching and imaging process is conducted automatically without any failure. The most critical parts are the recognition of touch point, the force control and the acquisition of fluorescent imaging data. The reason of failure was that, in rare cases, the head of a larva was curved in the image plane, but the image processing algorithm assumed that the larva's spine is horizontally straight. This caused the pipette tip to miss the ideal touch location and thus invalidated the fluorescence imaging data. This failure mode can be avoid by changing the imaging processing algorithm to extract the larva spine and determine the touch location along it.

Figs. 3–10(A)(B) show the fluorescent photos taken before and after a 5 mN touch. The glowing spots in the larva body are the GFP-expressing *Tutl*-positive neurons. We quantified fluorescence intensity values of three groups of *Tutl*-positive neurons (the ones in areas 1-3). Areas

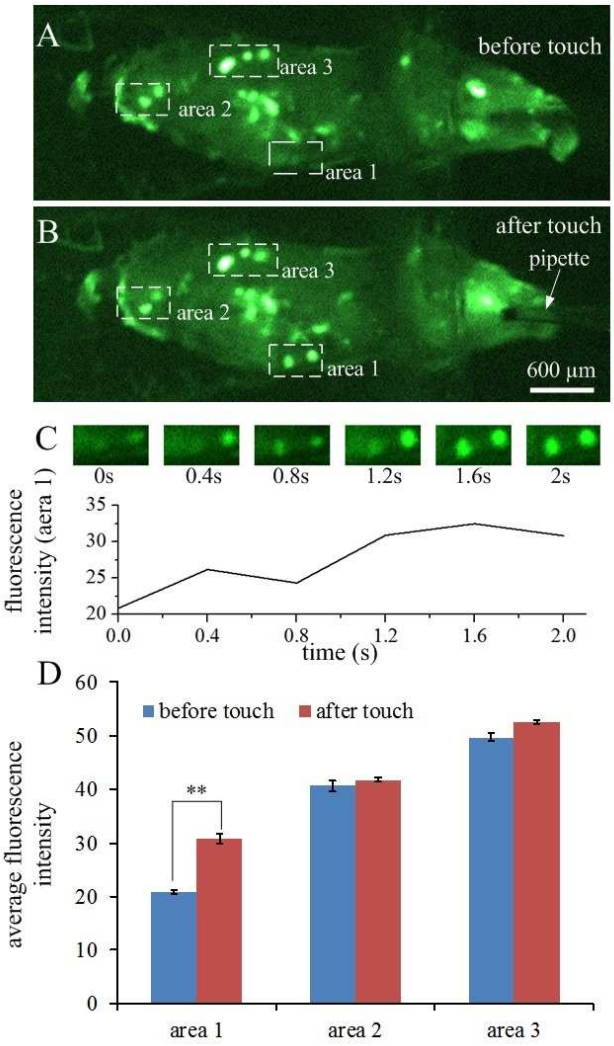

Figure 3–10: Fluorescence imaging results measured before and after robotic touching at the level of 5 mN. (A)(B) Fluorescent images of a *Drosophila* larva taken (A) before and (B) after the 5 mN touch. The average fluorescence intensity values of areas 1-3 that included *Tutl*-positive neurons were quantified off line. (C) Consecutive image frames and fluorescence intensity values showing dynamic change in the calcium signal of area 1 upon touching. (D) Quantitative data of the average fluorescence intensity values of area 1-3 measured from five consecutive image frames before and after touching (n=5). $^*p < 0.05$ as compared to the intensity values measured before touching.

1-3 were chosen as they include neuron groups with typically observable fluorescence expressions. Note that the quantification of calcium fluorescence signals in Fig. 3–10 is preliminary and just for proof-of-concept demonstrations. Further biological experiments are underway to obtain more biologically meaningful data. Figs. 3–10(C) shows the dynamic changes in florescence intensity in area 1 in six consecutive frames (exposure time: 400 ms) upon touching (photograph at t = 0 was taken right after touching). One can observe that, once the force is applied, the fluorescent intensity in area 1 starts to change and stabilizes after 2 sec. Fig. 3–10(D) shows the average fluorescence intensity values of the three areas which were calculated based on the fluorescence intensity values of area 1 in five consecutive image frames (n=5) of the same larva right after touch.

The robotic system has several advantages over the conventional manual operation, including the high force control accuracy, the unique capability of simultaneous larva touching and calcium fluorescence imaging, and the elimination of human-induced errors. The force controller has a resolution of 300 μN and a rising time of 612 ms, which cannot be achieved by manual operation. By integrating a larva immobilization device, the robotic system is capable of applying well-controlled mechanical stimulation and, at the same time, imaging neural signal transmissions via fluorescence calcium imaging. In contrast, a human operator has to dissect the larva body for performing fluorescent imaging [35], which is a tedious and more invasive process. The robotic system manipulates an array of *Drosophila* larvae in an automated fashion, and not human involvement is required during the touching/imaging process. This avoids potential uncertainties of data acquisition caused by manual operations.

3.5 Conclusion

An automated robotic micromanipulation system with force-control capability was developed for mechanotransduction studies of *Drosophila* larvae. Using a PDMS immobilization device, *Drosophila* larvae were securely immobilized into an array for robotic manipulation. An image processing algorithm was developed for recognizing the pipette tip and the touch location on the larva, providing vision feedback for closed-loop position control. A MEMS force sensor, mounted

with a glass pipette, was controlled to touch a larva, during which the touch force was regulated using a closed-loop controller. The force controller was optimized to provide good dynamic response and reliable force-regulated touching. The fluorescence imagining results proved the feasibility of using the system for studying transmission responses of *Tutl*-positive neurons to mechanical stimuli.

This chapter investigates using a simple PID controller without precisely modeling the system. The performance of force control still has room to improve. We will tackle this problem in the next chapter.

References

[1] W. Wang, X. Y. Liu, D. Gelinas, B. Ciruna, and Y. Sun, "A fully automated robotic system for microinjection of zebrafish embryos," *PLoS ONE*, vol. 2, no. 9, e862, 2007.

[2] W. H. Wang, X. Y. Liu, and Y. Sun, "High-throughput automated injection of individual biological cells," *IEEE Trans. Autom. Sci. Eng.*, vol. 6, no. 2, pp. 209–219, 2009.

[3] H. B. Huang, D. Sun, J. K. Mills, and S. H. Cheng, "Robotic cell injection system with position and force control: toward automatic batch biomanipulation," *IEEE Trans. Robot.*, vol. 25, no. 3, pp. 727–737, 2009.

[4] Y. Xie, D. Sun, C. Liu, H. Tse, and S. Cheng, "A force control approach to a robot-assisted cell microinjection system," *Int. J. Robot. Res.*, vol. 29, no. 9, pp. 1222–1232, 2010.

[5] X. Liu, R. Fernandes, M. Gertsenstein, A. Perumalsamy, I. Lai, M. Chi, K. H. Moley, E. Greenblatt, I. Jurisica, R. F. Casper, et al., "Automated microinjection of recombinant bcl-x into mouse zygotes enhances embryo development," *PLoS ONE*, vol. 6, no. 7, e21687, 2011.

[6] H. P. Spaink, C. Cui, M. I. Wiweger, H. J. Jansen, W. J. Veneman, R. Marín-Juez, J. de Sonneville, A. Ordas, V. Torraca, W. van der Ent, et al., "Robotic injection of zebrafish embryos for high-throughput screening in disease models," *Methods*, vol. 62, no. 3, pp. 246–254, 2013.

[7] J. Liu, V. Siragam, Z. Gong, J. Chen, M Fridman, C. Leung, Z. Lu, C. Ru, S. Xie, J. Luo, et al., "Robotic adherent cell injection (raci) for characterizing cell-cell communication," *IEEE Trans. Biomed. Eng.*, vol. PP, no. 99, pp. 1–1, 2014.

[8] S. Hu and D. Sun, "Automatic transportation of biological cells with a robot-tweezer manipulation system," *Int. J. Robot. Res.*, vol. 30, no. 14, pp. 1681–1694, 2011.

[9] C. C. Cheah, X. Li, X. Yan, and D. Sun, "Observer-based optical manipulation of biological cells with robotic tweezers," *IEEE Trans. Robot.*, vol. 30, no. 1, pp. 68–80, 2013.

[10] A. Thakur, S. Chowdhury, P. Švec, C. Wang, W. Losert, and S. K. Gupta, "Indirect pushing based automated micromanipulation of biological cells using optical tweezers," *Int. J. Robot. Res.*, vol. 33, pp. 1098–1111, 2014.

[11] K. Kim, X. Liu, Y. Zhang, and Y. Sun, "Nanonewton force-controlled manipulation of biological cells using a monolithic mems microgripper with two-axis force feedback," *J. Micromech. Microeng.*, vol. 18, no. 5, p. 055 013, 2008.

[12] T. Tanikawa and T. Arai, "Development of a micro-manipulation system having a two-fingered micro-hand," *IEEE Trans. Robot. Autom.*, vol. 15, no. 1, pp. 152–162, 1999.

[13] M. Jeannerod, M. A. Arbib, G. Rizzolatti, and H Sakata, "Grasping objects: the cortical mechanisms of visuomotor transformation," *Trends Neurosci.*, vol. 18, no. 7, pp. 314–320, 1995.

[14] S. Chowdhury, A. Thakur, C. Wang, P. Svec, W. Losert, and S. K. Gupta, "Automated indirect transport of biological cells with optical tweezers using planar gripper formations," in *2012 IEEE International Conference on Automation Science and Engineering (CASE)*, IEEE, 2012, pp. 267–272.

[15] N. Inomata, T. Mizunuma, Y. Yamanishi, and F. Arai, "Omnidirectional actuation of magnetically driven microtool for cutting of oocyte in a chip," *J. Microelectromech. Syst.*, vol. 20, no. 2, pp. 383–388, 2011.

[16] X. Liu, Z. Lu, and Y. Sun, "Orientation control of biological cells under inverted microscopy," *IEEE/ASME Tran. Mechatron.*, vol. 16, no. 5, pp. 918–924, 2011.

[17] C. Leung, Z. Lu, X. P. Zhang, and Y. Sun, "Three-dimensional rotation of mouse embryos," *IEEE Trans. Biomed. Eng.*, vol. 59, no. 4, pp. 1049–1056, 2012.

[18] Q. Zhao, M. Sun, M. Cui, J. Yu, Y. Qin, and X. Zhao, "Robotic cell rotation based on the minimum rotation force," *IEEE Trans. Autom. Sci. Eng.*, vol. PP, no. 99, pp. 1–12, 2014, ISSN: 1545-5955. DOI: 10.1109/TASE.2014.2360220.

[19] Z. Lu, C. Moraes, G. Ye, C. A. Simmons, and Y. Sun, "Single cell deposition and patterning with a robotic system," *PLoS ONE*, vol. 5, no. 10, e13542, 2010.

[20] Y. H. Anis, M. R. Holl, and D. R. Meldrum, "Automated selection and placement of single cells using vision-based feedback control," *IEEE Trans. Autom. Sci. Eng.*, vol. 7, no. 3, pp. 598–606, 2010.

[21] P Jordan, S Socrate, T. Zickler, and R. Howe, "Constitutive modeling of porcine liver in indentation using 3d ultrasound imaging," *J. Mech. Behav. Biomed.*, vol. 2, no. 2, pp. 192–201, 2009.

[22] X. Liu, J. Shi, Z. Zong, K.-T. Wan, and Y. Sun, "Elastic and viscoelastic characterization of mouse oocytes using micropipette indentation," *Ann. Biomed. Eng.*, vol. 40, no. 10, pp. 2122–2130, 2012.

[23] H. Xie, M. Yin, W. Rong, and L. Sun, "In situ quantification of living cell adhesion forces: single cell force spectroscopy with a nanotweezer," *Langmuir*, vol. 30, no. 10, pp. 2952–2959, 2014.

[24] M. Nakajima, T. Hirano, M. Kojima, N. Hisamoto, N. Nakanishi, H. Tajima, M. Homma, and T. Fukuda, "Local nano-injection of fluorescent nano-beads inside c. elegans based on nanomanipulation," in *2012 IEEE/RSJ International Conference on Intelligent Robots and Systems (IROS)*, IEEE, 2012, pp. 3241–3246.

[25] Z. Lu, P. C. Chen, and W. Lin, "Force sensing and control in micromanipulation," *IEEE Trans. Syst., Man, Cybern. C, Appl. Rev.*, vol. 36, no. 6, pp. 713–724, 2006.

[26] X. Y. Liu, K. Kim, Y. Zhang, and Y. Sun, "Nanonewton force sensing and control in microrobotic cell manipulation," *Int. J. Robot. Res.*, vol. 28, no. 8, pp. 1065–1076, 2009.

[27] Z. Lu, P. C. Y. Chen, J. Nam, R. Ge, and W. Lin, "A micromanipulation system with dynamic force-feedback for automatic batch microinjection," *J. Micromech. Microeng.*, vol. 17, no. 2, pp. 314–321, 2007.

[28] X. Liu, Y. Sun, W. Wang, and B. M. Lansdorp, "Vision-based cellular force measurement using an elastic microfabricated device," *J. Micromech. Microeng.*, vol. 17, no. 7, p. 1281, 2007.

[29] M. Girot, M. Boukallel, and S. Régnier, "A microforce and nanoforce biomicroscope device for in vitro mechanotransduction investigation," *IEEE Trans. Instrum. Meas.*, vol. 57, no. 11, p. 2532, 2008.

[30] J. H. Nam, P. C. Y. Chen, Z. Lu, H. Luo, R. Ge, and W. Lin, "Force control for mechanoinduction of impedance variation in cellular organisms," *J. Micromech. Microeng.*, vol. 20, no. 2, p. 025 003, 2010.

[31] M. L. Han, Y. L. Zhang, M. Y. Yu, C. Y. Shee, and W. T. Ang, "Non-contact force sensing for real-time stressing of biological cells," *Micro Nano Lett.*, vol. 6, no. 5, pp. 306–310, 2011.

[32] H. Ladjal, J.-L. Hanus, A. Pillarisetti, C. Keefer, A. Ferreira, and J. P. Desai, "Reality-based real-time cell indentation simulator," *IEEE/ASME Trans. Mechatron.*, vol. 17, no. 2, pp. 239–259, 2012. DOI: 10.1109/TMECH.2010.2091010.

[33] G. G. Ernstrom and M. Chalfie, "Genetics of sensory mechanotransduction," *Annu. Rev. Genet.*, vol. 36, no. 1, pp. 411–453, 2002.

[34] A. P. Jarman, "Studies of mechanosensation using the fly," *Hum. Mol. Gen.*, vol. 11, no. 10, pp. 1215–1218, 2002.

[35] Y. Zhou, S. Cameron, W.-T. Chang, Y. Rao, et al., "Control of directional change after mechanical stimulation in drosophila," *Mol. Brain*, vol. 5, no. 1, pp. 39–51, 2012.

[36] R. Y. Hwang, L. Zhong, Y. Xu, T. Johnson, F. Zhang, K. Deisseroth, and W. D. Tracey, "Nociceptive neurons protect drosophila larvae from parasitoid wasps," *Curr. Biol.*, vol. 17, no. 24, pp. 2105–2116, 2007.

[37] A. D. Pilling, D. Horiuchi, C. M. Lively, and W. M. Saxton, "Kinesin-1 and dynein are the primary motors for fast transport of mitochondria in drosophila motor axons," *Mole. Biol. Cell*, vol. 17, no. 4, pp. 2057–2068, 2006.

[38] M. Ghannad-Rezaie, X. Wang, B. Mishra, C. Collins, and N. Chronis, "Microfluidic chips for in vivo imaging of cellular responses to neural injury in drosophila larvae," *PLoS ONE*, vol. 7, no. 1, e29869, 2012.

[39] S. Mondal, S. Ahlawat, K. Rau, V Venkataraman, and S. P. Koushika, "Imaging in vivo neuronal transport in genetic model organisms using microfluidic devices," *Traffic*, vol. 12, no. 4, pp. 372–385, 2011.

[40] N. Otsu, "A threshold selection method from gray-level histograms," *IEEE Trans. Syst., Man, Cybern.*, vol. 9, no. 1, pp. 62–66, 1979.

[41] Q. Xu, "Design and smooth position and force switching control of a miniature gripper for automatic microhandling," *IEEE Trans. Ind. Informat.*, vol. 10, no. 2, pp. 1023–1032, 2014.

[42] A Eisinberg, A Menciassi, S Micera, D Campolo, M. Carrozza, and P Dario, "Pi force control of a microgripper for assembling biomedical microdevices," *IEE P-Circ. Dev. Syst.*, vol. 148, no. 6, pp. 348–352, 2001.

[43] X. Wang and H. Lin, "Design and frequency analysis of continuous finite-time-convergent differentiator," *Aerosp. Sci. Technol.*, vol. 18, no. 1, pp. 69–78, 2012.

The connection between Chapter 3 and Chapter 4

The system reported in Chapter 3 features a conventional PID controller, whose performance was experimentally characterized. However, to mimic a sudden touch a *Drosophila* larva experiences in biological experiments, rapid dynamic response of the force control system is desired. The current dynamics of the PID controller cannot meet this requirement. To this end, Chapter 4 will present a switched fuzzy-PD controller for implementation on the developed micromanipulation system, which provides significantly improved dynamic performance. Two major factors that hinder the controller performance are modeling errors and force measurement noise. A noise-insensitive extended high gain observer (EHGO) is proposed to estimate the modeling errors and handle the noisy force feedback signal. The switched fuzzy-PD controller combines the fast convergence property of a fuzzy controller and the small steady-state oscillation of a PD controller. Compared to the PID controller, the settling time and overshoot of the switched fuzzy-PD controller are significantly reduced.

CHAPTER 4
Switched Fuzzy-PD Control of Contact Forces in Robotic Micro-Biomanipulation

Switched Fuzzy-PD Control of Contact Forces in Robotic Micro-Biomanipulation

Weize Zhang, Xianke Dong, and Xinyu Liu*

Department of Mechanical Engineering, McGill University, 817 Sherbrooke Street West, Montreal, Quebec H3A 0C3, Canada

*Corresponding author: (xinyu.liu@mcgill.ca)

IEEE Transactions on Biomedical Engineering, accepted.

Force sensing and control are of paramount importance in robotic micromanipulation. A contact force regulator capable of accurately applying mechanical stimuli to a live Drosophila larva could greatly facilitate mechanobiology research on *Drosophila* and may eventually lead to novel discoveries in mechanotransduction mechanisms of neuronal circuitries. In this paper, we present a novel contact force control scheme implemented in an automated *Drosophila* larvae micromanipulation system, featuring a switched fuzzy-PD controller and a noiseinsensitive extended high gain observer (EHGO). The switched fuzzy-PD control law inherits the fast convergence of fuzzy control and overcomes its drawbacks such as large overshoot and steady-state oscillation. The noise-insensitive EHGO can reliably estimate system modeling errors, and is robust to force measurement noises, which is advantageous over conventional high gain observers (sensitive to signal noises). Force control experiments show that, compared to a PID controller, this new force control scheme significantly enhances the system dynamic performance in terms of rising time, overshoot, and oscillation. The developed robotic system and the force control scheme will be applied to mechanical stimulation and fluorescence imaging of *Drosophila* larvae for identifying new mechanotransduction mechanisms.

Index Terms-robotic micromanipulation, force control, switched fuzzy-PD control, extended high gain observer, fluorescence imaging, Drosophila larva, mechanotransduction, neural basis of behavior.

4.1 Introduction

Force sensing and control have played critical roles in robotic micromanipulation [1, 2, 3, 4, 5]. Force-controlled robotic systems are capable of performing micromanipulation tasks with high dexterity [1], and can also facilitate mechanobiology studies in which accurately-regulated force stimulation needs to be applied to cells or small organisms for probing possible mechanotransduction pathways [6]. For instance, a recent study illustrates that *Drosophila* larva, an excellent model organism for neuroscience, orients and reselects its path of forward movement upon the application of millinewton-level touch forces to its head [7]. Further study of neural circuitries responsible for this touch-induced behavior could decipher the neural basis of these danger-escaping behaviors.

Targeting this interesting problem, we have developed a force-controlled robotic system (Fig. 4–1) for mechanical stimulation of *Drosophila* larvae and *in-situ* fluorescence imaging of the touch-induced neural signal transduction [8]. We have demonstrated that, compared to manual operation, this robotic system significantly improves the manipulation accuracy, consistency, throughput, and success rate. The system initially employed a conventional proportional-integral-differential (PID) force controller with a rising time of 0.612 s (sampling frequency: 500 Hz). Because the mechanical stimulation is typically applied to a larva in a stepwise fashion to mimic sudden touches a larva may experience during forward locomotion [7, 9], it is highly desired for the force controller to have rising time as short as possible. The objective of this work is to develop an advanced force control scheme to further improve the dynamic response of the contact force regulation during robotic manipulation of *Drosophila* larvae.

A number of force control strategies have been proposed for robotic micromanipulation. The most straightforward and widely used approach is PID control [10], or PI control [1] when the time derivative is hard to acquire due to measurement noise. PID control works satisfactorily for linear systems, but usually yields poor dynamic response when the system includes nonlinear components and undetermined parameters. To address this issue, system linearization methods were implemented for control of cell injection forces [11]. This type of approaches require the system terms to be determined. Impendence control is another approach used in micromanipulation,

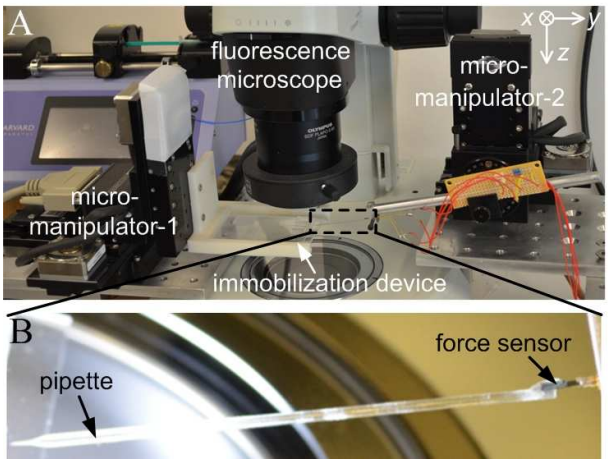

Figure 4–1: (A) Robotic system setup. (B) A glass pipette attached to a silicon piezoresistive force sensor for touching *Drosophila* larvae.

but it also requires precise dynamic models for feedforward [12]. An advanced control scheme, gain scheduling, was investigated in [13] to adaptively compensate for system nonlinearity, but modeling errors were neglected in this study. Scheduling technique designed for fault tolerance was investigated in [14], but it requires a partially known jump rate of fault. Switched Fuzzy-PID controller with feed forward compensation was investigated in [15], which does not require a known jump rate or mathematical model of model uncertainties, and thus represents a possible solution. However in this study, only simulations were conducted and no real experiments were demonstrated.

One common method to compensate for unknown system parameters and modeling errors is to implement an extended high gain observer (EHGO) [16]. Conventional EGHOs are difficult to use for force control in robotic micromanipulation, because small force signals are always noisy whereas conventional EHGOs are very sensitive to noise in feedback [17, 18]. To improve the system dynamics, fuzzy logic controllers have been illustrated to have excellent transient state of step response [19, 20] and thus could reduce the rising time of the force control system. A fuzzy controller is composed of a set of IF-THEN rules summarized from human experience, and thus has higher robustness than traditional PID controllers. In spite of these merits, fuzzy control often

leads to oscillation of the system response in the steady state, because of its sensibility to the feedback when operating around the equilibrium point.

In this article, we propose a novel control scheme integrating a switched fuzzy-PD controller and a noise-insensitive EHGO, and apply it to force-controlled robotic manipulation of *Drosophila* larvae. The major contribution of this work lies in the development of the force control scheme which is applicable to a variety of robotic micromanipulation tasks requiring high-performance force control. The control scheme utilizes the fast convergence of fuzzy control for nonlinear systems and overcomes its steady-state oscillations by switching fuzzy control to PD control as the contact force approaches the steady state (which is called switched fuzzy-PD control). The control scheme also integrates a revised noise-insensitive EHGO to compensate for the undetermined system terms. Although the conventional EHGOs have been combined with fuzzy controllers [21, 22], the control scheme we propose here integrates, for the first time, a noise-insensitive EHGO with the switched fuzzy-PD control for system parameter estimation/compensation. By adding the first and second derivative of force to the extended state vector and saturating the derivative of the estimated error, the proposed EHGO guarantees fast convergence and reduced peaking phenomenon despite measurement noise. This EHGO could be easily modified to work for other observable single output system with measurement noise, and the parameter tuning technique is shown in detail. In comparison, the proposed observer-controller scheme has shorter rising time, less overshoot and oscillation than PID control.

4.2 System Setup and Operation Procedure

The robotic micromanipulation system has been reported previously [8], and the focus of this paper is to design and implement a novel control scheme to regulate the contact forces during robotic manipulation of *Drosophila* larvae. To make this article self-contained, we briefly introduce the system setup and the automated manipulation procedure. As shown in Fig. 4–1(A), the robotic system employs a fluorescence microscope (SZX-16, Olympus), two three-degree-of-freedom (3-DOF) micromanipulators (MP-285, Sutter), a custom-made larva immobilization device, and a glass pipette mounted on a micro-electro-mechanical systems (MEMS) piezoresistive force sensor

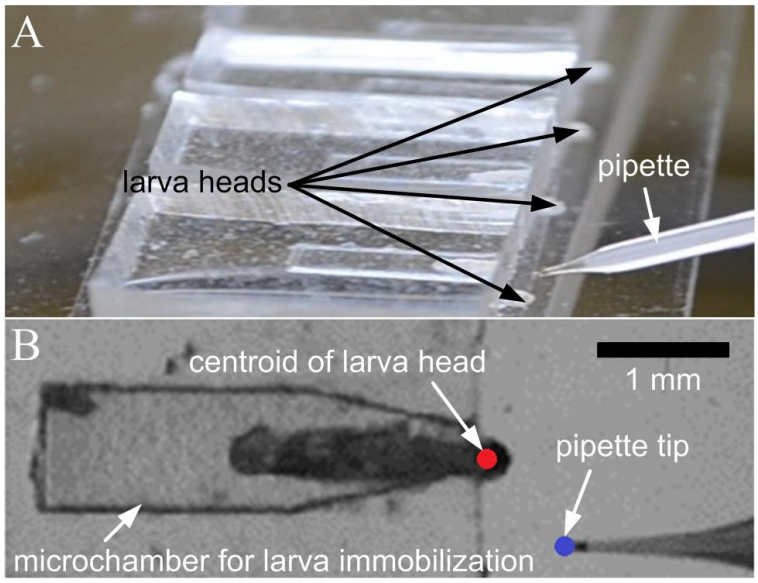

Figure 4–2: (A) Larva immobilization device with 4 larvae immobilized. (B) The pipette tip and the target touch location on larva head are identified using an imaging processing algorithm.

(AE801, Kronex; Fig. 4–1(B)). Micromanipulator-1 moves different larvae under the microscope, and micromanipulator-2 controls the pipette tip for larva touching. The force measurement range, resolution, and sensitivity of the pipette/sensor assembly are 0-120 mN, 50 μN, and 0.67 mV/mN, respectively. The force feedback data were sampled at 500 Hz, because the corresponding sampling interval (0.002 s at 200 Hz) needs to be significantly shorter than the characteristic time of the system, which will be measured in Section 4.6.3.

Before the system starts the automated larva manipulation, four larvae are immobilized in a row using the immobilization device (Fig. 4–2(A); see details in [8]). The system then visually recognizes the pipette tip and the centroid of the first larva head (target location for touching) outside the immobilization device (Fig. 4–2(B)). After that, the pipette tip is moved in-plane to the image coordinate of the larva head centroid, and then downward towards the larva head (along z-axis in Fig. 4–3(A)) until a contact is detected from the force feedback. Upon contact being detected, the microscopy is automatically switched from bright field to fluorescence and the control law of the z-axis of micromanipulator-2 is switched from position control to switched fuzzy-PD force control until the desired contact force level is achieved. During touching, fluorescence

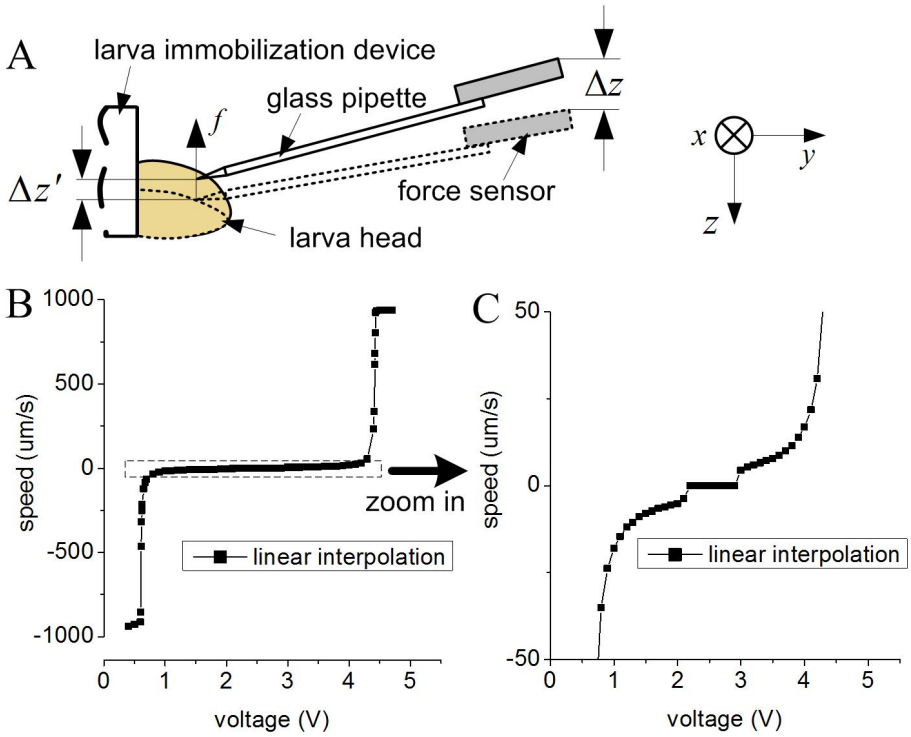

Figure 4–3: (A) Linear larva touch model. (B)(C) Micromanipulator calibration curve of the input voltage vs. output speed.

images were obtained from a fluorescence camera (EXi-Blue, QImaging). After the first larva is stimulated, the microscope is switched back to bright field and the next larva is brought into the field of view. The same operation procedure is repeated until all the four larvae are manipulated.

4.3 Larva Touch System Modeling

To design the switched fuzzy-PD controller, the larva touch model was first established. To be consistent with the previous biological study [7], the vertical component of the contact force was measured and controlled, a linear touch model exists (Fig. 4–3):

$$f = K\left(\Delta z - \Delta z'\right) = K\left(z - z_0 - \Delta z'\right) \tag{4.1}$$

where f is the contact force, z the vertical position of micromanipulator-2, z_0 the initial touching position, $\Delta z'$ the larva head deformation, and K the spring constant of the force sensor. During touching, the vertical (z-axis) speed of micromanipulator-2, $\dot{z}$, is controlled by an input voltage u.

The static relationship between $\dot{z}$ and u is:

$$\dot{z} = H(u) \tag{4.2}$$

We calibrated $H(u)$ to be nonlinear in the whole speed control range of -1000 μm/s to 1000 μm/s (Fig. 4–3(B)(C)), which is purposely designed by the vendor to maintain relatively low speeds (thus high positioning accuracy) in the major range of control voltage (1$\sim$4 V). In practice, we manually saturated $H(u)$ between $\pm$500 μm/s as speed limit to avoid large overshoots of the contact force.

The calibration was performed with following steps: A constant voltage was applied for 2 s to allow the micromanipulator to reach its constant speed, and the constant speed was then approximated by calculating the average speed during the 2 s interval, because 2 s is significantly longer than the characteristic time of the micromanipulator.

Note that $H(u)$ is in fact the steady-state speed of the z-axis of micromanipulator-2 under a given input voltage. Due to the dynamics of the micromanipulator, there is a time delay between the application of the input voltage and the achievement of the steady-state speed. In addition, there are other factors that contribute to the time-delay characteristic of the entire contact force regulation system, including transmission time of control commands, response time of the force sensor, calculation time of the control law, and dynamics of the larva body upon touching. Previous research on control of time-delay systems showed that the controller could be designed based on a simplified deadtime-free system model and the ignored time-delay effect could be taken into account, after the controller is designed, by implementing a Smith-like predictor [23]. Thus, we first established the switched fuzzy-PD controller by ignoring the time-delay characteristic of the contact force regulation system and assuming the manipulator immediately reaches its steady-state speed once an input voltage is applied. The compensation for the system's time-delay effect, which corresponds to the predictor block in Fig. 4–4, will be discussed in Section 4.6.3 after the controller is designed.

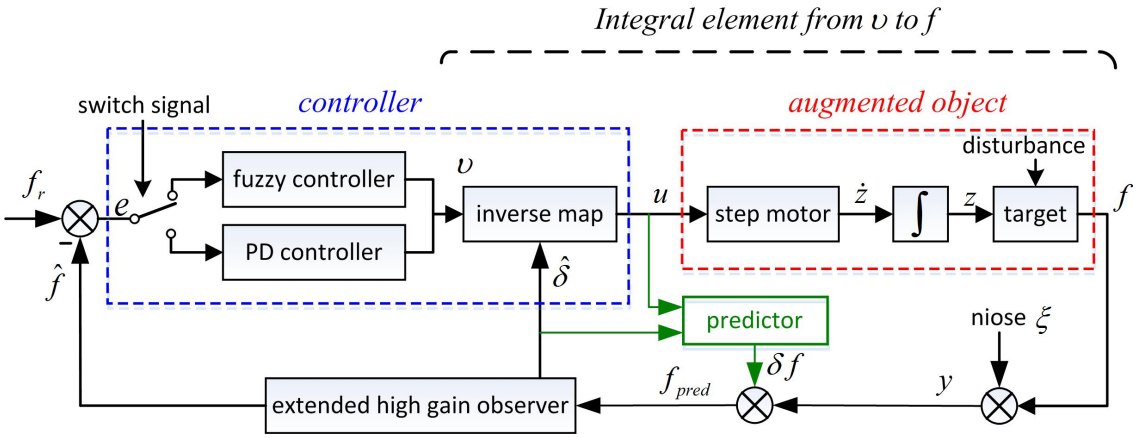

Figure 4–4: Control system architecture.

Combining (4.2) with the time derivative of (4.1), and including the calibration error (e_m) of $H(u)$ yield the final system model:

$$\dot{f} = KH(u) - K\Delta\dot{z}' + e_m \tag{4.3}$$

Combining the unknown $K\Delta\dot{z}'$ and e_m into an overall modeling error δ, the system model becomes:

$$\begin{cases} \dot{f} = KH(u) + \delta \\ y = f + \xi \end{cases} \tag{4.4}$$

where y is the measured contact force and equals the real force f plus the noise ξ. The time derivative of δ was assumed to be bounded. Sources of the modeling error include calibration error of the force sensor, disturbance from the live larva, and calibration error of the micromanipulator.

One may notice that the material properties of larva head is not explicitly shown in (4.4), but but it has been included in the overall unknown term $\delta = K\Delta\dot{z}' + e_m$ (in which the $\dot{z}'$ reflects the mechanical property of the larva head). This consideration avoids the necessity of measuring the heads mechanical property, which is cumbersome to measured and different in quantity from one larva to another. Once the mechanical property of the larva head is treated as a part of the total unknown term δ, it could always be estimated by the proposed noise-insenstive EHGO.

4.4 Overall Control Architecture

The proposed system control architecture is shown in Fig. 4–4. Denote $KH(u)+\delta$ as υ, the first equation of (4.4) becomes a linear form (marked as "*integral element from* υ to f" in Fig. 4–4)

$$\dot{f} = \upsilon \tag{4.5}$$

where υ is a virtual control input. Once υ is determined by the fuzzy or PD control law, the real control input u could be calculated by (marked as "*inverse map*" in Fig. 4–4)

$$u = H^{-1}\left(\frac{\upsilon-\delta}{K}\right) \tag{4.6}$$

where δ is obtained by a noise-insensitive revised EHGO. Note that $H(u)$ is not strictly monotone at dead zone. Therefore, we additionally define $H^{-1}(0)=2.5$ to make $H(u)$ reversible (the motor of the micromanipulator has a zero speed at an input of 2.5 V).

To compensate the time-delay effect of the force regulation system, a Smith-like predictor is used to estimate the difference between the delayed and non-delayed forces. The feedback force is then compensated to be non-delayed but with measurement noise, denoted by f_{pred} in Fig. 4–4. This value is then injected into the noise insensitive EHGO to produce an estimation of the system modeling error $\hat{\delta}$, which is finally used to generate the real control input u.

4.5 Observer Design and Simulation

4.5.1 Observer Design

If the measured contact force y was denoised, a conventional EHGO could guarantee a fast estimation of δ:

$$\begin{cases} \dot{\hat{f}} = KH(u) + \hat{\delta} - \frac{k_1}{\varepsilon}\left(\hat{f}-y\right) \\ \dot{\hat{\delta}} = -\frac{k_2}{\varepsilon^2}\left(\hat{f}-y\right) \end{cases} \tag{4.7}$$

where $\hat{f}$ and $\hat{\delta}$ are estimations of f and δ, k_1 and k_2 are gains, and ε is a small number to make the two gains high. This conventional EHGO works well if the contact force y does not include measurement noise. However, the small forces in robotic micromanipulation y) are always noisy,

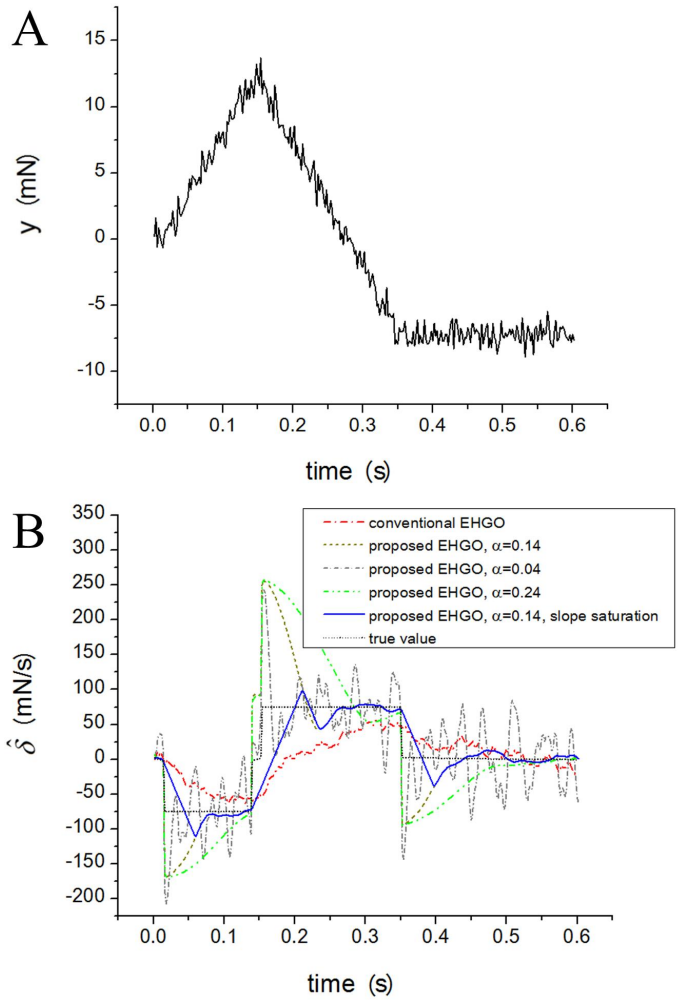

Figure 4–5: Simulation results of the conventional and revised EHGOs. (A) Input force signal with white noise. (B) Estimation results.

and the data noise (ξ in (4.4)) will be also amplified by the high gain of the EHGO and eventually destabilize the system. Here, we propose a revised noise-insensitive EHGO by substituting y with its smooth (differentiable) estimation g_1:

$$\begin{cases} \dot{\hat{f}} = KH(u) + \hat{\delta} - \frac{k_1}{\varepsilon}\left(\hat{f} - g_1\right) \\ \dot{\hat{\delta}} = -\frac{k_2}{\varepsilon^2}\left(\hat{f} - g_1\right) \\ \dot{g}_1 = g_2 \\ \dot{g}_2 = g_3 \\ \dot{g}_3 = \frac{1}{\alpha^3} h\left(g_1 - y, \alpha g_2, \alpha^2 g_3\right) \end{cases} \tag{4.8}$$

where $h(x)$ is a function that satisfies the continuity assumption (*Assumption* 4 in [24]), and α is a parameter that affects the noise attenuation performance of EHGO. The function $h(x)$ used in the revised EHGO is

$$\begin{aligned} h\left(g_1 - y, \alpha g_2, \alpha^2 g_3\right) &= -4 \cdot 2^{\frac{3}{5}} \left(g_1 - y + (\alpha g_2)^{\frac{9}{7}}\right)^{\frac{1}{3}} \\ &\quad - 4 \cdot \left(\alpha^2 g_3\right)^{\frac{3}{5}} \end{aligned} \tag{4.9}$$

This observer also requires that α and $\dot{\delta}$ (the time derivative of true modeling error δ) do not exceed the bounds, as defined in the Theorem 4 in [25]. These assumptions are necessary to make a lemma hold [26] to prove this observer. g_1 and its derivatives g_2 and g_3 form a subsystem acting as a filter and differentiator of y. The observer parameters (k_1, k_2, ε, and α) were determined through simulations in MATLAB SIMULINK (see Section 4.5.2), and their final values used in our experiments are: $k_1 = 50$, $k_2 = 1000$, $\varepsilon = 0.1$, and $\alpha = 0.14$.

The idea of proving the observer is summarized as follows, and the detailed proof is provided in the Appendix. The difference between g_1 and f could be bounded by Lyapunov analysis. Then, by discussing the stability of the equation governing $g_1 - \hat{f}$, the observer can be proved. The order of estimation errors are $|\delta - \hat{\delta}| = O(\alpha^{m-1})$ and $|f - \hat{f}| = O(\alpha^m)$, where $m \geq 3$. In principle, the parameter m can be designed arbitrarily large by choosing appropriate $h(x)$ [25], to achieve higher noise attenuation. However, this will also slow down the convergence of the EHGO and make it

less sensitive to rapidly varying modeling errors. To reach a good compromise, we chose the lower bound of m to be 3 [24], because, under this condition ($m \geq 3$), the subsystem formed by g_1, g_2 and g_3 has been verified to have good estimation performance [24, 26]. This ensures g_1 to serve as a good substitute for y, which is injected into the observer to replace y.

4.5.2 Observer Simulation and Parameter Determination

The observer parameters k_1, k_2, ε and α were calibrated via simulations conducted in MATLAB SIMULINK to optimize its performance. It is a common practice to firstly determine the values of k_1, k_2 and ε by assuming a denoised contact force y and conducting simulations of the conventional EHGO (4.7). The input of the conventional EHGO is the denoised force measurement (f) and the output is the estimated modeling error $\hat{\delta}$. We chose values of k_1, k_2, and ε that provided fast convergence (rising time less than 0.01 s for a step force input y), no overshoot, and no steady-state oscillation (simulation results not shown). The determined parameter values are: $k_1 = 50$, $k_2 = 1000$ and $\varepsilon = 0.1$.

The second step was to simulate the noise-insensitive EHGO to determine the value of α. We performed the simulation in the worst case scenario, in which the modeling error was set as a three-step form (Fig. 4–5(B)) and varied at large amplitudes and stepwise changes. The input force signal (y) for simulating the revised EHGO has high-level noises (Fig. 4–5(A)), and the simulation output was the estimated modeling error $\hat{\delta}$. We compared the estimated value by the EHGO with the true value δ, and evaluated the EHGO performance. We used the values of parameters k_1, k_2 and ε that were determined in the simulation of the conventional EHGO, and adjusted the value of α to achieve satisfactory performance of the revised EHGO in the simulations. Fig. 4–5(B) shows the simulation results of the estimated errors $\hat{\varepsilon}$ with different values of α. We found that a smaller α made the EHGO respond faster but oscillate more, and vise versa. Finally, we choose $\alpha = 0.14$ as a compromise between response time and smoothness of the error estimation. Another issue we identified in the simulation was the peaking phenomenon which leads to high overshoot of the estimation. To reduce it, the slope of $\hat{\delta}$ was saturated at ± 2500 mN/s. As shown in Fig. 4–5(B), with the slope saturation, the estimated error from the revised EHGO converged to the

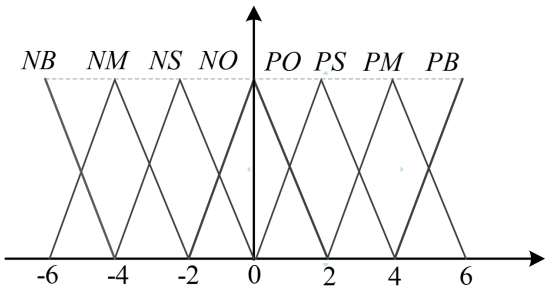

Figure 4–6: Membership functions of the fuzzy sets used in the fuzzy controller design.

Table 4–1: Fuzzy Control Rules

	NB(ec)	NM(ec)	NS(ec)	ZO(ec)	PS(ec)	PM(ec)	PB(ec)
NB(e)	PB	PB	PB	PM	PM	ZO	ZO
NM(e)	PB	PB	PB	PM	PM	ZO	ZO
NS(e)	PM	PM	PM	ZO	ZO	NS	NS
NO(e)	PM	PM	PS	ZO	NS	NM	NM
PO(e)	PM	PM	PS	ZO	NS	NM	NM
PS(e)	PS	PS	ZO	NM	NM	NM	NM
PM(e)	ZO	ZO	NM	NB	NB	NB	NB
PB(e)	ZO	ZO	NM	NB	NB	NB	NB

true value within 0.1 s with significantly reduced peaking phenomenon, while the conventional EHGO does not converge for the first two steps because of the force measurement noise. With the determined observer parameters, the performance of the revised EHGO is satisfying under the worst case scenario. These parameter values are then fixed throughout the experiments.

4.6 Switched Fuzzy-PD Control

In this section, the fuzzy control algorithm and the switch between the fuzzy and PD control laws are discussed in detail. The basic idea of fuzzy control can be described as follows. The controller translates a vague description (such as "high error and high error changing rate") into numerical values via membership functions, then searches the corresponding vague control input from a look-up table of control rules based on human experience (such as "the higher the error and its changing rate are, the higher the control input is"), and finally translates the vague control input back into a numerical value using a defuzzification method. For conciseness, we denote $e = f_r - \hat{f}$ and $ec = \dot{e} = \dot{f}_r - \dot{\hat{f}}$, where e is the system error signal (Fig. 4–4).

4.6.1 Fuzzy Control

The error e and error change rate ec are described by fuzzy sets (NB, NM, NS, NO, PO, PS, PM, PB) and (NB, NM, NS, ZO, PS, PM, PB), respectively. The membership functions of all the concerned fuzzy sets are shown in Fig. 4–6, with a universe of $[-6, 6]$. Then, as illustrated in Table 4–1, a fuzzy controller of 56 control rules are adopted in this research to improve the system performance. According to Table 4–1, we can formulate the fuzzy control rules as the following fuzzy relationships.

$$\begin{aligned} R_1 &= [NB(e) \times PB(v)] \cdot [NB(ec) \times PB(v)] \\ R_2 &= [NB(e) \times PB(v)] \cdot [NM(ec) \times PB(v)] \\ &\vdots \\ R_{56} &= [PB(e) \times NB(v)] \cdot [PB(ec) \times NB(v)] \end{aligned} \tag{4.10}$$

By fuzzy inference, the result $\bar{v}(\tau)$ is consequently represented as

$$\bar{v}(\tau) = \bar{v}_1(\tau) + \bar{v}_2(\tau) + \bar{v}_3(\tau) + \cdots + \bar{v}_{56}(\tau) \tag{4.11}$$

where

$$
\begin{aligned}
\bar{\upsilon}_1(\tau) &= \bar{e}(\tau)\cdot[NB(e)\times PB(\upsilon)]\cdot\bar{ec}(\tau) \\
&\qquad\qquad \cdot[NB(ec)\times PB(\upsilon)] \\
\bar{\upsilon}_2(\tau) &= \bar{e}(\tau)\cdot[NB(e)\times PB(\upsilon)]\cdot\bar{ec}(\tau) \\
&\qquad\qquad \cdot[NM(ec)\times PB(\upsilon)] \\
&\vdots \\
\bar{\upsilon}_{56}(\tau) &= \bar{e}(\tau)\cdot[PB(e)\times NB(\upsilon)]\cdot\bar{ec}(\tau) \\
&\qquad\qquad \cdot[PB(ec)\times NB(\upsilon)] \\
\bar{e}(\tau) &\triangleq \begin{cases} 0, & \tau\in[-6,e) \\ 1, & \tau=e \\ 0, & \tau\in(e,6] \end{cases} \\
\bar{ec}(\tau) &\triangleq \begin{cases} 0, & \tau\in[-6,ec) \\ 1, & \tau=ec \\ 0, & \tau\in(ec,6] \end{cases}
\end{aligned}
\tag{4.12}
$$

Then, adopting the centroid defuzzification method, we can denote the fuzzy control input υ_F as

$$
\upsilon_F = \frac{\int_{-6}^{6}\bar{\upsilon}(\tau)\tau d\tau}{\int_{-6}^{6}\bar{\upsilon}(\tau)d\tau} \tag{4.13}
$$

4.6.2 Fuzzy-PD Switching

The objective of developing the switched control scheme is to avoid the steady-state oscillation of fuzzy control. The control system makes the switching from fuzzy control to PD control according to the touch force response. Note that the desired touch forces (f_r in Fig. 4–4) for larva manipulation are usually stepwise signals. Thus, the steady state detection is much easier. Denote index $\sigma(t) = |\frac{e(t)}{f_r - f_0}| \times 100\%$, where f_0 is the initial state of system response. The switched fuzzy-PD controller is as follows:

$$v = \begin{cases} v_F, & \sigma(t) > \beta \\ v_{PD}, & otherwise \end{cases}$$

where

$$v_{PD} = k_p e + k_d ec$$

represents the PD control algorithm. The term β is a switch threshold whose value was chosen from trial-and-error experiments (see data in Section 4.7).

Remark 1: PD controller is adopted here instead of PID controller, because PD controller is already sufficient for eliminating the steady state error of step response when regulating an integral element as (4.5).

Remark 2: Here, the PD controller in the switched fuzzy-PD control algorithm is not the previous PID controller [8] with the integral term stripped off. In this research, we use the virtual input v as the PD input, whereas in our previous PID controller, the real input u was the PID input.

4.6.3 Time-Delay Compensation

As described in Section 4.3, the time-delay effect of the whole system was ignored during controller design. We now address the time-delay effect by implementing a Smith-like predictor. The Smith predictor is a critical part of our proposed control scheme, without which the system is prone to significant overshoot and oscillation, as we demonstrated using pure PID control (see data in Fig. 4–8(A)). An important parameter in designing the predictor is the deadtime. To determine its value, response curves of the contact force to open-loop stepwise voltage inputs of 4.1-4.5 V was experimentally obtained from five larvae, and two of which are shown in Fig. 4–7. The different input voltages resulted in different manipulator speeds ranging 25-500 μm/s (Fig. 4–3(B)(C)), thus different force response curves. Despite the different voltage inputs, the deadtime of the force regulation system remains relatively constant, which was measured to be 0.058$\pm$0.09 s (N = 5). The average value of 0.058 s was therefore used as the deadtime parameter for designing

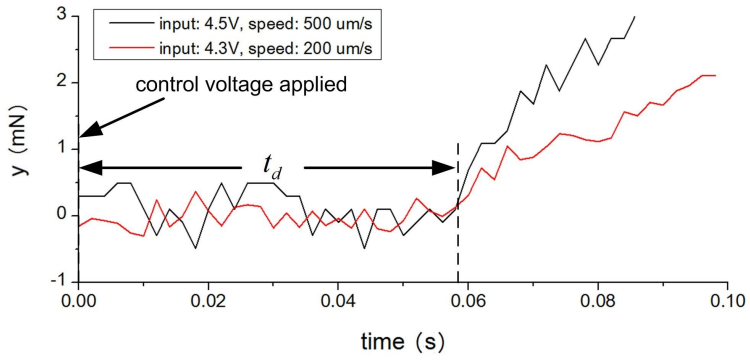

Figure 4–7: System deadtime test with step input.

the predictor. It has been also shown previously that the Smith-like predictor has a certain level of robustness against the uncertainty of deadtime [23].

A Smith-like predictor was then implemented to calculate the compensation value δf, as shown by the green dashed box in Fig. 4–4. The Smith-like predictor simulates

$$\begin{aligned} \dot{\hat{f}}_{dead\_time\_free} &= KH(u) + \hat{\delta} \\ \dot{\hat{f}}_{dead\_time} &= KH[u(t-t_d)] + \hat{\delta}(t-t_d) \\ \delta f &= \hat{f}_{dead\_time\_free} - \hat{f}_{dead\_time} \end{aligned} \tag{4.14}$$

and the prediction is given by:

$$f_{pred} = y + \delta f \tag{4.15}$$

The prediction f_{pred} is then substituted for y and is injected into the EHGO (Fig. 4–4).

4.7 Experimental Results and Discussions

The larva we used were transgenetically encoded with green fluorescent proteins (GFP) in a group of interconnected neurons expressing the cell-surface protein Turtle (Tutl). The change in fluorecence intensity inside these neurons reflects the transmission of neural signals. The Tutl-positive neurons have been shown to get involved in adjustment of the moving direction of a *Drosophila* larva, when a touch stimulus is applied to the larva's head [7]. This is a typical danger-escaping behavior of the *Drosophila* larva. We will use the developed micromanipulation system to

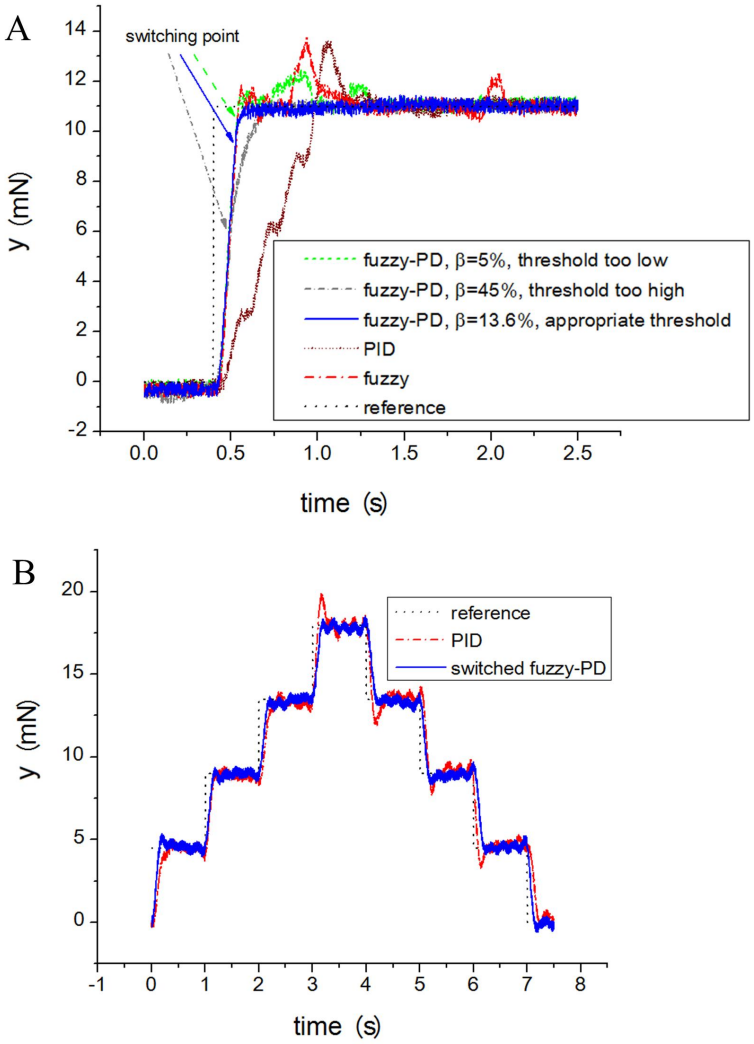

Figure 4–8: Comparison of step tracking performance of different control laws. (A) Single-step tracking results of the switched fuzzy-PD control with EHGO, the pure fuzzy control with EHGO, and the pure PID control. (B) Multi-step tracking results of the switched fuzzy-PD control and the PID control. The parameters of all the controllers were optimized, through trial-and-error experiments, before the presented tracking results were collected.

Table 4–2: Comparison of different controllers

Performance	PID	Fuzzy-PD appropriate threshold	Fuzzy-PD threshold too high	Fuzzy-PD threshold too low
	Value	Value (improvement)	Value (improvement)	Value (improvement)
Rising Time	0.612	0.11 (82%)	0.42 (31%)	0.11 (82%)
Overshoot	27.8%	0% (100%)	0% (100%)	14% (49%)
IAE_d	6.02/Medium	1.49/High (75%)	2.11/High (65%)	1.56/High (74%)

perform touch stimulation and calcium fluorescence imaging of immobilized larvae simultaneously, which could shed light on the possible neuron-level mechanisms that regulate this danger-escaping behavior.

We performed the force-controlled touching and fluorescence imaging simultaneously on eight third-instar larvae (4.5–5 mm long and 0.8–1 mm thick), and the operation success rate was 100%. Fig. 4–8(A) shows the step response curves of the system regulated by the switched fuzzy-PD control with EHGO with different thresholds, the pure fuzzy control with EHGO, and pure PID control. The switch threshold was determined in the following way. We wanted the switch threshold as small as possible to make full use of the fast convergence property of the fuzzy controller. However, the threshold should not be set too small either, otherwise the PD controller will become ineffective and the steady state oscillation could not be attenuated (Fig. 4–8(A)). We started with the value of 45% (sufficiently high) and gradually tuned down the threshold until a satisfying experimental result was achieved. The switch threshold was eventually determined to be $\beta = 13.6\%$ (control results shown in Fig.4–8(A)). One can observe that, compared to the PID control, the fuzzy control with EHGO provided a significantly shorter rise time of 0.11 s (vs. 0.612 s in PID control), but the oscillation at steady state was inevitable. The switched fuzzy-PD control with EHGO combined the advantages of fuzzy and PD control, demonstrating fast response (0.11 s) and negligible overshoot/oscillation. Overshoot neutralization was also shown in the comparison of multistep force tracking curves obtained from the switched fuzzy-PD control (with 13.6% threshold) and the PID control (Fig. 4–8(B)).

To quantify the performance improvement of the switched fuzzy-PD controller over the conventional PID controller, we adopted a standardized index for controller assessment, which is

denoted as IAE_d [27]. This index was developed to evaluate the step-response performance of a control system, and is defined as

$$IAE_d = \frac{\text{integration of absolute value of tracking error}}{\text{absolute value of step command} \times \text{system deadtime}} \tag{4.16}$$

IAE_d evaluates the overall performance of a controller. A smaller value of the IAE_d reflects better performance of the controller because short rising time, small overshoot and small oscillation all contribute to the reduction of IAE_d. A controller with $IAE_d < 2.8$ is usually considered to have high performance, and one with $IAE_d = 2.8 - 6.3$ is considered to have medium performance [27], and one with $IAE_d > 6.3$ is considered to have low performance.

The major performance parameters of the switched fuzzy-PD controller and the PID controller were compared and summarized in Table 4–2. Based on the values of IAE_d, even with a threshold value too high ($\alpha = 45\%$) or too low ($\alpha = 5\%$), the fuzzy-PD controller demonstrates shorter rising time and achieves better IAE_d index compared to the PID controller. This is due to the introduction of fuzzy logic that always tries to converge at the maximum speed. However, fuzzy logic generates significant steady-state oscillation, which requires the switch to the PD controller to restrain the oscillation. Failure to choose a proper switch threshold α may result in longer rising time (threshold too high) or greater steady state oscillation (threshold too low). Table 4–2 shows that, with an appropriate swith threshold ($\alpha = 13.6\%$), the switched fuzzy-PD controller has significant shorter rising time (82% improvement), zero overshoot (100% improvement), and much better overall performance (75% improvement) than the conventional PID controller.

We also performed preliminary biological experiments for simultaneous force-controlled touching and calcium fluorescence imaging of a *Drosophila* larva. The system run the switched fuzzy-PD controller to touch an immobilized larva twice at typical force levels of 2 mN and 4 mN (Fig. 4–9(B)) [7]. Each stimulus lasted for 4 s to simulate a touch in the real danger-escaping scenario, and a period of 56 s was arranged between two touch stimuli to make sure the larva recovered from the previous stimulus. Fig. 4–9(A) shows the fluorescence photograph of an immobilized larva before

touching. The red circle represents the location where fluorescence measurements were performed. During larva touching, the fluorescence camera recorded images at 2 frames per second. Fig. 4–9(C) shows time-lapse sequences of fluorescence images including an area of interest (AOI) for fluorescence measurement during the application of both stimuli. To quantify the calcium signal change, the average grayscale intensities of the AOI in all the images were measured and plotted in Fig. 4–9(D) as a function of time. The results reveal that the calcium fluorescence intensity inside the area of interest ramped up to its peak values in 1.5–2 s after the touch force was applied. Once the stimulus was removed, the fluorescence signal started to decrease and finally returned to its baseline levels in 3.5–4 s. The observed increasing and decreasing periods of the neural calcium signals in response to mechanical stimulation agree well with the results in [9]. The peak values of the calcium fluorescence in response to the 2 mN and 4 mN stiumli revealed no obvious difference. This demonstration confirms the feasibility of using the micromanipulation system, together with the force control scheme presented here, for studying transient signal transmission responses of the *Tutl*-positive neural circuitry to mechanical stimuli.

The main challenge we have tackled in this research was to provide fast and stable touching force to the larva with the existence of nonlinearity, disturbance, and feedback noise in the control loop. By adopting the noise-insensitive EHGO, we were able to estimate the uncertain errors on line with respect to the proposed model and compensate for the system nonlinearity and disturbance. The EHGO also served as a filter and reduced the measurement noise in the feedback. As a result, the control plant was transformed to a pure integral element (Fig. 4–4) that was amenable to high performance controllers. As shown in our experimental results (Fig. 4–8), the conventional fuzzy controller often led to steady state oscillations because of its high sensitivity to system feedback which magnified the influence of measurement noise. The proposed switched fuzzy-PD controller utilized the fuzzy control initially to achieve fast transient response and the PD control to rapidly reach the steady response without oscillation. The switched fuzzy-PD controller provided a rise time of 0.11 s and an zero overshot, which is much better than these of pure fuzzy controller (0.11 s and 28.7%) and PID controller (0.612 s and 27.8%). With the improved dynamic response, the

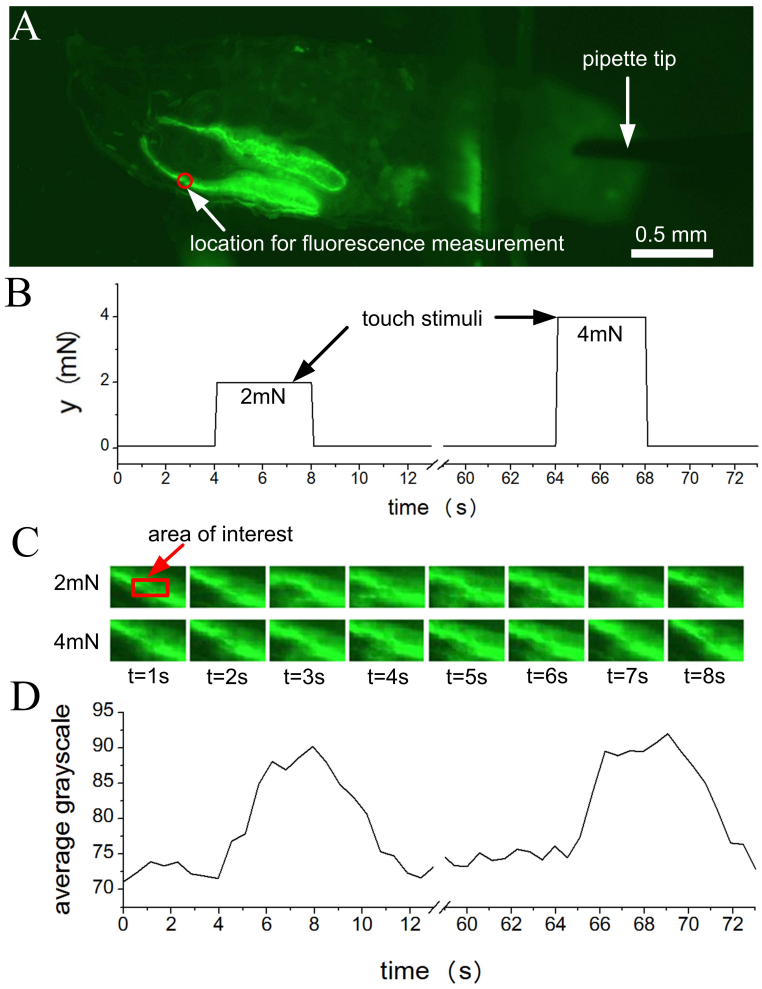

Figure 4–9: Experimental results of simultaneous touch stimulation and calcium fluorescence imaging of a *Drosophila* larva, at force levels of 2 mN and 4 mN. (A) A fluorescence image of the larva before touching. (B) The force curve of the two touch stimuli sequentially applied to the larva. (C) Consecutive fluorescence frames including an area of interest (AOI) for fluorecence imaging, during the application of two touch stimuli. (D) Average grayscale values of the fluorescence inside the AOI under the two stimuli.

robotic system will be applied to examining the neural mechanisms responsible for the danger-escaping behavior of *Drosophila* larvae. As many micromanipulation tasks require the control of interaction forces and the robotic systems usually have nonlinear components, external disturbance, and noisy force feedback [12, 13, 28], the control scheme we developed is also applicable to many other micromanipulation tasks requiring force control with rapid dynamic response.

4.8 Conclusion

This paper presented a novel switched fuzzy-PD control scheme for regulating contact forces during automated robotic mechanical stimulation of *Drosophila* larvae. The controller also employed an improved EHGO to compensate for undetermined system parameters and modeling errors. A simplified larva contact model was developed, whose modeling errors were compensated for by the observer. The observer overcome the disadvantage of conventional extended high gain observer (high sensitivity to measurement noise). The switched fuzzy-PD force controller inherited the fast dynamic response of a fuzzy controller, while overcoming its large overshoot and steady-state oscillation via the fuzzy-to-PD switch once the system reached the steady state. With the proposed control scheme, we demonstrated significantly improved dynamic performance of the robotic system over a conventional PID controller. Preliminary biological experiments of simultaneous touch stimulation and calcium fluorescence imaging of *Drosophila* larvae was also conducted.

4.9 Acknowledgment

The authors would like to thank the research group of Professor Yong Rao at the Research Institute of the McGill University Health Centre, for their assistance in preparation of the fluorescence *Drosophila* larvae.

Appendix

Theorem 1: Suppose $\dot{\delta}$ and α do not exceed the bounds defined in [25], the proposed observer (4.8) guarantees the following estimation error for the system described by (4.4):

$$\begin{aligned} \left|\hat{f} - f\right| &= O\left(\alpha^m\right) \\ \left|\hat{\delta} - \delta\right| &= O\left(\alpha^{m-1}\right) \end{aligned}$$

where $m \geq 3$.

Proof : We have

$$\begin{aligned} \dot{g}_1 &= \dot{f} + \dot{g}_1 - \dot{f} \\ &= KH(u) + \delta + \dot{g}_1 - \dot{f} \end{aligned} \tag{4.17}$$

Let

$$\begin{aligned} e_{o1} &= \hat{f} - g_1 \\ e_{o2} &= \hat{\delta} - \delta + \dot{f} - \dot{g}_1 \end{aligned}$$

From (4.4), (4.8) and (4.17), it is easy to verify that

$$\dot{e}_o = A_o e_o + L_o \sigma \tag{4.18}$$

where

$$\begin{aligned} e_o &= \left[e_{o1}\ e_{o2}\right]^T \\ A_o &= \begin{bmatrix} -\frac{k_1}{\varepsilon} & 1 \\ -\frac{k_2}{\varepsilon^2} & 0 \end{bmatrix} \\ L_o &= \begin{bmatrix} 0 \\ -1 \end{bmatrix} \\ \sigma &= \dot{\delta} + \ddot{g}_1 - \ddot{f} \end{aligned}$$

Note that the last three equations in (4.8) forms a subsystem presented in [24]. According to the noise-attenuation effect proven in [26], $\left|g_i - f^{(i-1)}(t)\right| = O\left(\alpha^{m-i+1}\right)$, where $m \geq 3$ and could be designed arbitrarily by choosing appropriate $h(x)$. The term σ is thus bounded:

$$\|\sigma\| = \left\|\dot{\delta}\right\| + O\left(\alpha\right) \tag{4.19}$$

The general solution of (4.18) is

$$e_o\left(t\right) = e^{A_o t} e_o\left(0\right) + \int_0^t e^{A_o(t-\tau)} L_o \sigma d\tau$$

The logarithmic norm of the solution could be bounded by

$$\begin{aligned} \|e_o\left(t\right)\| &\leq e^{\lambda_1 t}\|e_o\left(0\right)\| + l_b \int_0^t e^{A_o(t-\tau)} d\tau \\ &\leq e^{\lambda_1 t}\|e_o\left(0\right)\| + l_b \int_0^t e^{\lambda_1(t-\tau)} d\tau \\ &= e^{\lambda_1 t}\|e_o\left(0\right)\| + \frac{l_b}{-\lambda_1}\left(1 - e^{\lambda_1 t}\right) \end{aligned} \tag{4.20}$$

where λ_1 is the largest eigenvalue (or the one that has the smallest absolute value because λ_1 is negative) of matrix A_o, and l_b is the upper bound of $\|L_o\sigma\|$. With (4.19), the bound of (4.20) could be expressed as:

$$\|e_o\left(t\right)\| \leq e^{\lambda_1 t}\|e_o\left(0\right)\| + \frac{sup(\left\|\dot{\delta}\right\|) + O\left(\alpha\right)}{-\lambda_1}\left(1 - e^{\lambda_1 t}\right) \tag{4.21}$$

where $sup(\left\|\dot{\delta}\right\|)$ denotes the least upper bound of $\left\|\dot{\delta}\right\|$. By choosing sufficient large values of k_1 and k_2, one can readily verify that $\lambda_1 \to -\infty$, so $\|e_o\left(t\right)\| \to 0$. Finally, we have

$$\left|\hat{f} - f\right| \rightarrow |g_1 - f| = O\left(\alpha^m\right) \tag{4.22}$$

$$\left|\hat{\delta} - \delta\right| \rightarrow \left|\dot{g}_1 - \dot{f}\right| = O\left(\alpha^{m-1}\right) \tag{4.23}$$

This concludes the proof.

References

[1] Z. Lu, P. C. Chen, and W. Lin, "Force sensing and control in micromanipulation," *IEEE Trans. Syst., Man, Cybern. C, Appl. Rev.*, vol. 36, no. 6, pp. 713–724, 2006.

[2] X. Liu, Y. Sun, W. Wang, and B. M. Lansdorp, "Vision-based cellular force measurement using an elastic microfabricated device," *J. Micromech. Microeng.*, vol. 17, no. 7, p. 1281, 2007.

[3] X. Y. Liu, K. Kim, Y. Zhang, and Y. Sun, "Nanonewton force sensing and control in microrobotic cell manipulation," *Int. J. Robot. Res.*, vol. 28, no. 8, pp. 1065–1076, 2009.

[4] Y. Xie, D. Sun, H. Y. G. Tse, C. Liu, and S. H. Cheng, "Force sensing and manipulation strategy in robot-assisted microinjection on zebrafish embryos," *IEEE/ASME Trans. Mechatron.*, vol. 16, no. 6, pp. 1002–1010, 2011.

[5] A. Bolopion, H. Xie, D. S. Haliyo, and S. Régnier, "Haptic teleoperation for 3-d microassembly of spherical objects," *IEEE/ASME Trans. Mechatron.*, vol. 17, no. 1, pp. 116–127, 2012.

[6] H. Ladjal, J.-L. Hanus, A. Pillarisetti, C. Keefer, A. Ferreira, and J. P. Desai, "Reality-based real-time cell indentation simulator," *IEEE/ASME Tran. Mechatron.*, vol. 17, no. 2, pp. 239–250, 2012.

[7] Y. Zhou, S. Cameron, W.-T. Chang, Y. Rao, et al., "Control of directional change after mechanical stimulation in drosophila," *Mol. Brain*, vol. 5, no. 1, pp. 39–51, 2012.

[8] W. Zhang, A. Sobolevski, B. Li, Y. Rao, and X. Liu, "An automated force-controlled robotic micromanipulation system for mechanotransduction studies of drosophila larvae," *IEEE Trans. Autom. Sci. Eng.*, vol. 13, no. 2, pp. 789–797, 2016.

[9] Z. Yan, W. Zhang, Y. He, D. Gorczyca, Y. Xiang, L. E. Cheng, S. Meltzer, L. Y. Jan, and Y. N. Jan, "Drosophila nompc is a mechanotransduction channel subunit for gentle-touch sensation," *Nature*, vol. 493, no. 7431, pp. 221–225, 2013.

[10] K. Kim, X. Liu, Y. Zhang, and Y. Sun, "Nanonewton force-controlled manipulation of biological cells using a monolithic mems microgripper with two-axis force feedback," *J. Micromech. Microeng.*, vol. 18, no. 5, p. 055 013, 2008.

[11] Y. Xie, D. Sun, C. Liu, H. Tse, and S. Cheng, "A force control approach to a robot-assisted cell microinjection system," *Int. J. Robot. Res.*, vol. 29, no. 9, pp. 1222–1232, 2010.

[12] H. B. Huang, D. Sun, J. K. Mills, and S. H. Cheng, "Robotic cell injection system with position and force control: toward automatic batch biomanipulation," *IEEE Trans. Robot.*, vol. 25, no. 3, pp. 727–737, 2009.

[13] M. Boudaoud, Y. Le Gorrec, Y. Haddab, and P. Lutz, "Gain scheduling control of a nonlinear electrostatic microgripper: design by an eigenstructure assignment with an observer-based structure," *IEEE Trans. Control Syst. Technol.*, vol. 23, no. 4, pp. 1255–1267, 2015, ISSN: 1063-6536. DOI: 10.1109/TCST.2014.2362725.

[14] Y. Yin, P. Shi, and F. Liu, "Gain-scheduled robust fault detection on time-delay stochastic nonlinear systems," *IEEE Tran. Ind. Electron.*, vol. 58, no. 10, pp. 4908–4916, 2011, ISSN: 0278-0046. DOI: 10.1109/TIE.2010.2103537.

[15] Z. Chi, M. Jia, and Q. Xu, "Fuzzy pid feedback control of piezoelectric actuator with feedforward compensation," *Math. Probl. Eng.*, vol. 2014, 2014.

[16] R. Zhang, Q. Quan, and K.-Y. Cai, "Attitude control of a quadrotor aircraft subject to a class of time-varying disturbances," *IET Control Theory A*, vol. 5, no. 9, pp. 1140–1146, 2011.

[17] R. Madonski and P. Herman, "Method of sensor noise attenuation in high-gain observersexperimental verification on two laboratory systems," in *2012 IEEE International Symposium on Robotic and Sensors Environments (ROSE)*, IEEE, 2012, pp. 121–126.

[18] A. A. Prasov and H. K. Khalil, "A nonlinear high-gain observer for systems with measurement noise in a feedback control framework," *IEEE Trans. Automat. Contr.*, vol. 58, no. 3, pp. 569–580, 2013.

[19] K. Santa, S. Fatikow, and G. Felso, "Control of microassembly-robots by using fuzzy-logic and neural networks," *Comput. Ind.*, vol. 39, no. 3, pp. 219–227, 1999.

[20] J. Zhang, G. Li, and N. Xi, "Modeling and control of active end effector for the afm based nano robotic manipulators," in *2005 IEEE International Conference on Robotics and Automation, ICRA 2005*, IEEE, 2005, pp. 163–168.

[21] A. Boulkroune, M. Tadjine, M. MSaad, and M. Farza, "How to design a fuzzy adaptive controller based on observers for uncertain affine nonlinear systems," *Fuzzy Set Syst.*, vol. 159, no. 8, pp. 926–948, 2008.

[22] C. Li, S. Tong, and W. Wang, "Fuzzy adaptive high-gain-based observer backstepping control for siso nonlinear systems," *Inform. Sciences*, vol. 181, no. 11, pp. 2405–2421, 2011.

[23] C. Kravaris and R. A. Wright, "Deadtime compensation for nonlinear processes," *AIChE J.*, vol. 35, no. 9, pp. 1535–1542, 1989.

[24] X. Wang, Z. Chen, and G. Yang, "Finite-time-convergent differentiator based on singular perturbation technique," *IEEE Trans. Automat. Contr.*, vol. 52, no. 9, pp. 1731–1737, 2007.

[25] X. Wang and B. Shirinzadeh, "Rapid-convergent nonlinear differentiator," *Mech. Syst. Signal. Pr.*, vol. 28, pp. 414–431, 2012.

[26] J. Su, R. Zhang, X. Wang, and K.-Y. Cai, "Controlling a four-rotor aircraft based on noise-attenuation differentiator," *IET Control Theory A*, vol. 26, pp. 827–832, 2009.

[27] A. P. Swanda and D. E. Seborg, "Controller performance assessment based on setpoint response data," in *1999 American Control Conference*, IEEE, vol. 6, 1999, pp. 3863–3867.

[28] H. Xie and S. Régnier, "Three-dimensional automated micromanipulation using a nanotip gripper with multi-feedback," *J. Micromech. Microeng.*, vol. 19, no. 7, p. 075 009, 2009.

The connection between Chapter 4 and Chapter 5

Chapter 4 was mainly focused on an advanced force controller, which does not consider the dynamics of the micromanipulator. Further accommodating the micromanipulator dynamics could further improve the system performance, especially after the switch to PD control since the PD controller is model dependent. In Chapter 5, the micromanipulator dynamics will be taken into account, and several associated challenges, including insufficient feedback, measurement noise, and time delay, will be tackled by using a new compensation-prediction control scheme. This approach is applicable to any type of controllers. To highlight the effectiveness new scheme, the conventional PID controller is implemented together with the proposed scheme, and experimental comparisons are made with and without the scheme. The experimental results demonstrate that the improvement of control performance is purely enabled by the proposed scheme.

CHAPTER 5
A Model Compensation-Prediction Scheme for Control of Micromanipulation Systems with a Single Feedback Loop

A Model Compensation-Prediction Scheme for Control of Micromanipulation Systems with a Single Feedback Loop

Weize Zhang, Juntian Qu, Xuping Zhang, and Xinyu Liu*

Department of Mechanical Engineering, McGill University, 817 Sherbrooke Street West, Montreal, Quebec H3A 0C3, Canada

*Corresponding author: (xinyu.liu@mcgill.ca)

Submitted and under review.

Many micromanipulation systems employ sensor- less actuators and possess unknown modeling errors, feedback measurement noise, and time delays. Conventional model-based control schemes ignore some of these uncertainties, and thus sacrifice the control system performance. This paper presents a new model compensation-prediction scheme for micromanipu- lation systems that can be described by two-dimensional state- space models, estimate the unknown modeling errors from noisy single feedback measurement, and predict and compensate the system time delay. This approach combines two modeling errors into a single equivalent modeling error through mathematical transformation, and estimates the combined term using a noise- insensitive extended high-gain observer (EHGO). After removing the unknown term, the system is then transformed into a time invariant form, and a Smith predictor is implemented to predict and compensate the time delay. The effectiveness of the proposed compensation-prediction scheme is demonstrated by both numer- ical simulation and experiments of two typical micromanipulation systems, namely a robotic biosample stimulator and a material characterization microgripper. The results show that this method is able to significantly improve the control performance of a conventional PID controller, by simultaneously reducing the settling time and overshoot of the micromanipulation systems.

Index Terms-First order actuator, Modeling error, Measure- ment noise, Time delay, Compensation, Prediction, Performance index.

5.1 Introduction

Many micromanipulation systems employ large-scale or microelectromechanical systems (MEMS) based actuators to generate microscale motions and interact with micro-objects [1, 2, 3, 4, 5, 6, 7, 8, 9, 10]. Typical actuators used in micromanipulation include high-precision stepper motors [2, 5] and MEMS electrostatic and electrothermal actuators [3, 7], and these actuators usually do not have integrated position sensors for feedback control. Therefore, other feedback modalities, such as vision [2, 4, 5, 11, 6, 8] and force [3, 7, 12], have been utilized for guidance and/or closed-loop control of the micromanipulation systems. Additionally, the dynamics of these actuators needs to be considered in the control system, and is always coupled with the time-delay effect [13]. The control of micromanipulation systems is also prone to modeling errors and feedback measurement noise [14], making it difficult to implement model-based control methods (e.g., feed-forward compensation, model predictive control, and H-infinity control) to optimize performance.

This paper aims at developing a new control scheme for micromanipulation systems with single force feedback loop, which considers actuator dynamics and nonlinearity, time delays, unknown modeling errors, and measurement noises. Many micromanipulation systems with a single feedback loop can be described by a two-dimensional space-state model (2D systems). The first state variable is the system output to be controlled (e.g., interaction forces in demonstration experiments of this work), and the second state variable is the output of the actuator (which could be the displacement or speed). In principle, the modeling errors, which are reflected by two small terms in the differential equations of the 2D system, can be estimated from the feedback signal using an observer. However, because the force feedback is not directly coupled with output of actuator (i.e., the second state variable), the original 2D space-state model of the micromanipulation system is unobservable.

To address this problem, the most common way is to ignore details of the system model and implement a simple proportional-integral-derivative (PID) controller, which guarantees zero static error. However, because the system dynamics is not considered in the controller design and the time delay exists, the PID controller usually leads to large overshoots [15]. By tuning

the PID coefficients, the overshoot may be reduced but settling time is also sacrificed [16]. The Smith predictor is ideal to treat the time-delay effect of control systems but requires a precise time invariant model [17], which is unsuitable for our case here because unknown modeling errors exist in the micromanipulation systems. Another method is to ignore modeling errors completely to obtain a simplified linear system, and analyze it in frequency domain [18]. However, this method leads to long settling time and static state oscillations.

Advanced control schemes have also been proposed for a variety of micromanipulation systems. H-infinity and μ-synthesis were investigated in [14] to account for modeling errors of piezoelectric microactuators. These methods require the feedback of the actuator output, which can not be implemented in systems with sensorless actuators. Gain scheduling was adopted in [19] to adaptively compensate for system nonlinearity, but modeling errors were neglected in this study. In [20], unknown terms were estimated during the initial step of control system. This method could only treat constant modeling errors, and causes large overshoot during each estimation. In [21], an iterative procedure, based on an eigenstructure assignment methodology coupled with auto-scheduling, was proposed to treat model uncertainties. In [22], a fuzzy-PID controller with feedforward compensation was adopted to account for model uncertainties. However, in these two systems [21, 22], only simulations were conducted and no real control experiments were demonstrated. In [23], a sliding mode controller was employed for a gripper system to compensate for uncertainties, but this method is unable to tackle time delay. Besides, the system was only tested on a hard material (copper) without any effect of the material compliance (e.g., elasticity and viscoelasticity). In our case, soft materials are manipulated and the slow dynamics of these soft materials will bring in additional uncertainties in the control system. Passive bilateral control was investigated in [24] to account for time delays, but this approach showed large steady state errors. Moreover, all control methods introduced above fail to account for time-varying modeling errors, time delays, and feedback measurement noises simultaneously.

In this paper, we present a new model compensation-prediction scheme for control of micromanipulation systems with single force feedback loop. The proposed scheme describes the system in a

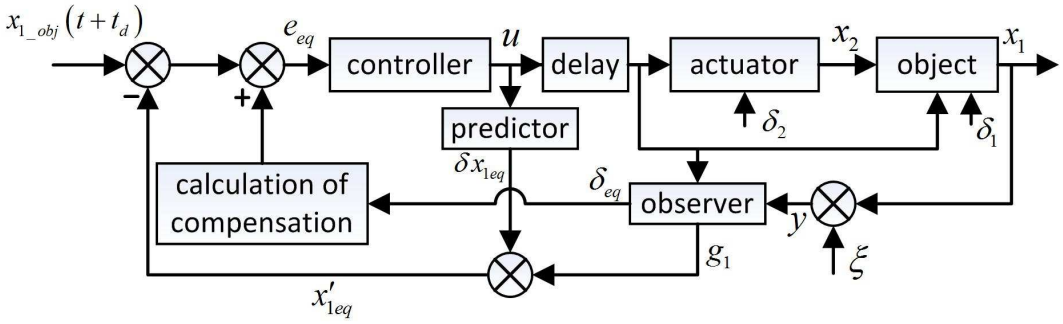

Figure 5–1: Architecture of the compensation-prediction scheme.

2D state-space model, and combines modeling error terms from the two differential equations of the 2D system into a single equivalent error term, making the system observable. A noise-insensitive extended high-gain observer (EHGO) is used for estimating the combined error term from the single force feedback loop. After compensating this unknown term by the EHGO, the system is then transformed into a time invariant form, and a Smith predictor is implemented to compensate the time-delay effect. It is finally proved that this approach is equivalent to adding a compensation to the conventional Smith predictor. We illustrate the effectiveness of this compensation-prediction scheme with numerical simulations, and then test it on two typical force-controlled micromanipulation systems: a robotic biosample stimulator and a microelectromechanical systems (MEMS) based microgripper. Both the simulation and experimental results demonstrate that the proposed scheme is effective in reducing settling time and system overshoot simultaneously, despite the presence of modelling errors, feedback measurement noises, and time delays.

5.2 Compensation-Prediction Scheme Overview

A general architecture of the model compensation-prediction scheme is show in Fig. 5–1. The actuator in the micromanipulation system causes a time delay due to its dynamics, backlash of the transmission mechanism, signal transmission delays, and so on. The system output, x_1, is the interaction force between the end-effector and the target micro-object, and its objective (reference) value is denoted by x_{1_obj}. Note that only single and multi-step force commands are used because most of the force control tasks in robotic micromanipulation only involves the regulation of stepwise forces [3, 12, 15, 20]. The tracking error of x_1 is denoted by $e_1(t) = x_{1\_obj}(t+t_d) - x_1(t)$. Note that we

use $x_{1\_obj}(t+t_d)$ instead of $x_{1\_obj}(t)$ as reference to highlight the fact that the time-delayed system will always response t_d later than the step command. The system has two unknown modeling errors (δ_1 and δ_2) in the two differential equations of the 2D state-space model respectively (see Section 5.3), and these errors are time-varying because they are affected by external disturbances. To make the system observable from the single force feedback loop, we combine them into an equivalent modeling error (δ_{eq} in Fig. 5–1) through mathematical transformation, and then estimate δ_{eq} using a modified EHGO insenstive to the force measurement noise (ξ in Fig. 5–1). The EHGO also provides a denoised value (g_1) of the force measurement y. A Smith predictor is implemented to calculate a correction (δx_{1eq}) to the tracking error caused by the system time delay. Based on the estimation (δ_{eq}) of the equivalent modeling error, a compensation is added to further correct the tracking error, and the corrected error (e_{eq}) is then injected into a controller to calculate the control input u.

5.3 Modeling

To simplify the description, here we define two types of models: The term "real model" is defined as the equations that represent the true dynamics of the system [25, 26] (including the modeling errors). The term "ideal model" is defined as the real model without the modeling error terms. This is equivalent to say that the real could always be written as an ideal model plus modeling errors.

The real model of the micromanipulation system contains time delay, unmeasurable actuator output (due to the lack of displacement feedback), time-varying modeling errors, and feedback measurement noise. We establish a 2D state-space model in a general form as follows:

$$\begin{cases} \dot{x}_1 = ax_1 + bx_2 + cu(t-t_d) + \delta_1 \\ \dot{x}_2 = \frac{1}{T_m}\left[u(t-t_d) - x_2\right] + \delta_2 \end{cases} \tag{5.1}$$

where x_1 and x_2 are state variables, and u is the control input and is time-delayed by t_d. The second differential equation describes the actuator (treated as a first-order model) with unmeasurable output x_2, where T_m is the actuator time constant and can be quantified via step-input testing

of the actuator [13]. Note that there are also some actuators in micromanipulation systems with second-order behaviors (MEMS electrostatic actuators), and the proposed compensation-prediction scheme is only limited to actuators with first-order behaviors. The terms δ_1 and δ_2 represent the total unknown modeling errors in each equation. The parameters a, b, c, and t_d are constants related to the system's physical parameters and can be estimated or measured from the system. The system model (5.1) is robust to the estimation/measurement errors of these parameters since these errors can be always included in the total modeling errors (δ_1 and δ_2). These errors are dependent on x_1, x_2 and u. *Assumption* 1: It is assumed that δ_1, δ_2, and the time derivative of δ_1 are all bounded; and $a \leq 0$. The restriction on a is valid for the two case studies in our investigation.

One may notice that, since the statistic property of the real model is unknown, the distribution laws of δ_1 and δ_2 are thus undetermined. However, *Assumption* 1 is the mathematical constraint on δ_1 and δ_2, and we will prove in Section 5.4.1 that *Assumption* 1 is sufficient to make the EHGO to work properly.

Physically, the variables x_1 and x_2 are the force and the output of the actuator, respectively. The system model (5.1) is a generalized form of typical force controlled micromanipulation systems, as given by (5.23) and (5.25) to be discussed in Section 5.6. Note that not all parameters of in (5.1) will appear in experimental cases since (5.1) is a generalize form. For instance, in the first experimental study described with (5.23), we have $a = c = 0$.

Note that there are also some actuators in micromanipulation systems with second-order behaviors (MEMS electrostatic actuators), and the proposed compensation-prediction scheme is only limited to actuators with first-order behaviors. DC motors and thermal actuators can be well approximated with first-order model [27, 28].

Note that in some cases, the control input must be linearized with a one-to-one mapping $H(u)$, if the actuator is nonlinear. For instance, a MEMS V-beam thermal actuator has a nonlinear relationship between its control voltage and output displacement [3]. If the actuator displacement is used as the control input, a one-to-one mapping, determined by the actuator calibration data, is

needed to convert the control voltage (output from the controller) into the actuator displacement (control input of the 2D state-space model). The actuator displacement can be described with a first-order linear system, and the second equation of (5.1) in this case could be written as

$$\dot{x}_2 = \frac{1}{T_m}\left\{H[u(t-t_d)] - x_2\right\} + \delta_2 \tag{5.2}$$

5.4 Model Transformation

5.4.1 Combination of Unknown Terms

One major difficulty of directly using the 2D model is that the system only has single feedback loop, thus making it impossible to estimate both unknown modeling errors ($\delta_1$and δ_2). Our idea is to combine two unknown terms into an equivalent single term δ_{eq} via mathematical transformation. We start the conversion with decomposing δ_2 into:

$$\begin{aligned} \delta_{21} &= \delta_2 - \tfrac{1}{T_m} e^{-\frac{t}{T_m}} \int_0^t \delta_2 e^{\frac{\tau}{T_m}} d\tau \\ \delta_{22} &= \tfrac{1}{T_m} e^{-\frac{t}{T_m}} \int_0^t \delta_2 e^{\frac{\tau}{T_m}} d\tau \end{aligned} \tag{5.3}$$

where $\delta_2 = \delta_{21} + \delta_{22}$, and that

$$\frac{d}{dt}\left(x_2 - T_m\delta_{22}\right) = \frac{1}{T_m}\left[u(t-t_d) - (x_2 - T_m\delta_{22})\right] \tag{5.4}$$

The second state variable x_2 could be replaced by $x_2 - T_m\delta_{22}$ because this term could be considered as a whole. A change of variable could be applied. Let:

$$\begin{aligned} x_{2eq} &= x_2 - T_m\delta_{22} \\ \delta_{eq} &= \delta_1 + be^{-\frac{t}{T_m}} \int_0^t \delta_2 e^{\frac{\tau}{T_m}} d\tau \end{aligned} \tag{5.5}$$

It is easy to show that

$$\begin{cases} \dot{x}_1 = ax_1 + bx_{2eq} + cu(t-t_d) + \delta_{eq} \\ \dot{x}_{2eq} = \frac{1}{T_m}\left[u(t-t_d) - x_{2eq}\right] \end{cases} \tag{5.6}$$

Now only one combined unknown term δ_{eq} exists in (5.6), which is a combination of δ_1 and δ_2. With *Assumption* 1, it is obvious that δ_{eq} and its time derivative are bounded. Next step will be to estimate δ_{eq} with a noise-insensitive EHGO to make the system free of unknown terms.

5.4.2 Noise-Insensitive EHGO

If the force measurement y is denoised, a traditional EHGO is able to estimate δ_{eq}. However, measurement noise is inevitable in the feedback signal. The noise will also be magnified by the high gain of the EHGO and may eventually destabilize the system. Here, a modified EHGO is adopted to estimate δ_{eq}[29]:

$$\begin{cases} \dot{\hat{x}}_1 = a\hat{x}_1 + b\hat{x}_{2eq} + cu(t-t_d) + \hat{\delta}_{eq} - \frac{k_1}{\varepsilon}\left(\hat{x}_1 - g_1\right) \\ \dot{\hat{x}}_{2eq} = \frac{1}{T_m}\left[u(t-t_d) - \hat{x}_{2eq}\right] - \frac{k_2}{\varepsilon^2}\left(\hat{x}_1 - g_1\right) \\ \dot{\hat{\delta}}_{eq} = -\frac{k_3}{\varepsilon^3}\left(\hat{x}_1 - g_1\right) \\ \dot{g}_1 = g_2 \\ \dot{g}_2 = g_3 \\ \dot{g}_3 = \frac{1}{\alpha^3} h\left(g_1 - y, \alpha g_2, \alpha^2 g_3\right) \end{cases} \tag{5.7}$$

where $h(x)$ is a function that satisfies the continuity assumption in [30], and g_1, g_2, and g_3 are extended state variables of a subsystem to attenuate the measurement noise [30]. It has been proven that the order of the estimation error is determined by $\left|\delta_{eq} - \hat{\delta}_{eq}\right| = O\left(\alpha^{m-1}\right)$ and $\left|\dot{\delta}_{eq} - \dot{\hat{\delta}}_{eq}\right| = O\left(\alpha^{m-2}\right)$, where the lower bound of the parameter m is 3 [31]. The term g_1 is also a filtered/denoised value of the feedback measurement y, and thus could serve as the estimation of x_1. The term g_2 is an estimation of $\dot{x}_1$, and will be used for controller implementation.

The parameters used in the EHGO are: $k_1 = 50$, $k_2 = 1000$, $\varepsilon = 0.1$ [29] and $\alpha = 0.04$ [30]. $h(x)$ used in this research is [30]:

$$\begin{aligned} h\left(g_1 - y, \alpha g_2, \alpha^2 g_3\right) &= -4 \cdot 2^{\frac{3}{5}} \left(g_1 - y + (\alpha g_2)^{\frac{9}{7}}\right)^{\frac{1}{3}} \\ &\quad - 4 \cdot \left(\alpha^2 g_3\right)^{\frac{3}{5}} \end{aligned} \tag{5.8}$$

With the selected parameters and $h(x)$, the EHGO has been verified to have good performance [29].

5.4.3 Smith Predictor for Time-Delay Compensation

The system is now time-delayed and has no unknown terms. However, the system is time variant due to the presence of δ_{eq}. One can implement a Smith predictor by ignoring δ_{eq} (this approach will be compared with our compensation-prediction scheme in the simulation and experiments), or with the estimation $\hat{\delta}_{eq}$ in (5.7). The latter is not recommended because the Smith predictor requires $\hat{\delta}_{eq}(t+t_d)$ instead of $\hat{\delta}_{eq}(t)$. Even one could estimate $\hat{\delta}_{eq}(t+t_d)$ with linear interpolation, it is easy to show that such approximation will cause a tracking error of $\int_0^t(\dot{\hat{\delta}}_{eq}-\dot{\delta}_{eq})t_d d\tau = \int_0^t O\left(\alpha^{m-2}\right)t_d d\tau$ which could not be bounded. In contrast, our proposed method has a bounded tracking error, as will be shown in Section V.

We first reform the system and express it into a time-invariant system. Let:

$$x_{1eq} = x_1 - e^{at}\int_0^t \delta_{eq} e^{-a\tau} d\tau \tag{5.9}$$

It is easy to verify that

$$\begin{cases} \dot{x}_{1eq} = a x_{1eq} + b x_{2eq} + cu(t-t_d) \\ \dot{x}_{2eq} = \frac{1}{T_m}\left[u(t-t_d) - x_{2eq}\right] \end{cases} \tag{5.10}$$

Now, the system representation is free of modeling errors, and the state vector variables have been changed to x_{1eq} and x_{2eq}. The conversion from old variables (x_1 and x_2) to new variables (x_{1eq} and x_{2eq}) is shown in (5.5) and (5.9). The Smith predictor simulates

$$\begin{cases} \dot{\hat{x}}_{1eq\_f} = a\hat{x}_{1eq\_f} + b\hat{x}_{2eq\_f} + cu \\ \dot{\hat{x}}_{2eq\_f} = \frac{1}{T_m}\left(u - \hat{x}_{2eq\_f}\right) \end{cases} \tag{5.11}$$

$$\begin{cases} \dot{\hat{x}}_{1eq} = a\hat{x}_{1eq} + b\hat{x}_{2eq} + cu(t-t_d) \\ \dot{\hat{x}}_{2eq} = \frac{1}{T_m}\left[u(t-t_d) - \hat{x}_{2eq}\right] \end{cases} \tag{5.12}$$

$$\delta x_{1eq} = \hat{x}_{1eq\_f} - \hat{x}_{1eq} \tag{5.13}$$

where $\hat{x}_{1eq}$ and $\hat{x}_{1eq\_f}$ are the estimations of x_{1eq} with and without dead time. The corrected feedback is

$$x'_{1eq} = x_{1eq} + \delta x_{1eq} \tag{5.14}$$

5.5 Controller Implementation

The objective of this research is to develop a new scheme for compensating modeling errors and predicting time delays from a single feedback loop, which could enhance the control performance of the micromanipulation system without the need to tune the controller. Thus, the conventional PID controller was implemented as an example, but the method is also applicable to other types of controllers.

Note that the corrected feedback $x'_{1eq}(t)$ is the estimated feedback at $t + t_d$, which equals to $x_{1eq}(t + t_d)$. Therefore, the objective value from which x'_{1eq} is subtracted should also be at $t + t_d$. Use (5.9) and suppose we want to stabilize x_1 at x_{1_obj}, and the command given by the compensation-prediction model is

$$x_{1eq\_obj}(t + t_d) = x_{1\_obj}(t + t_d) - e^{a(t+t_d)} \int_0^{t+t_d} \delta_{eq} e^{-a\tau} d\tau \tag{5.15}$$

Note that the integration in (5.15) requires the value of δ_{eq} in the time period $[t, t + t_d]$ to be known. We use linear interpolation to estimate the value of δ_{eq} in $[t, t + t_d]$:

$$\delta_{eq}(t + \Delta t) = \delta_{eq}(t) + \Delta t \dot{\hat{\delta}}_{eq} \tag{5.16}$$

where $\dot{\hat{\delta}}_{eq}$ is the estimated time derivative of δ_{eq} in Eq. 5.7. The PID controller is expressed as

$$u = K_p e_{eq} + K_I \int e_{eq} dt + K_d \dot{e}_{eq} \tag{5.17}$$

where K_p, K_I and K_d are PID coefficients, and

$$e_{eq}(t) = x_{1eq\_obj}(t + t_d) - x'_{1eq}(t) \tag{5.18}$$

Remark 1: It is easy to show that

$$\begin{aligned} e_{eq} =& x_{1\_obj} - (x_1 + \delta x_{1eq}) \\ &+ e^{at} \int_0^t \delta_{eq} e^{-a\tau} d\tau - e^{a(t+t_d)} \int_0^{t+t_d} \delta_{eq} e^{-a\tau} d\tau \end{aligned} \tag{5.19}$$

Note that when $\delta_1 = \delta_2 = 0$, we have $\delta_{eq} = 0$ and $e_{eq} = x_{1\_obj} - (x_1 + \delta x_{1eq})$. In this case e_{eq} is the conventional tracking error with Smith predictor correction. (5.19) indicates that, even with the presence of the modeling error, we could still implement a Smith predictor as if we had the precise model, except for adding a supplementary correction of $e^{at} \int_0^t \delta_{eq} e^{-a\tau} d\tau - e^{a(t+t_d)} \int_0^{t+t_d} \delta_{eq} e^{-a\tau} d\tau$ to compensate for the modeling error (which corresponds to the "calculation of compensation" block in Fig. 5–1). This significantly simplifies the implementation of the entire model compensation-prediction scheme.

With *Assumption* 1, it is straightforward to prove that the compensation term is bounded. Note that when $a = 0$, (5.9) is not bounded. However, since x_{1eq} is an intermediate term which is not used in calculating the compensation, the compensation term is still bounded. It is also straightforward to prove that, both the estimation error caused by the observer and the error caused by the linear interpolation (5.16) will contribute to the error of the compensation. The former is at the order of $O(\alpha^{m-1} t_d)$, and the latter is at the order of $O(\alpha^{m-2} t_d^2)$, making the total tracking error at the order of $O(\alpha^{m-1} t_d + \alpha^{m-2} t_d^2)$ ($m \geq 3$). It is desirable that t_d does not exceed the order of magnitude of α to constrain the total tracking error at the order of $O(\alpha^{m-1} t_d)$.

Remark 2: When implementing the PID controller, $\dot{e}_{eq}$ can be obtained by taking time derivative of (5.19), and then substituting (5.11), (5.12), (5.13) and (5.16) into $\dot{e}_{eq}$ to express it with known terms.

5.6 Simulation Results

5.6.1 Simulation with Modeling Errors Induced by Parameter Inaccuracy and Constant Disturbance

In the first step, we simulate a common scenario where modeling errors are induced by inaccuracy of model parameters. Thus, two models (one real model and one ideal model) need to

be formulated, and the modeling errors are the difference between these two models. Constant disturbances are added to the real model. The real model is:

$$\begin{cases} \dot{x}_1 = 1.5x_2 + 0.2u(t-0.1) + 10 \\ \dot{x}_2 = \frac{1}{0.15}\left[u(t-0.1) - x_2\right] + 10 \end{cases} \tag{5.20}$$

while the ideal model is:

$$\begin{cases} \dot{x}_1 = -0.15x_1 + x_2 + 0.15u(t-0.05) \\ \dot{x}_2 = \frac{1}{0.1}\left[u(t-0.05) - x_2\right] \end{cases} \tag{5.21}$$

Thus, the modeling errors (δ_1 and δ_2) are not only the constant disturbance, but also includes the contributions from parameter inaccuracy, i.e. the difference between the two differential equations in the real and ideal models. The feedback signal is $y = x_1 + \xi$, and the measurement noise ξ has a standard deviation of 1. The simulation and the experimental case studies were performed at a sampling frequency of 200 Hz. This frequency was lower than the one used in our previous studies [31], which was due to the hardware limitation as the control system required additional resources of the host computer to calculate the compensation term. However, the sampling interval of 0.005 s at 200 Hz is still significantly shorter than the characteristic time of the system, which has the same order of magnitude of the system dead time and the time constant of the first order actuator.

The model system presented above is suitable for demonstrating the effectiveness of the model compensation-prediction scheme, for the following reasons. First, all model parameters (including the time delay) are inaccurate. The conventional PID controller will inevitably generate large overshoots of the output, and the conventional Smith predictor will work improperly. Second, the time constant of the actuator and the dead time of the system are at the same order of magnitude as these of real micromanipulation systems.

For comparison, we first simulated PID control of the system without the model compensation-prediction scheme, and tuned the controller parameters to achieve the best step-response performance (in terms of the shortest settling time) with the Ziegler-Nichols method [32]. Note that the same method was also adopted for subsequent experiments. The final controller parameters

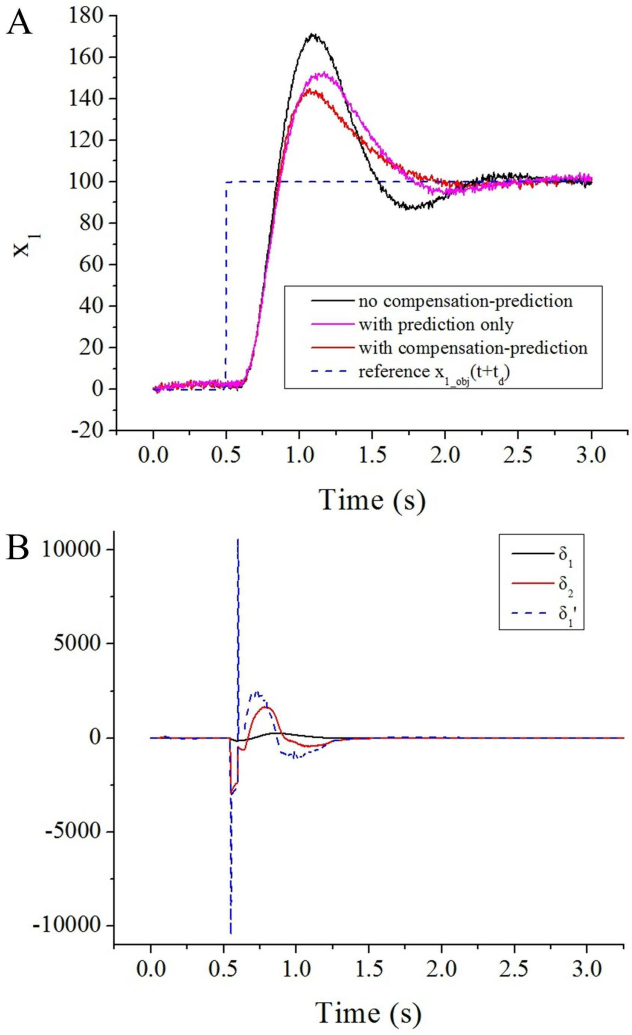

Figure 5–2: (A) Simulation results of a system with parameter inaccuracy and constant disturbance induced modeling errors. (B) Verification of *Assumption* 1.

are $K_p = 3$, $K_I = 5.5$, and $K_d = 0.2$. Then, we integrated the compensation-prediction scheme into the same PID controller (PID parameters unchanged). We also simulated performance of the PID controller with Smith predictor alone (PID parameters unchanged). Fig. 5–2 (A) shows the simulation results. The settling time of the model compensation-prediction scheme decreased from 2.21 s to 1.71 s compared to no-compensation-prediction scheme, and decreased from 2.02 s to 1.71 s compared to the prediction-only scheme. The overshoot of the model compensation-prediction scheme decreased from 70% to 40% compared to no-compensation-prediction scheme, and decreased from 52% to 40% compared to the prediction-only scheme. Fig. 5–2 (B) shows that δ_1, δ_2 and $\dot{\delta}_1$ are all bounded, and *Assumption* 1 thus is satisfied.

5.6.2 Simulation with Modeling Errors Induced by Parameter Inaccuracy and Sinusoidal Disturbance

The environmental disturbance (e.g., low-frequency oscillations of an anti-vibration table on which a micromanipulation system is placed) may also play a part in the total modeling errors. To simulate this effect and test the disturbance attenuation ability of the compensation-prediction scheme in the worst case scenario, two sinusoidal disturbances with high magnitudes are added to the real model:

$$\begin{cases} \dot{x}_1 = 1.5x_2 + 0.2u(t-0.1) + 30\cos(2\pi t) \\ \dot{x}_2 = \frac{1}{0.15}\left[u(t-0.1) - x_2\right] + 30\cos(2\pi t) \end{cases} \tag{5.22}$$

and the ideal model remains unchanged from (5.21). The frequency of the disturbance (1 Hz) is the same order of magnitude of an anti-vibration table, which is one of the primary sources of disturbance in our experimental setups. The magnitude of 30 is exaggerated to show the effectiveness of our control scheme.

For comparison, we first simulated PID control of the system without the model compensation-prediction scheme, and tuned the controller parameters to achieve the best step-response performance. In this case, the best performance refers to step-wise response with minimum steady state oscillations. The final controller parameters are $K_p = 3.7$, $K_I = 4.9$, and $K_d = 0.25$. Then, we integrated the compensation-prediction scheme into the same PID controller, then integrated the

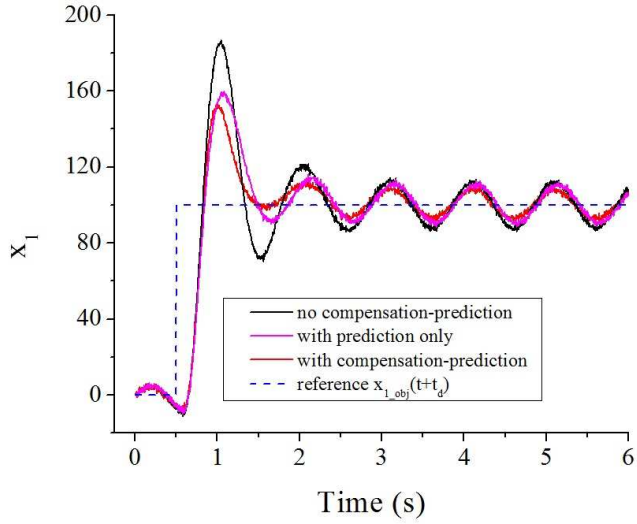

Figure 5–3: Simulation results of a system with parameter inaccuracy and heavy sinusoidal disturbance induced modeling errors.

Smith predictor alone, with the controller parameters unchanged. Simulation results are shown in Fig. 5–3. Steady state oscillation is inevitable in the output due to the heavy sinusoidal disturbance, but the implementation of compensation-prediction scheme reduced steady state oscillation from ±14% to ±10% compared to that of the compensation-prediction scheme, and from ±12% to ±10% compared to that of the prediction-only scheme.

5.7 Case Study Experiments and Discussion

5.7.1 Robotic Biosample Stimulator

We performed the first case study experiment of the model compensation-prediction scheme on a robotic biosample stimulator, as shown in Fig. 5–4(A). This system was developed for automatically applying force-controlled contact stimulation to the head of an immobilized live *Drosophila* larva to study its neural mechanisms of behavior responses to mechanical stimulation [29]. The system employs a glass needle, attached to a MEMS piezoresistive force sensor (AE801, Kronex), to touch the larva head, and a stepper-motor-driven micromanipulator (MP-285, Sutter) to move the needle vertically for larva touching. During operation, the micromanipulator moves the needle vertically towards the larva head (Fig. 5–4(B)) until a contact is established and detected by the force sensor. Then, the vertical position of the micromanipulator, z, is controlled to regulate

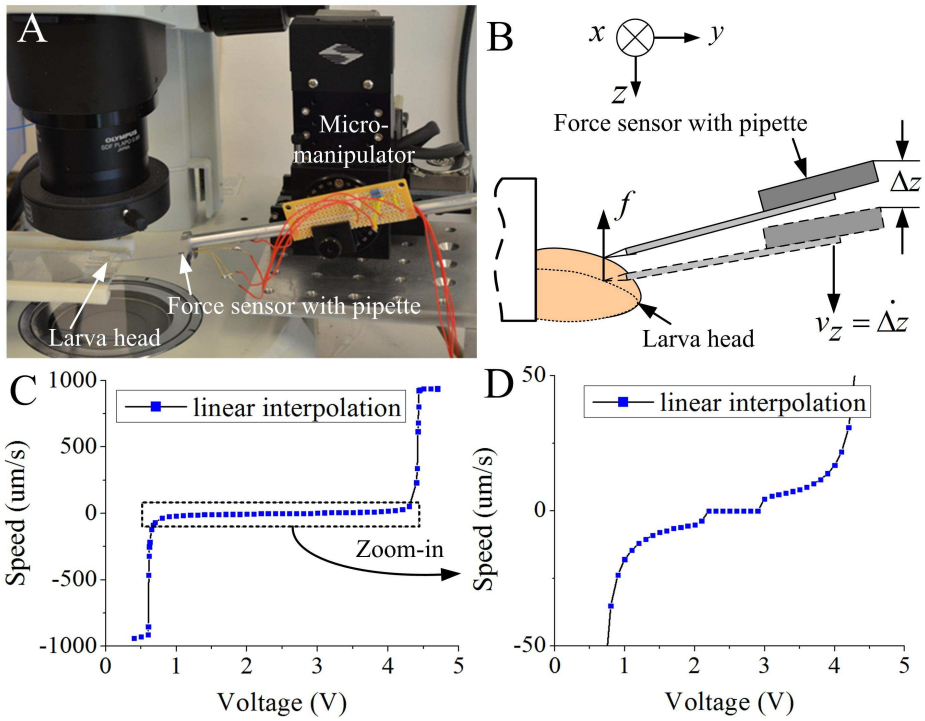

Figure 5–4: (A) General layout of the robotic biosample stimulator. (B) Simplified schematic of the robotic biosample stimulator with the variables used in the modeling. (C) and (D) The calibration of the function $H(u)$, which describes the voltage-maximum speed mapping of the manipulator.

the contact force. The vertical speed of the micromanipulator ($v_z = \dot{z}$) is controlled by the input voltage applied to the z-axis stepper motor. The force is converted into a voltage output by the force sensor, which provides the only force feedback loop in the system. The force sensor has a linear calibration curve of the output voltage vs. the input force.

The larva head can be safely assumed to be elastic. Thus, $f = K\Delta z$, where f is the contact force, K is the spring constant of the larva head, and Δz is the z-axis displacement of the micromanipulator. The time derivative of $f = K\Delta z$ leads to $\dot{f} = Kv_z$. Set the contact force f and v_z as the two state vector variables, and the state-space model of the system can be expressed by

$$\begin{cases} \dot{f} = Kv_z + \delta_1 \\ \dot{v}_z = \frac{1}{T_m}\left\{H\left[u\left(t - t_d\right)\right] - v_z\right\} + \delta_2 \\ y = f + \xi \end{cases} \tag{5.23}$$

where the second equation is a time-delayed, first-order model governing the z-axis of the micromanipulator. Note that the z-axis of the micromanipulator was calibrated to have a nonlinear relationship between its input voltage and output speed (Fig. 5–4(C)(D)). Therefore, a one-to-one mapping function $H(u)$, determined by the nonlinear calibration curve of the z-axis of the micromanipulator, was used for system linearization, which converted the real input (the control voltage u) into a virtual input (the vertical speed v_z). After the calculation of the virtual input v_z by the controller, the real input u is obtained via the inverse map of $H(u)$.

We implemented the PID control of the robotic stimulator with and without the model compensation-prediction scheme, and the parameters of the system model are $K = 200$ N/m, $T_m = 0.01$ s, and $t_d = 0.05$ s. The modeling errors δ_1 and δ_2 primarily arise from the estimation errors of the larva head compliance (K), and the calibration error of the function $H(u)$. The system was first tuned without the compensation-prediction scheme to achieve the best possible result (by minimizing settling time first, then minimizing overshoot without influencing settling time) for the single-step response, and the controller parameters were determined to be: $K_p = 150$, $K_I = 200$ and $K_d = 2$. Large overshoot is inevitable due to the presence of time delay [12]. Then

the controller parameters are inherited for the compensation-prediction and the prediction-only schemes. The red, black and pink curves in Fig. 5–5(A) show the single-step response of the system in three different schemes. A settling time of 0.8 s and an overshoot of 27% were achieved by the no-compensation-prediction scheme, and the integration of the model compensation-prediction scheme reduced the settling time to 0.3 s (62.5% improvement) and the overshoot to 5% (81.5% improvement). Compared with the prediction-only scheme (settling time 0.39 s, overshoot 11%), the improvements are 23.1% and 54.5%, respectively. The multi-step response of the system also shows similar improvements, as illustrated in Fig. 5–5(B).

5.7.2 Force-Controlled MEMS Microgripper

The second case study was demonstrated on a force-controlled MEMS microgripper [15], as shown in Fig. 5–6. The microgripper has an active gripping arm (the left arm in Fig. 5–6(B)) driven by a V-beam thermal actuator, and a force sensing arm (the right arm in Fig. 5–6(B)) attached to a capacitive force sensor. The device was used as a soft material microtester [15], for which a microscale soft object was grasped between the two gripping arm tips, and the gripping force and the induced deformation of the object were measured and used to calculate elastic or viscoelastic properties of the material. In this case study experiment, we grasped soft micro-cubes made from polydimethylsiloxane (PDMS), and demonstrated control of the grasping force using the model compensation-prediction scheme.

Taking the microgripper as the plant, the control input (u) is the actuation voltage applied to the thermal actuator, which regulates the displacement of the left arm tip (Δx in Fig. 5–6(B)). Once a micro-object was grasped between the two tips, the grasping force was controlled by adjusting the control input u. The force was measured by the capacitive force sensor and finally converted into a voltage signal with a capacitance readout circuit [15]. This system also requires linearization because the voltage-displacement mapping $H(u)$ of the thermal actuator is nonlinear (Fig. 5–6(C)). The virtual input is thus the displacement of the active arm, and the real input can be obtained via the inverse map of $H(u)$.

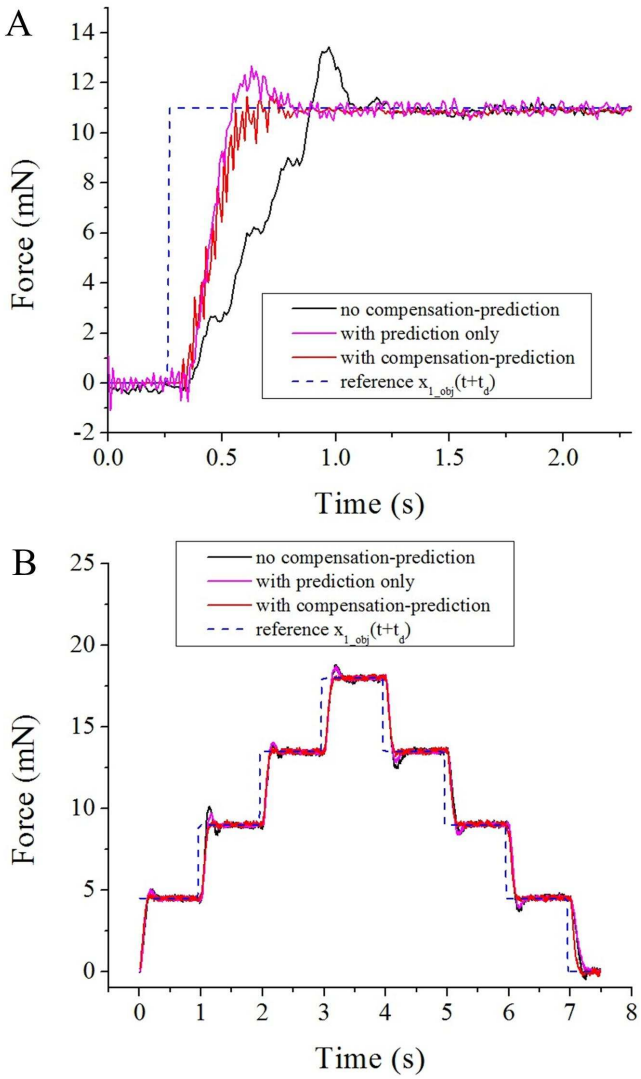

Figure 5–5: Experimental results of PID control of the robotic biosample stimulator with and without the compensation-prediction scheme. (A) Single step response. (B) Multi-step response.

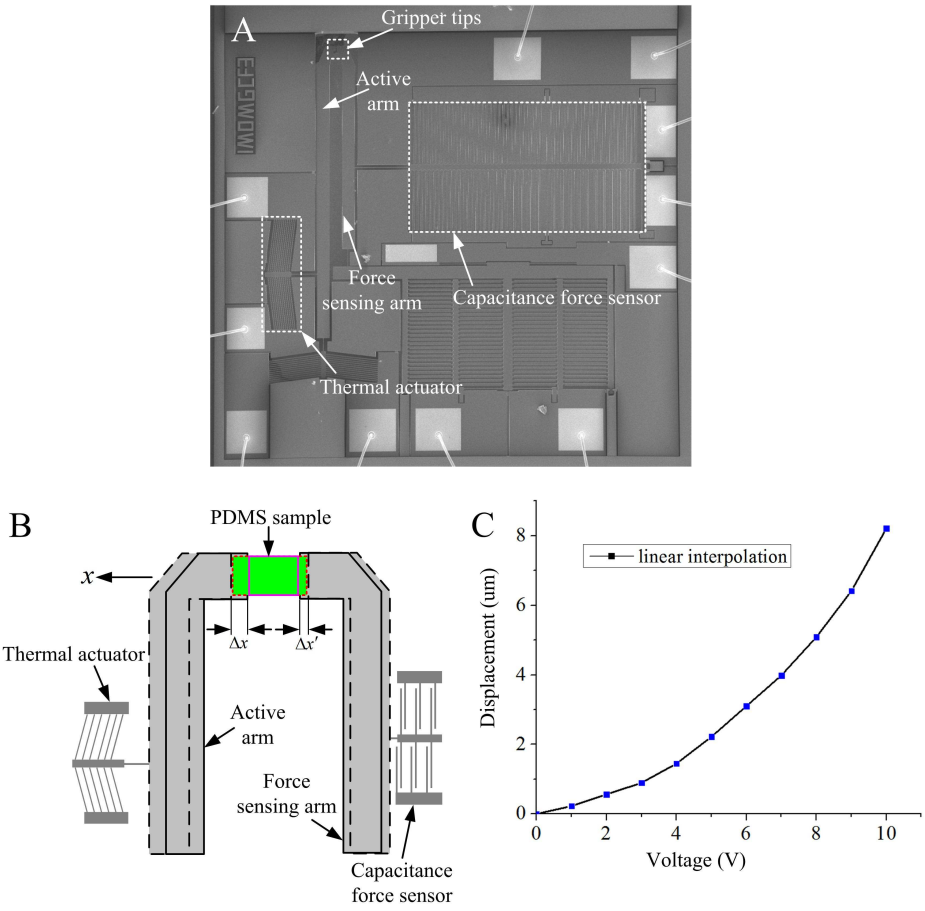

Figure 5–6: (A) Scanning electron microscopy (SEM) photograph of the microgripper. (B) Simplified schematic of the microgripper. (C) The calibration of the function $H(u)$, which describes the voltage-maximum displacement mapping of the movable arm.

Denote the deformation of the sample by x_{def}, the displacement of the force-sensing arm (due to the grasping force) by $\Delta x'$, and the gripping force by f, and the following relationship exists:

$$\begin{cases} x_{def} = \Delta x' - \Delta x \\ \dot{f} = -\frac{1}{\alpha} f + k\dot{x}_{def} \\ \dot{\Delta x} = \frac{1}{T_m} \left\{ H \left[u \left(t - t_d \right) \right] - \Delta x \right\} + \delta_2 \end{cases} \tag{5.24}$$

The second equation of (5.24) is the Maxwell viscoelastic model of PDMS, where k and α are parameters characterizing the viscoelastic property of the sample. The third equation is a time-delayed, first-order model governing the thermal actuator. Then, we converted (5.24) into the form of (5.1):

$$\begin{cases} \dot{f} = -\frac{1}{\alpha} f + \frac{k}{T_m} \Delta x - \frac{k}{T_m} H \left[u \left(t - t_d \right) \right] + \delta_1 \\ \dot{\Delta x} = \frac{1}{T_m} \left\{ H \left[u \left(t - t_d \right) \right] - \Delta x \right\} + \delta_2 \\ y = f + \xi \end{cases} \tag{5.25}$$

Note that $\Delta x'$ is much smaller than Δx; thus, the time derivative of $\Delta x'$ can be integrated into δ_1. The PDMS material parameters used for controller implementation are $\alpha = 0.3$ s and $k = 0.0225$ N/m, which are extracted from previous experiments [33]. Other parameters are estimated to be $T_m = 0.00075$ s and $t_d = 0.022$ s. The time constant (T_m) was estimated based on the experimental data in [28], and the time-delay (t_d) was obtained by conducting open-loop step input tests following the method in [13]. The system was first tuned without the compensation-prediction scheme to achieve the best possible result for single step response, and the final controller parameters were: $K_p = 1$, $K_I = 50$ and $K_d = 0$. These parameters were kept the same for the compensation-prediction and the prediction-only schemes. Fig. 5–7(A) shows the single-step responses of the controller with the three different schemes. A settling time of 0.3 s and an overshoot of 35% were achieved by the no- compensation-prediction scheme. In contrast, integrating the model compensation-prediction scheme yielded a much shorter settling time of 0.15 s (50% improvement vs. pure PID control) and a much smaller overshoot of 10% (71.4% improvement). Compared to the prediction-only scheme, the compensation-prediction scheme shows 14.1% improvement (0.15

Table 5–1: Comparison of results after the implementation of the compensation-prediction scheme.

Performance	No compensation-prediction	Prediction only	Compensation & prediction	Improvement	Rating
			Simulation		
Settling time	2.21 s	2.02 s	1.71 s	22.6% / 15.3%	
Overshoot	70%	52%	40%	42.9% / 23.1%	
IAE_d	5.96	5.44	4.86	15.6% / 10.6%	Medium/Medium/Medium
			Robotic biosample stimulator		
Settling time	0.8 s	0.39 s	0.3 s	62.5% / 23.1%	
Overshoot	27%	11%	5%	81.5% / 54.5%	
IAE_d	7.15	4.55	3.49	51.2% / 23.3%	Poor/Medium/Medium
			Microgripper		
Settling time	0.3 s	0.174 s	0.15 s	50% / 14.1%	
Overshoot	35%	18.41%	10%	71.4% / 45.7%	
IAE_d	5.59	1.76	1.49	73.3% / 15.3%	Medium/High/High

s vs. 0.174 s) in settling time and 45.7% improvement (10% vs. 18.4%) in overshoot. Fig. 5–7(B) shows the multi-step force control response of the control system with the compensation-prediction scheme, revealing similar improvements over the pure PID control.

Note that researchers have also developed microgrippers with on-chip actuation position sensors [23, 34]. However, integrating both actuation position sensors and force sensors on the same chip increases the complexity of the device microfabrication and readout circuit development, and many microgripper designs [3, 35] do not include actuation position sensors. Therefore, the control scheme presented in this work is still meaningful for controlling these sensorless microgrippers with improved performance.

5.7.3 Discussion

For time-delayed systems, the Smith predictor cannot be directly applied to them if they are time variant and have unknown terms. When the system was regulated with PID controllers, our simulation and experimental results showed that large overshoots are inevitable, especially in the case that short settling time is required. With the implementation of the compensation-prediction scheme, the control performance was significantly improved. However, compared with the prediction-only scheme, our propose scheme may not have advantage in terms of the settling time, but the overshoot could be deduced further. We quantitatively assessed the control performance of the three schemes (no-compensation-prediction, prediction only, and compensation-prediction) using a standardized index conceived for single step responses (denoted as IAE_d) [36]. A lower index indicates better control performance, and three levels of the control performance

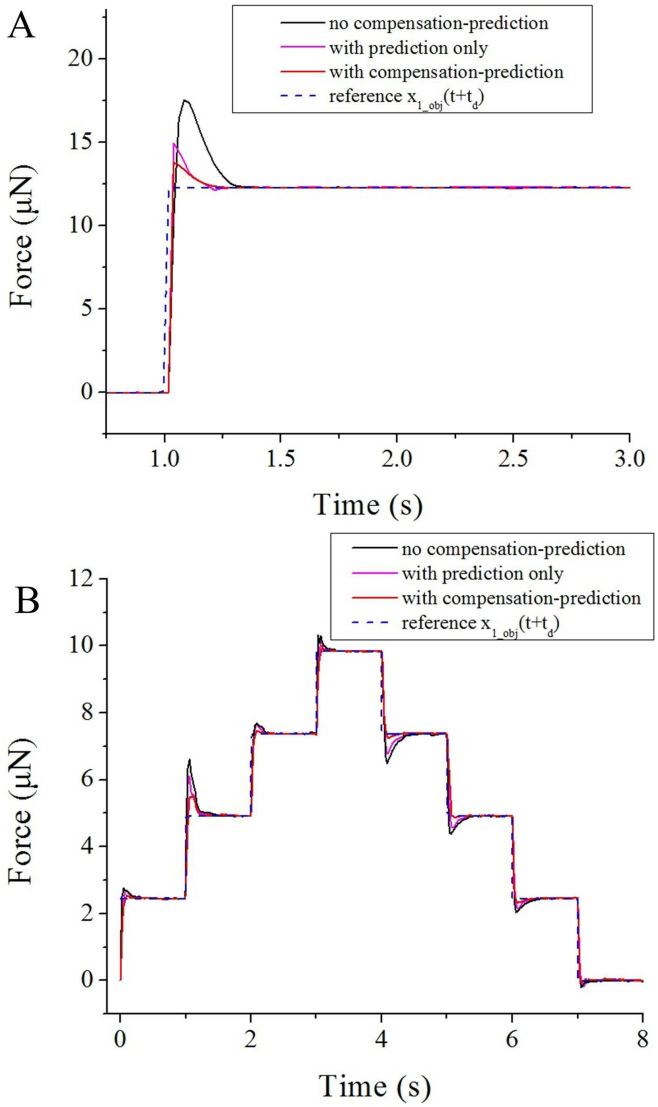

Figure 5–7: Experimental results of PID control a MEMS microgripper with and without the compensation-prediction scheme. (A) Single step response. (B) Multi-step response.

(i.e., poor, medium, and high) can be determined based on the index value. The performance comparison data for both the separate control parameters (settling time and overshoot) and the overall performance index are summarized in Table 5–1.

5.8 Conclusions

In this paper, we presented a new model compensation-prediction scheme for micromanipulation systems (which were described by unobservable 2D state-space models) with a first-order sensorless actuators, single force feedback loop, unknown modeling errors, feedback measurement noise, and time delays. This approach combined two modeling errors into one equivalent term, thus making the system observable by a noise-insensitive EHGO. The scheme removed the system unknown terms and enabled the implementation of a Smith predictor for time-delay prediction and compensation. Through the implementation of the proposed scheme on two typical micromanipulation systems, this method was proven to be effective in reducing the settling time and overshoot of the systems' step-input responses. The improvement of the control performance by the proposed scheme was finally quantified by a standardized control performance index.

References

[1] F. Arai, D. Andou, Y. Nonoda, T. Fukuda, H. Iwata, and K. Itoigawa, "Integrated microendeffector for micromanipulation," *IEEE/ASME Trans. Mechatron.*, vol. 3, no. 1, pp. 17–23, 1998, ISSN: 1083-4435. DOI: 10.1109/3516.662864.

[2] Y. Sun and B. J. Nelson, "Biological cell injection using an autonomous microrobotic system," *Int. J. Robot. Res.*, vol. 21, no. 10-11, pp. 861–868, 2002.

[3] K. Kim, X. Liu, Y. Zhang, and Y. Sun, "Nanonewton force-controlled manipulation of biological cells using a monolithic mems microgripper with two-axis force feedback," *J. Micromech. Microeng.*, vol. 18, no. 5, p. 055 013, 2008.

[4] D. Cappelleri, P. Cheng, J. Fink, B. Gavrea, and V. Kumar, "Automated assembly for mesoscale parts," *IEEE Trans. Autom. Sci. Eng.*, vol. 8, no. 3, pp. 598–613, 2011.

[5] X. Liu, R. Fernandes, M. Gertsenstein, A. Perumalsamy, I. Lai, M. Chi, K. H. Moley, E. Greenblatt, I. Jurisica, R. F. Casper, et al., "Automated microinjection of recombinant

bcl-x into mouse zygotes enhances embryo development," *PLoS ONE*, vol. 6, no. 7, e21687, 2011.

[6] J. Wason, J. Wen, J. Gorman, and N. Dagalakis, "Automated multiprobe microassembly using vision feedback," *IEEE Trans. Robot.*, vol. 28, no. 5, pp. 1090–1103, 2012.

[7] B. Komati, K. Rabenorosoa, C. Clévy, and P. Lutz, "Automated guiding task of a flexible micropart using a two-sensing-finger microgripper," *IEEE Trans. Autom. Sci. Eng.*, vol. 10, no. 3, pp. 515–524, 2013.

[8] S. Zimmermann, T. Tiemerding, and S. Fatikow, "Automated robotic manipulation of individual colloidal particles using vision-based control," *IEEE/ASME Trans. Mechatron.*, vol. 20, no. 5, pp. 2031–2038, 2015.

[9] M. Xie, Y. Wang, G. Feng, and D. Sun, "Automated pairing manipulation of biological cells with a robot-tweezers manipulation system," *IEEE/ASME Trans. Mechatron.*, vol. 20, no. 5, pp. 2242–2251, 2015.

[10] M. Mehrtash, X. Zhang, and M. Khamesee, "Bilateral magnetic micromanipulation using off-board force sensor," *IEEE/ASME Trans. Mechatron.*, vol. 20, no. 6, pp. 3223–3231, 2015.

[11] B. Tamadazte, N. Piat, and S. Dembélé, "Robotic micromanipulation and microassembly using monoview and multiscale visual servoing," *IEEE/ASME Trans. Mechatron.*, vol. 16, no. 2, pp. 277–287, 2011.

[12] W. Zhang, A. Sobolevski, B. Li, Y. Rao, and X. Liu, "An automated force-controlled robotic micromanipulation system for mechanotransduction studies of drosophila larvae," *IEEE Trans. Autom. Sci. Eng.*, vol. PP, no. 99, pp. 1–9, 2015, ISSN: 1545-5955. DOI: 10.1109/TASE.2015.2403393.

[13] G. Fedele, "A new method to estimate a first-order plus time delay model from step response," *J. Franklin Inst.*, vol. 346, no. 1, pp. 1–9, 2009.

[14] S. Khadraoui, M. Rakotondrabe, and P. Lutz, "Interval modeling and robust control of piezoelectric microactuators," *IEEE Trans. Control Syst. Technol.*, vol. 20, no. 2, pp. 486–494, 2012.

[15] J. Qu, W. Zhang, A. Jung, S. Sliva, and X. Liu, "A MEMS microgripper with two-axis actuators and force sensors for microscale mechanical characterization of soft materials," in *2015 IEEE International Conference on Automation Science and Engineering (CASE)*, 2015.

[16] P. Klan and R Gorez, "PI controller design for actuator preservation," in *Proceedings of the 17th IFAC World Congress*, 2008.

[17] C. Kravaris and R. A. Wright, "Deadtime compensation for nonlinear processes," *AIChE J.*, vol. 35, no. 9, pp. 1535–1542, 1989.

[18] B. Komati, M. R. Pac, I. Ranatunga, C. Clévy, D. O. Popa, and P. Lutz, "Explicit force control vs impedance control for micromanipulation," in *ASME 2013 International Design Engineering Technical Conferences and Computers and Information in Engineering Conference*, American Society of Mechanical Engineers, 2013, V001T09A018–V001T09A018.

[19] M. Boudaoud, Y. Le Gorrec, Y. Haddab, and P. Lutz, "Gain scheduling control of a nonlinear electrostatic microgripper: design by an eigenstructure assignment with an observer-based structure," *IEEE Trans. Control Syst. Technol.*, vol. 23, no. 4, pp. 1255–1267, 2015, ISSN: 1063-6536. DOI: 10.1109/TCST.2014.2362725.

[20] B. Komati, C. Clevy, and P. Lutz, "Force tracking impedance control with unknown environment at the microscale," in *2014 IEEE International Conference on Robotics and Automation (ICRA)*, 2014, pp. 5203–5208.

[21] M. Boudaoud, M. G. De Faria, Y. Haddab, S. Haliyo, Y. Le Gorrec, P. Lutz, and S. Régnier, "Robust microscale grasping using a self scheduled dynamic controller," in *World Congress*, vol. 19, 2014, pp. 7492–7498.

[22] Z. Chi, M. Jia, and Q. Xu, "Fuzzy pid feedback control of piezoelectric actuator with feedforward compensation," *Math. Probl. Eng.*, vol. 2014, 2014.

[23] Q. Xu, "Design and smooth position/force switching control of a miniature gripper for automated microhandling," *IEEE Trans. Ind. Informat.*, vol. 10, no. 2, pp. 1023–1032, 2014, ISSN: 1551-3203. DOI: 10.1109/TII.2013.2290895.

[24] M. Boukhnifer and A. Ferreira, "Passive bilateral control of teleoperators under time delay and scaling factors," in *44th IEEE Conference on Decision and Control, and 2005 European Control Conference (CDC-ECC '05)*, 2005, pp. 6972–6977.

[25] H. Dellas, "A real model of the world business cycle," *J. Int. Money Financ.*, vol. 5, no. 3, pp. 381–394, 1986.

[26] R. Zhang, Q. Quan, and K.-Y. Cai, "Attitude control of a quadrotor aircraft subject to a class of time-varying disturbances," *IET Control Theory A*, vol. 5, no. 9, pp. 1140–1146, 2011.

[27] R. Hickey, D. Sameoto, T. Hubbard, and M. Kujath, "Time and frequency response of two-arm micromachined thermal actuators," *J. Micromech. Microeng.*, vol. 13, no. 1, p. 40, 2003.

[28] H Sehr, I. S. Tomlin, B Huang, S. P. Beeby, A. G. R. Evans, A Brunnschweiler, G. J. Ensell, C. G. J. Schabmueller, and T. E. G. Niblock, "Time constant and lateral resonances of thermal vertical bimorph actuators," *J. Micromech. Microeng.*, vol. 12, no. 4, p. 410, 2002.

[29] W. Zhang, X. Dong, and X. Liu, "Switched fuzzy-pd control of contact forces in robotic micromanipulation of drosophila larvae," in *2015 IEEE International Conference on Robotics and Automation (ICRA)*, 2015.

[30] X. Wang, Z. Chen, and G. Yang, "Finite-time-convergent differentiator based on singular perturbation technique," *IEEE Trans. Automat. Contr.*, vol. 52, no. 9, pp. 1731–1737, 2007.

[31] W. Zhang, X. Dong, and X. Liu, "Switched fuzzy-pd control of contact forces in robotic micro-biomanipulation," *IEEE Trans. Biomed. Eng.*, vol. PP, no. 99, pp. 1–1, 2016.

[32] K. Åström and T Hägglund, "Revisiting the ziegler–nichols step response method for pid control," *J. Process Control*, vol. 14, no. 6, pp. 635–650, 2004.

[33] W. Zhang, X. Dong, S. S.-D. Cruz, H. K. Heris, L. G. Mongeau, A. J. Ehrlicher, and X. Liu, "A cost-effective microindentation system for soft material characterization," in *2015 IEEE International Conference on Mechatronics and Automation (ICMA)*, 2015, pp. 825–830. DOI: 10.1109/ICMA.2015.7237592.

[34] B. Piriyanont, A. G. Fowler, and S. Reza Moheimani, "Force-controlled mems rotary microgripper," *J. Microelectromech. Syst.*, vol. 24, no. 4, pp. 1164–1172, 2015.

[35] K. Kim, E. Nilsen, T. Huang, A. Kim, M. Ellis, G. Skidmore, and J.-B. Lee, "Metallic microgripper with su-8 adaptor as end-effectors for heterogeneous micro/nano assembly applications," *?Microsys. Technol.*, vol. 10, no. 10, pp. 689–693, 2004, ISSN: 1432-1858. DOI: 10.1007/s00542-004-0367-6. [Online]. Available: http://dx.doi.org/10.1007/s00542-004-0367-6.

[36] A. Yepes, A. Vidal, O. Lopez, and J. Doval-Gandoy, "Evaluation of techniques for cross-coupling decoupling between orthogonal axes in double synchronous reference frame current control," *IEEE Tran. Ind. Electron.*, vol. 61, no. 7, pp. 3527–3531, 2014, ISSN: 0278-0046. DOI: 10.1109/TIE.2013.2281160.

The connection between Chapter 5 and Chapter 6

In Chapters 4 and 5, the improvement of force control performance of the micromanipulation system were achieved through two different ways. In Chapter 4 an advanced controller was adopted without modifying the control scheme, while in Chapter 5 a new compensation-prediction control scheme was utilized in combination with a conventional PID controller. The objective of Chapter 6 are two fold. On one hand, I will combine the switched fuzzy-PD controller with the advanced compensation-prediction scheme to achieve even better force control performance. On the other hand, I will use the final force control system to performance biological experiments and quantify, for the first time, the relationship between the touch force level and the transmission signal intensity of Class III ddaA neurons in *Drosophila* larvae.

CHAPTER 6
Quantifying the Relationship between Touch Force and Signal Transmission of Class III ddaA Neurons in *Drosophila* Larvae

Quantifying the Relationship between Touch Force and Signal Transmission of Class III ddaA Neurons in *Drosophila* Larvae

Weize Zhang, Yixu Chen, Yong Rao, and Xinyu Liu*

Department of Mechanical Engineering, McGill University, 817 Sherbrooke Street West, Montreal, Quebec H3A 0C3, Canada

*Corresponding author: xinyu.liu@mcgill.ca.

To be submitted.

The responses of stimuli of *Drosophila* larvae have drawn increasing interacts from researchers because it is a good representative of creatures' danger-escaping behaviors. By applying mechanical stimuli and studying the mechanotransduction under microscope, the fluorescence intensity of Class III ddaA neurons of certain genotypes have been demonstrated to have strong correlation with the mechanical stimulation. However, these experiments were performed under a fixed force level, and the force measurement approaches introduced relatively large errors. It is intuitive to assume that there exists a quantitative relationship between the touch force level and the calcium fluorescence intensity of the class III ddaA neurons. However, due to the lack of capability of accurate force control in previous experimental setup, this relationship has not been quantified. In this paper, we present a robotic mciromanipulation system which is capable of applying closed-loop force-controlled mechanical stimuli to *Drosophila* larvae and fluorescence image recording. we combined two of our previous works together and obtained a compensation-prediction+switched fuzzy-PID control architecture, which demonstrates a settling time of 0.15 s, no overshoot and a resolution better than 0.05 mN. By applying mechanical stimuli ranging from 0.25 mN-2 mN, we obtained, for the first time, the quantitative relationship between the applied force level and the change in calcium fluorescence signal. The threshold force level at which the neuron starts to

get activated was determined to be 0.3 mN. This work may contribute to new findings on sensory mechanotransduction in Drosophila larvae.

Index Terms-Robotic micromanipulation, Closed-loop, Control architecture, Calcium fluorescence imaging, Quantitative correlation.

6.1 Introduction

The sense of stimuli is the basis of danger-escaping behaviors and is critical for a creature to survive. *Drosophila* larva is a common biological model for studying mechanisms of sensory neurons responsive to external stimulation. For instance, a *Drosophila* larva tends to turn/roll at the presence of a touch stimulus [1, 2, 3]. Increasing interests arise in larval sensory mechanotransduction and the underlying neuronal mechanisms. Even though functions of most neuron types found in the *Drosophila* larval body walls remain unexplored [3], it has been investigated that Class I to IV neurons are nociceptive and related to larval locomotion, among which the Class III md neurons contribute to the larval response to gentle touches and can be activated by a touch force [3].

Calcium ions generate versatile intracellular signals that control key functions in all types of neurons [4], which makes the neuronal calcium signal a good indictor of neuron activities. Calcium fluorescence intensity of a variety of neurons of *Drosophila* larvae can be influenced by environmental stimulation [2, 5, 6, 7], among which the fluorescence intensity of Class III ddaA neurons of certain genotypes have been demonstrated to have strong correlation with the mechanical stimulation [3]. One straightforward method to investigate this correlation is to visualize the change in fluorescence intensity at presence of mechanical stimuli under microscope. Previous studies have confirmed this phenomenon with a constant force applied to the larval body. In [3, 8], experiments were performed at the force level of 1 mN. The time history of fluorescence intensity of the neuronal calcium signal was provided in [3]. The neuron that shows significant change in fluorescence intensity has been identified to be Class III ddaA [3]. Even though the selected *Drosophila* larvae are of a specific genotype, their locomotion behavior at the presence mechanical stimuli (danger-escaping behavior) shows no difference compared to that of non-mutated larvae [3, 2, 8], which makes them good representative of ordinary *Drosophila* larvae.

Despite the promising results previously obtained, these experiments were performed under a fixed force level, and the force measurement approaches (e.g., by visually measuring the deflection of an eyelash) introduced relatively large errors. In addition, it is intuitive to speculate that

there exists a quantitative relationship between the touch force level and the calcium fluorescence intensity of the class III ddaA neurons; however, due to the lack of capability of accurate force control in previous experimental setup, this relationship has not been quantified. We have developed a force-controlled robotic micromanipulation system capable of simultaneous mechanical stimulation and calcium fluorescence imaging of *Drosophila* larvae [9], and also proposed new force control approaches for improving the system's force control performance [10, 11].

Controlling the touch force applied to a *Drosophila* larva is a challenging task. Main difficulties of touch force control include modeling error, measurement noise, time delay and insufficient feedback. In [10], we developed a switched fuzzy to proportional-derivative (PD) controller without considering the dynamics of the micromanipulator, which demonstrated fast convergence speed and reduced steady state oscillation. The fuzzy controller is not model dependant, but the PD controller is. Ignoring the dynamics of the micromanipulator has an negative impact on the system performance after the switch to PD control. Therefore, it is intuitive to further improve the performance by considering manipulator dynamics. In [11], we tried to account for the micromanipulator dynamics and tackled the associated new challenge: since an additional state vector is added to the system, the single force feedback is insufficient to make the system observable. Coupled with other problems, including modeling error, measurement noise and time delay, a new control scheme is needed to solves these problems altogether. We proposed a compensation-prediction scheme [11] and tested it with a conventional proportional-integral-derivative (PID) controller. With the proposed scheme implemented, the overshoot and settling time of the system's step response were both reduced. In this paper, we will combine our previous work to form a compensation-prediction control architecture with a switched fuzzy-PID controller. This approach combines the advantage of both control methods previously developed and will further improve the system control performance.

Remark: The result of combining switched fuzzy-PD controller and compensation-prediction control scheme is compensation-prediction+switched fuzzy-PID (instead of PD) control architecture, because in [11], a PID (instead of PD) controller was optimized for compensation-prediction scheme.

Here, we report a force-controlled robotic micromanipulation system with an advanced force control architecture and apply the system to quantifying the relationship between the touch force applied to a *Drosophila* larva and the larva's transmission signal in its Class III ddaA neurons. The force control architecture combines the compensation-prediction scheme and the switched fuzzy-PID control. Biological experiments are performed to visualize and record the change in calcium fluorescence intensity of Class III ddaA neuron at different force levels. We obtained, for the first time, the quantitative relationship between the relative change in calcium fluorescence intensity of Class III ddaA neurons and the touch force level applied to the larva, and determined the minimum force level at which the Class III ddaA neurons of a *Drosophila* larva start to respond.

6.2 System Setup and Operation Procedure

6.2.1 System Components

The experimental setup of the robotic micromanipulation system is shown in Fig. 6–1(A). An inverted microscope (BX61W1, Olympus) is used with 4X, 10X and 20X objectives, and could switch between different objectives with a motorized turret. A high-speed fluorescence camera (Zyla, Andor) is mounted to the end of an optical spitter (OPTALSPLIT II, Cairn). The camera is capable of capturing fluorescence images with satisfying quality (clear enough to observe ddaA neurons) at eight frames per second. The optical splitter is employed to split two components of recorded images at specific emission wavelength and thus acquire GFP (509 nm) and RFP (583 nm) fluorescence signals emitted from the same neuron simultaneously. Since the larva samples are immobilized and flattened (immobilized body thickness: 130 m) with PDMS devices [10], most of the neurons are largely in the horizontal plane of the substrate. The larvae are placed on a motorized stage, whose horizontal movement could be controlled via keyboard input. A glass pipette is glued onto a piezoresistive force sensor (AE801, SensorOne). The pipette-sensor assembly

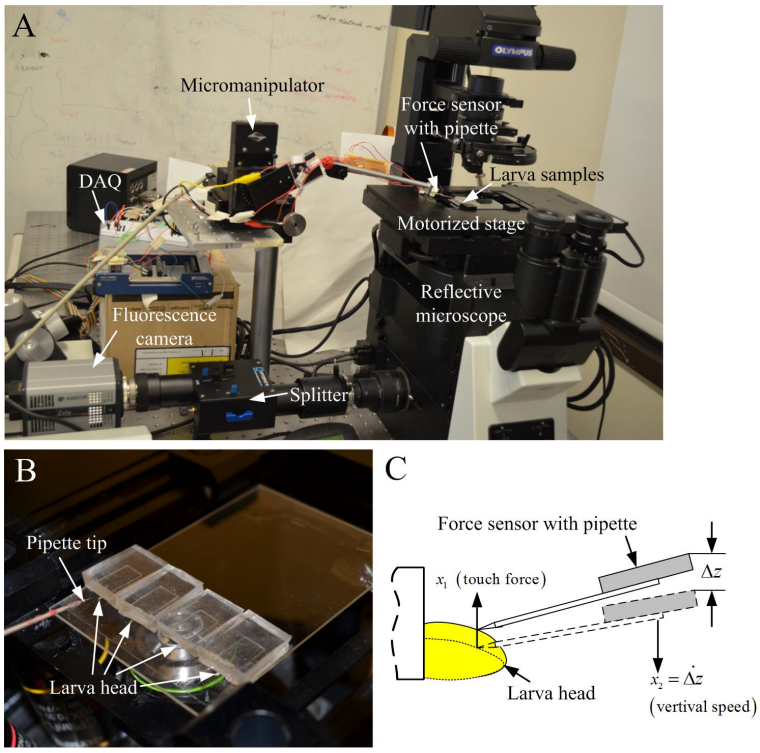

Figure 6–1: (A) Experimental setup of the micromanipulation system. (B) Zoomed-in photograph of four larva samples immobilized by PDMS devices. (C) Schematic of the control system model.

is attached to an iron rod, which is fixed onto a micromanipulator (MP-285, Sutter Insturments). The force data is read with a home-made Wheatstone bridge circuit, and is acquired with a data acquisition board (USB 6343, National Instruments).

Fig. 6–3(B) is the photograph of four immobilized larvae and the glass pipette. Larvae are immobilized by the PDMS devices with only heads exposed for touch stimulation. Fig. 6–3(C) is the schematic of a simplified mechanical model of lava touching with the assumption of linear elasticity of the larva body.

6.2.2 System Operation Procedure

Compared to the system reported in our previous work [12], this system employs an inverted microscope and a faster and more sensitive fluorescence camera to quantify the calcium fluorescence signals from single neuron cells, and to record fluorescence images at a higher frame rate. Note that the stimulation of a single neuron cell requires that the pipette tip and the neuron are in the same field of view under 20× magnification [3]. Thus, we must stimulate and observe neuron cells immobilized within the PDMS device but close to the device side wall (see Fig. 6–2(B)). In our previous setup [12], the automated operations were performed under a 4× objective and cannot quantify fluorescence signal of a single neuron with satisfactory resolution. Therefore, in this work we operate the system through teleoperation by a user on a computer screen. The system allows an operator to perform all the operations under a 20× objective via keyboard inputs.

Fig. 6–2 illustrates major steps of the system teleoperation. Once an experiment begins, the first step is to move the correct neuron to the field of view under fluorescence mode (20× magnification), as shown in Fig. 6–2(B). Then the system switches to bright-field mode (Fig. 6–2(C)) and the operator moves the pipette tip to the vicinity of the neuron via keyboard control (Fig. 6–2(D)). Note that the pipette tip is not very clear but still discernible (indicated by the dashed lines in 6–2(C)(D)). After that, the system switches back to the fluorescence mode, and a closed-loop controlled touch force is applied to the larva and the fluorescence images recorded simultaneously. A user can perform all these steps through keyboard inputs, and do not need to leave the computer screen.

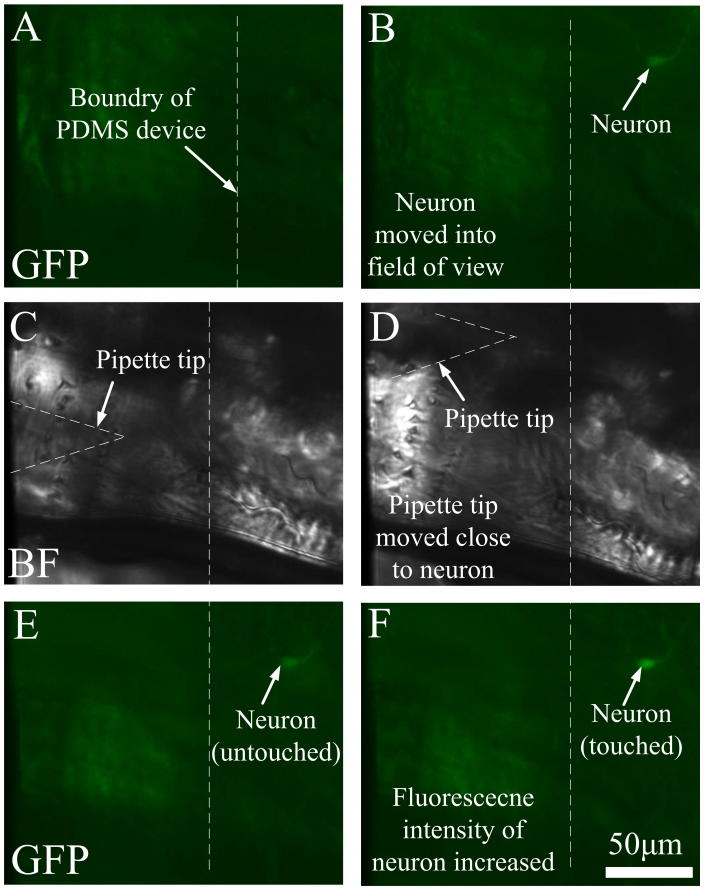

Figure 6–2: System operation steps. (A) to (B): A neuron is moved into field of view under the fluorescence mode. (B)(C) The pipette tip is moved to the vicinity of the neuron under the bright field mode. (C) Closed-loop controlled touch stimulus is applied and the fluorescence images of the neuron are recorded.

One reason for having these specific operation steps is that the non-fluorescent pipette tip is not observable in the fluorescence mode. To make sure the pipette tip and the neuron are both in the same field of view under 20× magnification, the system switches to the bright field mode (from Figs. 6–2(B) to 6–2(C)) to visualize the pipette tip and to make sure it does not contact the PDMS device boundary (which is still in the imaging field and indicated by the vertical dashed line in Fig. 6–2). The pipette tip is blocked by larval body and is out of focus, making its image blurred but still visible in the bright field mode. We can see that the pipette tip is on the left side of the PDMS device boundary, which does not contact the PDMS device and could be moved freely. The neuron is on the right side of the PDMS device boundary, which is immobilized inside the PDMS device.

6.3 Closed Loop Force Control

6.3.1 System Modeling

The control architecture is the combination of the compensation-prediction scheme and the fuzzy-PID controller, both have been presented in our previous work [10, 11]. To make this paper self-contained, we briefly introduce the combined control architecture of the robotic micromanipulation system. The system is modeled as a two-dimensional (2D) state-space model:

$$\begin{cases} \dot{x}_1 = Kx_2 + \delta_1 \\ \dot{x}_2 = \frac{1}{T_m}\left\{H\left[u\left(t - t_d\right)\right] - x_2\right\} + \delta_2 \\ y = x_1 + \xi \end{cases} \tag{6.1}$$

The variables x_1 and x_2 are the contact force (the variable to be controlled) and the vertical speed of the micromanipulator, respectively, as shown in Fig. 6–1(C). The first equation is the time derivative of a linear spring touch model [10, 11], where K is the spring constant. The second equation is a time-delayed first-order dynamic model of the micromanipulator, where T_m is the time constant of the first-order dynamic model, and the function $H(u)$ is the calibrated mapping of maximum z-axis speed vs. input voltage of the micromanipulator [11]. The parameters were experimentally determined to be $K = 200$ N/m, $T_m = 0.01$ s, and $t_d = 0.05$ s [11].

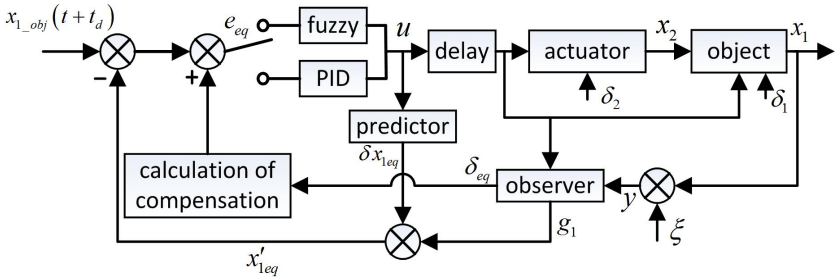

Figure 6–3: Control system architecture.

6.3.2 Control Flow Overview

The force control architecture is the combination of the compensation-prediction scheme [11] and the switched fuzzy-PID controller [10], which is effective to treat problems with measurement noise, time delay, modeling error and insufficient feedback. As shown in Fig. 6–3, the z-axis of the micromanipulator could be treated as a first order actuator. The system is time delayed by t_d due to the dynamics of the micromanipulator and other delay times of the system (e.g., the delay of command transmission and the mechanical backlash). The system output is x_1, and its objective (reference) value is denoted by x_{1_obj}. Note that only step inputs are used for control performance validation, as they mimic sudden mechanical stimuli applied to the larva [3, 8].

The tracking error of x_1 is denoted by $e_1(t) = x_{1\_obj}(t + t_d) - x_1(t)$. Note that we use $x_{1\_obj}(t+t_d)$ instead of $x_{1\_obj}(t)$ as reference to highlight the fact that the time-delayed system will always respond to an step input with a time delay of t_d. The system has two unknown modeling errors (δ_1 and δ_2) in the two differential equations of the 2D state-space model Eq. 6.1. These errors are supposed to be time-varying. To make the system observable from the single force feedback loop, we combine them into an equivalent modeling error (δ_{eq}) through mathematical transformation, and then estimate δ_{eq} using a modified EHGO insenstive to the force measurement noise (ξ). The EHGO also provides a denoised value (g_1) of the force measurement y. A Smith predictor is implemented to calculate a correction (δx_{1eq}) to the tracking error caused by the system time delay. Based on the estimation (δ_{eq}) of the equivalent modeling error, a compensation is added to further correct the tracking error, and the corrected error (e_{eq}) is then injected into a

controller to calculate the control input u. The selection of controller is summarized as follows: once the force command is set, the system employs the fuzzy controller first to take advantage of its fast converging speed. Since the fuzzy controller is not model dependant, it does not need any modification compared to [10]. Once the tracking error reaches a threshold of 13.6% [10], the system switches to PID controller with optimized PID paramters ($K_p = 150$, $K_I = 200$ and $K_d = 2$) [11] under compensation-prediction scheme.

Important equations are summarized as follows. For simplicity, we mark $\upsilon(t) = H[u(t)]$. First of all, a noise-insensitive EHGO [11] is adopted to calculate an equivalent modeling error δ_{eq} and an estimation of the time-derivative of x_1:

$$\begin{cases} \dot{\hat{x}}_1 = K\hat{x}_{2eq} + \hat{\delta}_{eq} - \frac{k_1}{\varepsilon}(\hat{x}_1 - g_1) \\ \dot{\hat{x}}_{2eq} = \frac{1}{T_m}[\upsilon(t - t_d) - \hat{x}_{2eq}] - \frac{k_2}{\varepsilon^2}(\hat{x}_1 - g_1) \\ \dot{\hat{\delta}}_{eq} = -\frac{k_3}{\varepsilon^3}(\hat{x}_1 - g_1) \\ \dot{g}_1 = g_2 \\ \dot{g}_2 = g_3 \\ \dot{g}_3 = \frac{1}{\alpha^3} h(g_1 - y, \alpha g_2, \alpha^2 g_3) \end{cases} \tag{6.2}$$

The parameters are $k_1 = 50$, $k_2 = 1000$, $\varepsilon = 0.1$ and $\alpha = 0.04$ [11]. $h(x)$ used in this research is [13]:

$$\begin{aligned} h(g_1 - y, \alpha g_2, \alpha^2 g_3) &= -4 \cdot 2^{\frac{3}{5}} \left(g_1 - y + (\alpha g_2)^{\frac{9}{7}}\right)^{\frac{1}{3}} \\ &\quad - 4 \cdot \left(\alpha^2 g_3\right)^{\frac{3}{5}} \end{aligned} \tag{6.3}$$

Then a traditional Smith predictor is implemented as if the system is devoid of modeling errors [11]:

$$\begin{cases} \dot{\hat{x}}_{1eq\_f} = a\hat{x}_{1eq\_f} + b\hat{x}_{2eq\_f} + cu \\ \dot{\hat{x}}_{2eq\_f} = \frac{1}{T_m}(\upsilon - \hat{x}_{2eq\_f}) \end{cases} \tag{6.4}$$

$$\begin{cases} \dot{\hat{x}}_{1eq} = a\hat{x}_{1eq} + b\hat{x}_{2eq} + cu(t - t_d) \\ \dot{\hat{x}}_{2eq} = \frac{1}{T_m}\left[\upsilon(t - t_d) - \hat{x}_{2eq}\right] \end{cases} \tag{6.5}$$

$$\delta x_{1eq} = \hat{x}_{1eq\_f} - \hat{x}_{1eq} \tag{6.6}$$

where $\hat{x}_{1eq}$ and $\hat{x}_{1eq\_f}$ are the estimations of x_{1eq} with and without dead time. The term δx_{1eq} is a traditional Smith predictor correction. A conventional tracking error with Smith predictor correction is

$$e_{eq} = x_{1\_obj} - (x_1 + \delta x_{1eq}) \tag{6.7}$$

However, given the presence of modeling error, a compensation-prediction scheme is adopted to further rectify e_{eq}. According to the discussion in [11], the compensation-prediction scheme is equivalent to implementing a Smith predictor as if we had the precise model, except for adding a supplementary correction of $e^{at}\int_0^t \delta_{eq} e^{-a\tau} d\tau - e^{a(t+t_d)}\int_0^{t+t_d} \delta_{eq} e^{-a\tau} d\tau$ to compensate for the modeling error (which corresponds to the "calculation of compensation" block in Fig. 6–3). The tracking error injected into the controller is:

$$\begin{aligned} e_{eq} =& x_{1\_obj} - (x_1 + \delta x_{1eq}) \\ &+ e^{at}\int_0^t \delta_{eq} e^{-a\tau} d\tau - e^{a(t+t_d)}\int_0^{t+t_d} \delta_{eq} e^{-a\tau} d\tau \end{aligned} \tag{6.8}$$

This concludes the compensation-prediction scheme. It treats modeling error, time delay, measurement noise and insufficient feedback altogether. The next step is to inject the equivalent tracking error e_{eq} into an appropriate controller. Two candidate controllers could be chosen from: the fuzzy controller and the PID controller. These two controllers are summarized as follows:

When e_{eq} is higher than a threshold set by user [10], e_{eq} and its time-derivative $\dot{e}_{eq}$ (calculated with the method described in [11]) are evaluated with a fuzzy logic lookup table, from "positive big" (PB) to "negative big" (NB). Then a fuzzy control input is derived from the lookup table consisting 56 control rules [10]:

$$\bar{\upsilon}(\tau) = \bar{\upsilon}_1(\tau) + \bar{\upsilon}_2(\tau) + \bar{\upsilon}_3(\tau) + \cdots + \bar{\upsilon}_{56}(\tau) \tag{6.9}$$

Finally, a numerical control input is calculated from centroid defuzzification method [10]:

$$\upsilon = \upsilon_F = \frac{\int_{-6}^{6} \bar{\upsilon}(\tau)\tau d\tau}{\int_{-6}^{6} \bar{\upsilon}(\tau) d\tau} \tag{6.10}$$

When e_{eq} is inferior to the threshold, a conventional PID controller is used, whose parameters are inherited from [11]:

$$\upsilon = \upsilon_{PID} = K_p e_{eq} + K_I \int e_{eq} dt + K_d \dot{e}_{eq} \tag{6.11}$$

Note that υ is virtual input due to the nonlinear relationship between the real input u and the maximum vertical speed $H(u)$. The real input u is derived from an inversion $u = H^{-1}(\upsilon)$.

6.4 Experimental Methods

6.4.1 Larvae Preparation

NOMPC (No mechanoreceptor potential C) is a mechanotransduction channel subunit for gentle-touch sensation [8], and Class III ddaA dendritic arborization neurons function in gentle-touch sensation. 3rd instar *Drosophila* larvae are larvae close sexual maturity. Their size, shape and neuron network make them ideal test subjects for mechanotransduction studies [14, 15, 16, 17]. We chose 3rd instar $nompC^1/nompC^3$, UAS-*nompC*/CyO, weep; GAL4 [19-12]/UAS-GCaMP6 (nompC rescue) as the genotype of the experimental group, and 3rd instar GAL4 [19-12]/UAS-GCaMP6 as the control group [8]. The notation of genotype is defined as the location and the identifier of the inserted gene. For instance, GAL4 [19-12]/UAS-GCaMP6 signifies the GAL4 gene at the cytological location 19-12 that encodes the yeast transcription activator protein GAL4, and the UAS (Upstream Activation Sequence) is an enhancer to which GAL4 specifically binds to activate gene transcription. GCaMP6 is an ultrasensitive protein calcium sensor. Note that we used GCaMP6 instead of the GCaMP5 marker in [8] due to a recent upgrade of marker of our supplier.

The larvae preparation procedure is summarized as follows. Original larvae lines were provided by Younger S of UCSF School of Medicine. These larvae lines were in four genotypes:

1. $nompC^3$, UAS-*nompC*; Gal4[19-12]

2. *nompC*^{1}/CyO,weep; UAS-GCaMP5
3. GAL4 [19-12]
4. UAS-GCaMP5

To get a desired genotype, line 1 and line 2 were crossed for experimental group, and line 3 and line 4 were crossed for control group.

Original larvae lines were raised in *Drosophila* agar with apple juice under room temperature. The number of eggs were limited to less than 200 per dish. It took about 11-12 days for the eggs to go through embryo, 1st-3rd instar larva, pupa stage, and eventually adults emerged from the pupa cases. Immediately after the Eclosion, virgin larvae were picked out for crossing to minimize the possibility of mutated gene. The offsprings were kept in the same *Drosophila* agar.

6.4.2 Experimental procedure

For simplicity of the description, the term "applying mechanical stimuli" is defined as touching the imaging field of the neuron for 1 s [3]. The experiment was designed to be three steps.

First of all, select one Class III ddaA neuron of a drosophila larva of the experimental group. Apply mechanical stimuli of 1 mN for 5 times and observe the changes in fluorescence intensity of the neuron. This is to verify that the response to touch is repetitive, and each experiment is independent.

Secondly, apply mechanical stimuli of 2 mN, 1 mN, 0.5 mN and 0.25 mN to larvae from the experimental group. Each force level is applied for 30 times on 3 larvae (2 neurons per larva, 5 times of stimulation per force level, and thus 10 sets of fluorescence signal data per larva). This is to quantify the fluorescence response of neurons under different force levels, and to find a threshold under which no significant fluorescence response is displayed (the threshold force level to activate the Class III ddaA neuron).

Finally, apply mechanical stimuli of 2 mN to control group. This experiment is also performed for 30 times. This is to verify that the control group is unable to display significant change in fluorescence intensity even under the highest force level.

The interval between each stimulus was > 10 s, which is long enough to allow the larva to completely recover from each stimulation.

After each stimulus, fluorescence image frames of the neuron are collected. Fluorescence intensity is measured by calculating the average grayscale value within a 5 μm $\times$ 5 μm block that contains the brightest part of the neuron, as shown in Fig. 6–6. Suppose the intensities of RFP and GFP are F_{rfp} and F_{gfp} respectively. Using F_{rfp} as reference, the normalized intensity F_n is defined as:

$$F_n = \frac{F_{gfp}}{F_{rfp}} \tag{6.12}$$

The relative increment $\frac{\Delta F_n}{F_n}$ is defined as the indicator of neuron response to mechanical stimuli.

6.5 Experimental Results

6.5.1 Validation of Force Control Performance

To demonstrate the advantage of this combined control architecture, the step-response data of three different control architectures are compared. Note that the data of switched fuzzy-PD controller is not the same as these from the experiment in [10] as new noise-attenuation methods (e.g., electromagnetic shielding and force sensor signal amplification) were implemented [11]. To make the results more comparable, we performed all the experiments with same noise-attenuation conditions, and the results are shown in Fig. 6–4. By comparing the performance of the PID controller with the compensation-prediction scheme with that of the switched fuzzy-PD controller, one can clearly see the advantage of the fuzzy controller: the logic of the fuzzy controller always tries to converge at its maximum speed [10], resulting in shorter raising time and shorter settling time. However, the performance of switched fuzzy-PD controller still has room to improve after the switch from fuzzy to PD control, because when the control loop becomes model-dependent after the switch, a more accurate model with smaller modeling errors allows the observer to provide faster estimation [11]. Combining the compensation-prediction+PID scheme with the fuzzy controller to form a complete compensation-prediction switched fuzzy-PID scheme, the settling time is as short

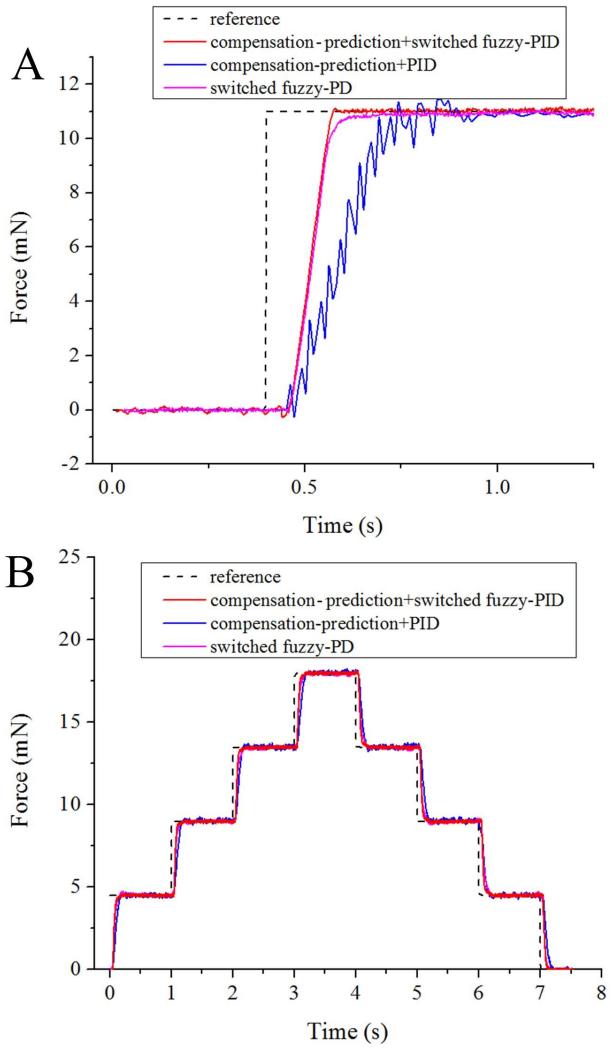

Figure 6–4: Comparison of force control results from three control architectures. By combing two the compensation-prediction scheme and the switched fuzzy-PID controller, the system inherits the fast convergence characteristic of fuzzy controller before reaching the switching threshold, and converge faster than the PD controller after reaching the switching threshold. (A) Single step response. (B) Multi-step response.

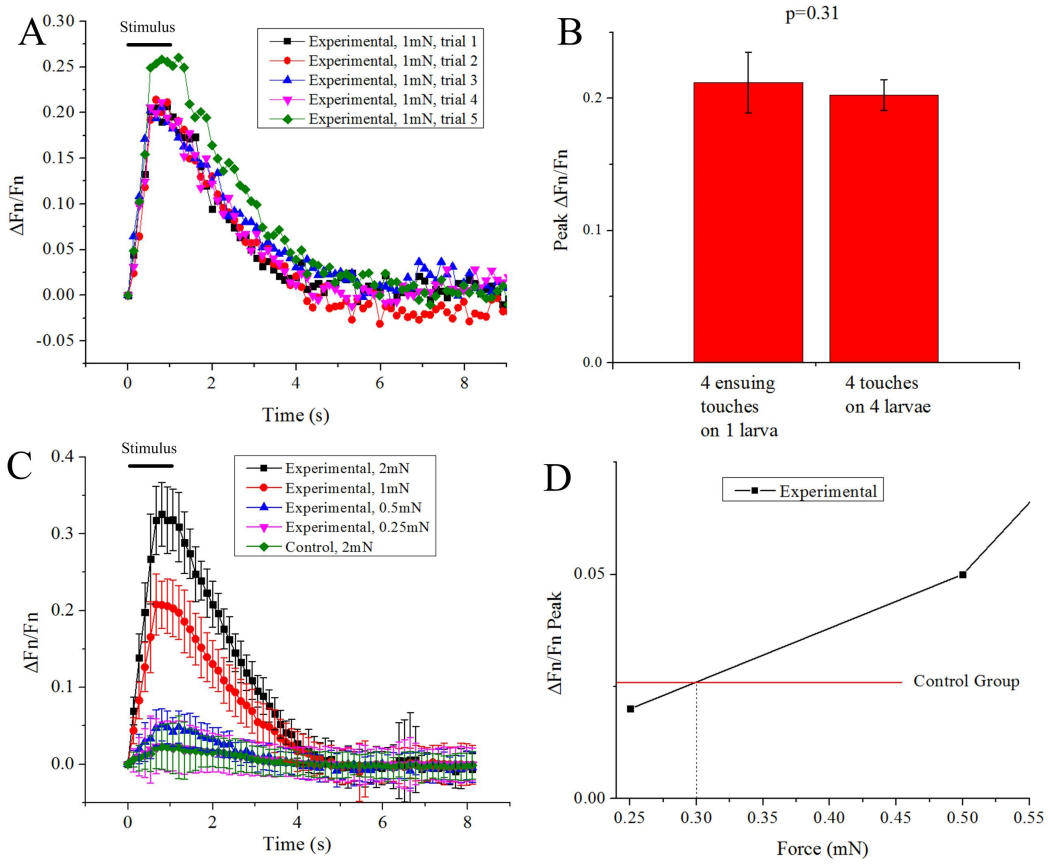

Figure 6–5: (A) Comparison of responses to 1 mN mechanical stimuli 5 times on the same Class III ddaA neuron. (B) Student's-t test of ensuing touches and single touches. No significant difference is found. (C) Comparison of responses to mechanical stimuli of different force levels. Each stimulus is applied 30 times. (D) Linear interpolation of the peak $\frac{\Delta F_n}{F_n}$ between 0.25 mN and 0.5 mN of experimental group. It intersects with the peak $\frac{\Delta F_n}{F_n}$ of control group at 0.3 mN.

as 0.15 s without overshoot, and the force control resolution is lower than 0.05 mN. Compared to the switched fuzzy-PD controller, our proposed architecture has the same initial convergence speed, but converges faster after the controller switch, which could be attributed to the compensation-prediction scheme. Compared to the compensation-prediction scheme with a PID controller, our proposed architecture displays faster initial convergence speed due to the fuzzy controller.

6.5.2 Independence of Neuronal Response to Repeated Stimuli

To illustrate that the response of each mechanical stimulus is independent, one Class III ddaA neuron of a *Drosophila* larva from the experimental group was selected. A mechanical stimulus of 1 mN was applied for 5 times with a time interval of at least 1 min between each touch, resulting in

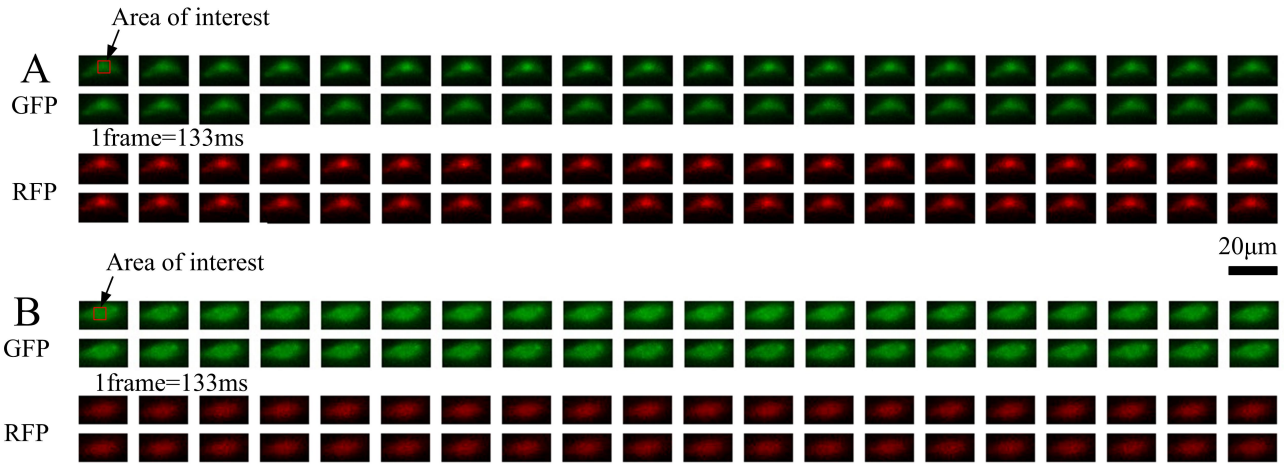

Figure 6–6: GFP ans RFP image stacks of a Class III ddaA neuron of experimental group (A) and those of control group (B).

4 ensuing touches. The relative increment in normalized fluorescence intensity ($\frac{\Delta F_n}{F_n}$) of the Class III ddaA neuron is plotted in Fig. 6–5(A). To demonstrate that the 4 ensuing consecutive touches have no significant difference with the first touch, a Student's-t test was conducted to compare the peak $\frac{\Delta F_n}{F_n}$ response of the 4 consecutive touches and that of 4 singles touches, as shown in Fig. 6–5(B). The p value is determined to be 0.31, which is much higher than the threshold ($p = 0.05$) to reject the hypothesis that the difference is considered to be statistically significant. Therefore, the independence of the neuron's response to repeated stimuli is confirmed.

6.5.3 Responses to Stimuli of Different Force Levels

The response of Class III ddaA neurons to mechanical stimuli at different levels are plotted in Fig. 6–5(C). For the experimental group, the peak of $\frac{\Delta F_n}{F_n}$ in response to 2 mN, 1 mN, 0.5 mN and 0.25 mN are 32.2%, 21.4%, 5.1% and 2.4%, respectively. For the control group, the peak of $\frac{\Delta F_n}{F_n}$ for 2 mN stimuli is 2.55%, which is much lower than that of the experimental group at 2 mN. To determine the minimum force level at which the neuronal fluorescence signal starts to respond, we used linear interpolation of the peak values of $\frac{\Delta F_n}{F_n}$ between 0.25 mN and 0.5 mN of the experimental group, and analyzed its intersection with the peak value of the control group. The horizontal coordinate of the intersection is 0.3 mN, which indicates the minimum force level required.

6.6 Discussion

The proposed force control architecture combines the advantages of the fuzzy controller (fast convergence before reaching the threshold) and the compensation-prediction scheme (capability of handling force measurement noise, modeling error, time delay, and insufficient feedback modality). The achieved high force control performance allowed the robotic micromanipulation system to replicate the sudden touch stimuli applied to *Drosophila* larvae during experiments [3]. Under 1 mN stimuli, both [3] and our system verified a 21% increment in the calcium fluorescence intensity of the Class III ddaA neurons. Furthermore, with the closed-loop force control capability and a control resolution better than 0.05 mN, we run the test under different force levels and decreased the applied force to as small as 0.25 mN. Quantitative relationship between the applied force level and the change in calcium fluorescence signal was acquired for the first time. The threshold force level at which the neuron started to get activated was determined to be 0.3 mN. The fluorescence camera we used took images at a higher frame rate than that of the previous work [3] without sacrificing the imaging quality, making calcium fluorescence measurement more accurate. The teleoperated experimental procedure reduced the training required for an operator and improved the overall operation efficiency.

Given that the calcium signal is a good indictor for the activities of the Class III ddaA neurons under mechanical stimulation [4], and our experimental results demonstrate strong positive correlation between the neuronal activities and the applied force level [3], the qualitative relationship between the fluorescence change and the force level suggests that the larva may display few danger-escaping behavior at a stimulus below 0.3 mN. This was not revealed in previous studies because of the lack of force control capability at the level below 1 mN [1]. Our work may contribute to new findings on sensory mechanotransduction in *Drosophila* larvae.

6.7 Conclusion

This paper reported a robotic approach for applying close-loop controlled mechanical stimuli to *Drosophila* larvae. Different force levels were accurately controlled in a closed-loop manner. The teleoperated touching and imaging procedure alleviated the workload for system operators. The

combination of switched fuzzy-PID controller and compensation-prediction scheme successfully addressed challenges such as measurement noise, modeling error, time delay and insufficient feedback modality altogether, providing fast convergence of force control both before and after reaching the switching threshold. Settling time and overshoot have been both reduced. The quantitative relationship between the calcium fluorescence change and the force level was experimental determined. The threshold above which the neuron started to respond to the stimulus was determined to be 0.3 mN. This system enabled accurate mechanical stimulation of *Drosophila* larvae, which may lead to novel biological discoveries in the mechanotrasduction mechanisms in *Drosophila* larvae.

References

[1] Y. Zhou, S. Cameron, W.-T. Chang, Y. Rao, et al., "Control of directional change after mechanical stimulation in drosophila," *Mol. Brain*, vol. 5, no. 1, pp. 39–51, 2012.

[2] R. Y. Hwang, L. Zhong, Y. Xu, T. Johnson, F. Zhang, K. Deisseroth, and W. D. Tracey, "Nociceptive neurons protect drosophila larvae from parasitoid wasps," *Curr. Biol.*, vol. 17, no. 24, pp. 2105–2116, 2007.

[3] A. Tsubouchi, J. C. Caldwell, and W. D. Tracey, "Dendritic filopodia, ripped pocket, nompc, and nmdars contribute to the sense of touch in drosophila larvae," *Curr. Biol.*, vol. 22, no. 22, pp. 2124–2134, 2012.

[4] C. Grienberger and A. Konnerth, "Imaging calcium in neurons," *Neuron*, vol. 73, no. 5, pp. 862–885, 2012.

[5] Y. Xiang, Q. Yuan, N. Vogt, L. L. Looger, L. Y. Jan, and Y. N. Jan, "Light-avoidance-mediating photoreceptors tile the drosophila larval body wall," *Nature*, vol. 468, no. 7326, pp. 921–926, 2010.

[6] Q. Yuan, Y. Xiang, Z. Yan, C. Han, L. Y. Jan, and Y. N. Jan, "Light-induced structural and functional plasticity in drosophila larval visual system," *Science*, vol. 333, no. 6048, pp. 1458–1462, 2011.

[7] W. Zhang, Z. Yan, L. Y. Jan, and Y. N. Jan, "Sound response mediated by the trp channels nompc, nanchung, and inactive in chordotonal organs of drosophila larvae," *Proc. Natl. Acad. Sci.*, vol. 110, no. 33, pp. 13 612–13 617, 2013.

[8] Z. Yan, W. Zhang, Y. He, D. Gorczyca, Y. Xiang, L. E. Cheng, S. Meltzer, L. Y. Jan, and Y. N. Jan, "Drosophila nompc is a mechanotransduction channel subunit for gentle-touch sensation," *Nature*, vol. 493, no. 7431, pp. 221–225, 2013.

[9] W. Zhang, A. Sobolevski, B. Li, Y. Rao, and X. Liu, "An automated force-controlled robotic micromanipulation system for mechanotransduction studies of drosophila larvae," *IEEE Trans. Autom. Sci. Eng.*, vol. PP, no. 99, pp. 1–9, 2015, ISSN: 1545-5955. DOI: 10.1109/TASE.2015.2403393.

[10] W. Zhang, X. Dong, and X. Liu, "Switched fuzzy-pd control of contact forces in robotic micro-biomanipulation," *IEEE Trans. Biomed. Eng.*, vol. PP, no. 99, pp. 1–1, 2016.

[11] W. Zhang, J. Qu, X. Zhang, and X. Liu, "A model compensation-prediction scheme for control of micromanipulation systems with a single feedback loop," *IEEE/ASME Trans. Mechatron.*, under review.

[12] W. Zhang, A. Sobolevski, B. Li, Y. Rao, and X. Liu, "An automated force-controlled robotic micromanipulation system for mechanotransduction studies of drosophila larvae," *IEEE Trans. Autom. Sci. Eng.*, vol. 13, no. 2, pp. 789–797, 2016.

[13] X. Wang, Z. Chen, and G. Yang, "Finite-time-convergent differentiator based on singular perturbation technique," *IEEE Trans. Automat. Contr.*, vol. 52, no. 9, pp. 1731–1737, 2007.

[14] S. Fye, K. Dolma, M. J. Kang, and S. Gunawardena, "Visualization of larval segmental nerves in 3rd instar drosophila larval preparations," *J. Vis. Exp.*, vol. 43, e2128–e2128, 2010.

[15] J. Betschinger, K. Mechtler, and J. A. Knoblich, "Asymmetric segregation of the tumor suppressor brat regulates self-renewal in drosophila neural stem cells," *Cell*, vol. 124, no. 6, pp. 1241–1253, 2006.

[16] B. Bello, H. Reichert, and F. Hirth, "The brain tumor gene negatively regulates neural progenitor cell proliferation in the larval central brain of drosophila," *Development*, vol. 133, no. 14, pp. 2639–2648, 2006.

[17] A. Pauli, F. Althoff, R. A. Oliveira, S. Heidmann, O. Schuldiner, C. F. Lehner, B. J. Dickson, and K. Nasmyth, "Cell-type-specific tev protease cleavage reveals cohesin functions in drosophila neurons," *Dev. Cell*, vol. 14, no. 2, pp. 239–251, 2008.

CHAPTER 7
Conclusion and Future Work

7.1 Summary of Accomplishments and Contributions

Robotic systems offer high efficiency and high precision in micromanipulation that could not be achieved manually. Contact force is involved in a wide range of micromanipulation tasks, which is why force control is of paramount importance in robotic micromanipulation. The increasing interests in the study of danger-escaping behavior of *Drosophila* larvae raise new questions for force-controlled micromanipulation systems. Many force control architectures have been proposed, but given the complexities and difficulties in micromanipulation, traditional force control architectures are unable to tackle measurement noise, time delay, modeling error and insufficient feedback modality all at the same time. This thesis contributes to the field by devoting efforts in four aspects. First of all, a robotic micromanipulation system for mechanical stimulation and calcium fluorescence imaging of *Drosophila* larvae is developed. Secondly, a switched fuzzy-PD controller to account for modeling error and measurement noise is designed and implemented. Thirdly, a compensation-prediction force control scheme to account for time delay and insufficient feedback modality is designed and implemented. Last but not least, the developed micromanipulation system together with the proposed force control architecture is developed to accurately apply mechanical stimuli to *Drosophila* larva samples, and the quantitative relationship between the applied force level and the change in calcium fluorescence response of the Class III ddaA neurons are acquired. Through the process, new techniques and insights are discovered, as organized below.

- Custom-made PDMS devices for effective immobilization of *Drosophila* larvae are designed and fabracated. It utilized a thin channel to press larval body for firm immobilization. The best height of the channel was determined to be 0.13 mm so that it could guarantee secured

immobilization and high survival of the larva samples. The flattened larval body also gained additional transparency for clearer observation under microscope.

- The first robotic micromanipulation system for mechanical stimulation and calcium fluorescence imaging of *Drosophila* larvae is developed. The system incorporated customized image processing and control software capable of real-time fluorescence imaging and teleoperated manipulation on *Drosophila* larvae. The software is written in C++ language and could be easily maintained.
- A novel switched fuzzy-PD controller for closed-loop force control in micromanipulation of *Drosophila* larvae is proposed and developed. The controller includes a noise-insensitive extended high gain observer (EHGO) to estimate the modelling errors of the robotic system based on the noisy force feedback. One key property of switched fuzzy-PD controller is that it combines the fast-convergence property of fuzzy controller and the small steady-state oscillation of PD controller.
- A new compensation-prediction scheme for force control in robotic micromanipulation to tackle challenges such as modeling errors, measurement noise, time delay and insufficient feedback modality is developed, which is applicable to a variety of micromanipulation systems. To simplify the implementation, I have proven that this method is equivalent to implementing a Smith predictor as if there is no modeling error and adding an additional correction term to the tracking error (which is calculated from a noise-insensitive extended high gain observer (EHGO) estimation). This scheme effectively deals with the compensation and prediction of the system model and can be used with any type of model dependent controllers. The scheme has been demonstrated to significantly improve the system's overall control performance.
- The first quantitative study of the relationship between the force stimulus level and the change in calcium transmission fluorescence signal in Class III ddaA neurons of *Drosophila* larvae is investigated. The developed micromanipulation system was used to apply force-controlled mechanical stimuli to individual larvae at different force levels and simultaneously

quantify the corresponding time history of the calcium fluorescence intensity of the target Class III ddaA neuron. Based on the experimental result, the minimum force level at which the neuron starts to respond was determined to be 0.3 mN.

7.2 Future Work

During the course of the presented research, new ideas of developing the micromanipulation systems were realized, new approaches of contact force control were conceived and carried out in biological experiments. These efforts contribute to improving micromanipulation system performance and quantifying biological results. Along the pathway, some aspects have been found that they could be pursued to further boost these accomplishments.

- The current control software utilizes the standard communication protocol of the micromanipulator which lacks certain functions, such as updating the coordinates of the micromanipulator in real time. The software can be further developed to add another low-level layer of the micromanipulator protocol for real-time coordinate communication.
- The mechanical setup of the micromanipulation system still has room to improve. The current connection mechanism for holding the piezoresistive force sensor and glass pipette was custom-made, and including an iron rod and a pipette holder. This can be improved by implementing a single-piece metallic extension without screw connections.
- The noise-insensitive EHGO works well for our current system. However, due to its nonlinearity, it requires manual tuning of the parameters via trial-and-error experiments. The nonlinearity comes from the function $h(x)$ of the system. If this function is replaced with a linear function, the EHGO will be linear and its parameters could be tuned with mature methods automatically.
- This thesis has demonstrated the use of the compensation-prediction scheme for our current system which is a two-dimensional state-space system. However, the variable-changing technique is universal and could be applied to systems with higher dimensions as well. Additional mathematical analysis is needed to extend this approach to systems with higher dimensions.